DISS. ETH No. 14055

Single molecules as sensitive probes in high-resolution optical microscopy

A dissertation submitted to the

SWISS FEDERAL INSTITUTE OF TECHNOLOGY ZÜRICH

For the degree of
Doctor of Natural Sciences

presented by
BEATE SICK
Diplom-Physikerin, Ruprecht-Karls-Universität Heidelberg

born August 25, 1967 in Stuttgart
Germany

Accepted on the recommendation of:
Prof. Dr. Urs P. Wild, Examiner
Prof. Dr. Frédéric Merkt, Co-Examiner
Dr. Bert Hecht, Co-Examiner

Zürich 2001

Contents

Abstract

Widely used models in physics, chemistry and biology are often based on a single-molecule description. In the last decade it became possible to detect single molecules, and to measure some of their physical and chemical properties. Single-molecule experiments can directly provide the distribution and time trajectory of an observable. This is an essential advantages over ensemble measurements, which yield only mean values averaged over a whole population of molecules.

This thesis is concerned with the optical investigation of single molecules at room temperature. A high-resolution fluorescence microscope has been developed, which combines a scanning confocal optical microscope (SCOM) and a scanning optical near-field microscope (SNOM). A new method for the fabrication of optical near-field probes is presented, which yields high-quality probes. Single-molecule sensitivity and an optical resolution down to 50 nm is demonstrated for the SNOM part of the instrument. The single-molecule sensitivity of the confocal microscope is shown in various experiments. The theoretically predicted resolution is achieved which is proven by the comparison of simulated and measured single-molecule images.

The main limitation in optical single-molecule studies at room temperature results from the limited number of photons emitted by a fluorescent molecule. The investigation of single terrylene molecules embedded in a p-terphenyl crystal reveals an extraordinarily high photostability of the fluorophores. More than 10^8 fluorescence photons are on average emitted from individual molecules before photo-bleaching takes place. This number of photons exceeds all previously reported values by more than one order of magnitude. However, fluorescent molecules which are frequently

used as labels in biological experiments requiring physiological conditions only emit in the order of 10^5 photons before photo-bleaching. For this reason efficient methods are required which allow to gain as much information as possible from the limited amount of photons. A new method for rapid identification of single molecules is presented which relies on simultaneous spectral and time-resolved photon counting. It is shown that a few hundred detected photons are sufficient to assign an observed molecule to one out of four species with a confidence level higher than 99.9%.

An important parameter in various single-molecule experiments is the orientation of the molecular absorption dipole moment, because the orientation has an influence on other parameters, e.g. the lifetime of a fluorophore in the neighborhood of a dielectric or metallic interface does depend on the orientation of the molecule. It is shown for the first time how a confocal microscope can be utilized for reliably determining the three-dimensional orientation of single molecules. The method relies on engineering the field-distribution in the focus of a high numerical aperture lens such that all electric field components acquire comparable magnitudes. Single molecules are utilized to map the field distribution in the excitation focus, which verify the performed simulations.

Zusammenfassung

Weitverbreitete Modelle in der Physik, Chemie und Biologie beruhen auf einer Einzelmolekülbeschreibung. Im letzten Jahrzehnt wurde es möglich einzelne Moleüle zu detektieren und manche ihrer physikalischen und chemischen Eigenschaften zu messen. Experimente an einzelnen Molekülen machen sowohl die Verteilung einer physikalischen Meßgroße als auch deren zeitliche Entwicklung direkt zugänglich. Dies ist ein wesentlicher Vorteil gegenüber Ensemble-Experimenten, bei denen immer ein Mittelwert über eine ganze Population von Molekülen gemessen wird.

Die vorliegende Arbeit beschäftigt sich mit der optischen Untersuchung von einzelnen Molekülen bei Zimmertemperatur. Ein hochauflösendes Fluoreszenzmikroskop wurde entwickelte, welches ein konfokales optisches Rastermikroskop (SCOM) und ein nahfeldoptisches Rastermikroskop (SNOM) kombiniert. Ein neues Herstellungsverfahren für qualitativ hochwertige optische Nahfeldspitzen wird vorgestellt. Die Einzelmolekülsensitivität und eine optische Auflösung von bis zu 50 nm wird für den SNOM-Teil des Instruments nachgewiesen. Die Einzelmolekülsensitivität des konfokalen Mikroskops wird in verschiedenen Experimenten demonstriert. Durch den Vergleich von simulierten und gemessenen Rasterbildern von einzelnen Molekülen wird nachgewiesen, daß die theoretische Auflösungsgrenze erreicht wird.

Die größte Beschränkung bei optischen Messungen an einzelnen Molekülen bei Zimmertemperatur ist die begrenzte Zahl von emittierten Photonen. Die Untersuchung von einzelnen Terrylenmolekülen, die in einen p-terphenyl Kristall eingelagert sind, weist eine extrem hohe Photostabilität der Fluorophore nach. Mehr als 10^8 Fluoreszenzphotonen werden im Mittel von einem einzelnen Molekül emittiert bevor es photobleicht. Diese Zahl übersteigt alle zuvor bekannten Werte um mehr als eine

Größenordnung. Allerdings emittieren Fluoreszenzmoleküle, die in der Biologie als Marker eingesetzt werden, unter physiologischen Bedingungen im Mittel nur etwa 10^5 Photonen bevor sie bleichen. Aus diesem Grund bedarf es effizienter Methoden, die es erlauben möglichst viel Information aus der begrenzen Zahl von Photonen zu gewinnen. Eine neue Methode für effiziente und schnelle Identifikation von einzelnen Molekülen wird vorgestellt, die auf gleichzeitigem spektral und zeitaufgelöstem Photonenzählen beruht. Es wird nachgewiesen, daß wenige hundert detektierte Photonen ausreichen, um ein beobachtetes Molekül mit einer Sicherheit von 99,9% einer von vier verschiedenen Spezies zuzuordnen.

Ein wichtiger Parameter in verschiedenen Experimenten mit einzelnen Molekülen ist die Orientierung des molekularen Absoptionsdipolmoments. So wird etwa die Lebensdauer von Fluorophoren in der Nähe von dielektrischen oder metallischen Grenzflächen durch die Orientierung des Moleküls beeinflußt. In der vorliegenden Arbeit wird zum ersten mal gezeigt, wie ein konfokales Mikroskop eingesetzt werden kann, um die dreidimensionale Orientierung eines Moleküls zuverlässig zu bestimmen. Die Methode beruht darauf, eine elektrische Feldverteilung im Fokus eines Objektivs mit hoher numerischer Apertur so zu konstruieren, daß alle Feldkomponenten vergleichbare Größe haben. Einzelne Moleküle werden eingesetzt, um die Feldverteilung im Anregungsfokus abzubilden, wodurch die durchgeführten Simulationen zur Berechnung der Feldverteilung verifiziert werden.

1. General introduction

The topic of this thesis is the optical investigation of single-molecules at room temperature. As an introduction into the field a brief review about the advent of single-molecules studies is given. The potentials, limits, achievements, and challenges of single-molecule measurements at room temperature are discussed. The chapter closes with a preview of the contribution of this work to the field.

Seite Leer /
Blank leaf

1.1   Principle of the performed studies

This thesis is concerned with optical single-molecule studies at room temperature using a home-built, high-resolution fluorescence microscope. For this kind of study fluorophores are spatially separated by embedding them at low concentration in a transparent matrix. They are excited by illumination with laser light, and the resulting fluorescence light is detected by a sensitive microscope.

1.2   Brief history

The evolution of nano-science started with the invention of the scanning probe techniques like STM (Scanning Tunneling Microscopy), AFM (Atomic Force Microscopy) and SNOM (Scanning Near-Field Optical Microscopy) in the 1980s. These instruments, capable of for controlling and imaging matter on the level of single molecules, have provided unique information about conformational and mechanical properties of molecular systems [38]. In contrast to scanning probe techniques, which are restricted to the investigation of surfaces, optical far-field techniques make it possible to address molecules deep inside a transparent bulk sample. Because optical far-field techniques require no mechanical contact, they allow for a non-invasive investigation of the sample. Optical detection of single molecules has been achieved for the first time in 1989 in a low-temperature absorption experiment [75]. A drastical improvement of the signal-to-noise-ratio was obtained one year later by applying fluorescence techniques to low-temperature single-molecule experiments [85]. In 1990 the detection of single fluorophores at room temperature was achieved in solution [21]. Optical imaging of immobilized single fluorophores at room temperature was demonstrated for the first time in 1993 by near-field microscopy [16], followed by optical far-field experiments [34,54,71], which in particular opened the way for non-invasively studying biological processes under physiological conditions.

Since that time the field of optical single-molecule studies concerning experiments at room temperature as well as at low temperatures has been developing rapidly. There are several excellent reviews [29,80,90,126,129] of these developments.

1.3 Potentials and achievements of single-molecule studies

Single-molecule experiments have essential advantages over ensemble measurements, because they yield distributions and time trajectories of observables in addition to averaged values.

For example a single-molecule study could prove that the origin of the multi-exponential electron-transfer kinetics, which were observed in ensemble measurements of photo-induced electron transfer from fluorophores to a semiconductor surface, is the static inhomogeneity of site dependent single-exponential transfer kinetics for each single fluorophore [67].

If the molecules of interest are not fluorescent themselves, they can be tagged with fluorophores. This allows their identification, the determination of their position, as well as the tracking of their motion.

Great benefits were gained in the investigation of molecular motor activities by following the motions of labeled subunits. These measurements revealed that a kinesin molecule slides along microtubules in steps of 8 nm [104], the rotation of F_1-ATPase was observed which rotates with discrete 120° steps [131], and the movement of a single myosin head along an actin filament in regular steps of 5.3 nm was observed [57].

Distances on a nanometer scale can be determined between acceptor and donor fluorophores using single-molecule fluorescence resonant energy transfer (FRET). Labeling one macromolecule at specific positions with donor and acceptor fluorophores allows following intra molecular motions.

The assembly-disassembly of individual proteins as well as conformational changes occurring within a single protein molecule were observed by labeling different protein subunits with donor and acceptor fluorophores and performing FRET measurements [53].

Time-dependent processes and reaction pathways can be followed without the need for synchronizing an ensemble of molecules, if at all possible. Subpopulations with different behavior can be revealed in inhomogeneous ensembles. Rare or short transient intermediates can be observed, that are difficult to capture in ensemble

measurements because of their low steady-state concentrations.

A single-molecule study of RNA catalysis and folding was performed by attaching a donor and acceptor fluorophore to specific sites on the ribozyme molecule [136]. Three different folding pathways were observed, each with at least one intermediate state. A fast-folding pathway was recorded, which had remained unobserved in ensemble measurements.

The small size of a single molecule and the sensitivity of its fluorescence properties to external perturbations makes it an ideal local sensor. Thus, static and dynamic heterogeneities in populations of molecules in a complex condensed system can be identified and related to the molecular environment. A single molecule can be utilized to test microscopic theories. Even controlling the properties of a single fluorophore by selective external perturbations is possible.

Fluctuations in time-resolved fluorescence spectra of single-fluorophores attached to a protein were observed and attributed to slow spontaneous conformational changes of the protein [127]. Following a labeled lipid molecule in the membrane of a living cell revealed spatial heterogeneities in the shape of lipid-specific membrane domains whose existence, locations, shapes and motions could be observed [106]. Controlled life-time changes of a fluorophore were demonstrated by scanning a near-field tip above the fluorophore [2,116].

1.4 Limitations and challenges of single molecule studies

Major limitation in optical single-molecule studies at room temperature result from the limited number of photons emitted by a fluorophore (see chapter 2). After the fluorophore is photo-bleached it can not be used for further investigations. This implies the need for sensitive microscopes with high detection efficiency, to collect as much as possible of the limited amount of photons. Moreover, any development which provides more photostable fluorophores is of utmost importance. A higher photostability can either be achieved by appropriate environments (see chapter 4) which protect the fluorophores, or by developing more photostable dyes or other

fluorescing nano-particles. As long as no better dyes are available and the experiment demands a certain environment like physiological conditions for investigating biological processes, methods are required which gain as much information as possible from each emitted photons (see chapter 5). In general the more characteristic parameters are extracted the fewer photons are required for non-ambiguous conclusions. As an example one can think of identification, where every determined observable, in which the species differ, helps to distinguish between them. Simultaneous determination of various parameters is also needed for other applications because the change of one observable can influence another observable, which can lead to ambiguous measurements if not all observables are observed simultaneously. This implies also the need for doing appropriate statistical analyses and developing a statistical theory of molecular interactions. For example, the lifetime of a fluorophore in the neighborhood of a metallic surface or a dielectric interface does not only depend on the distance to the surface but also on the orientation of the molecule [23, 69, 70, 86]. The transfer efficiency in FRET measurements does not only depend on the distance, but simultaneously on the mutual orientation of donor and acceptor [41]. In applications like these, determination of the orientation of the molecular transition dipoles is an important task. As a matter of fact, standard polarization microscopy yields only information about the in-plane component of the emission dipole moment. Recently developed wide-field microscopy techniques for determining the full three-dimensional information of the dipole orientation rely on defocusing or aberrated imaging with the drawback of diminished resolution [27,102]. Scanning near-field microscopy, too, can be utilized for three-dimensional orientational imaging of molecules at the surface, based on analyzing two images of the same sample area recorded with different polarizations of the excitation light. The analysis requires detailed knowledge about the optical probe [124]. In conclusion there is a need for a reliable, high-resolution far-field technique for orientational imaging (see chapter 6).

Single-molecule studies, combining sensitive optical measurements with single-molecule manipulation techniques like patch-clamb, atomic force microscopy, and optical or magnetic tweezer, could provide even more information about molecular

processes. A discussion of this issue would be challenging but is beyond the scope of this introduction.

1.5   Preview of this work

The main focus of this thesis is on the development of methods and instrumentation aiming at optical single-molecule studies at room temperature. According to the foregoing section today's technical challenge is the simultaneous determination of all possible observables with as possible high resolution and few required photons. The objects under investigation in this work are the single molecules as well as the instruments. Both topics are complementarily interconnected because the instruments are utilized for investigation of single molecules and *vice versa*.

Chapter 2 provides the fundamentals which are required to understand the concepts underlying the following chapters. The chapter is divided into two parts. The first part is concerned with basic photo-physical properties of fluorescent molecules. The necessary requirements for single-molecule studies are discussed. The second part provides the basics of optical imaging. A brief introduction to the angular spectrum representation of optical fields is given, a mathematical technique used to describe propagation of light e.g. in optical microscopes. Using this terminology the fundamental difference between near-field and far-field microscopy is discussed. Moreover, the prerequisites for the calculation of the focal field-distribution in a scanning confocal microscope are provided, which will be needed in chapter 6.

Chapter 3 deals with the instrument designed within this work. The guideline was to strive for the requirements of single-molecule studies (see section 2.1.2) and to determine all parameters describing a fluorophore with a most possible high resolution. A combination of a scanning confocal optical microscope (SCOM) and a scanning near-field optical microscope (SNOM) was realized. Additionally, a fabrication method for optical near-field probes is presented, well suited for every-day use because it is reliable, easy to handle, inexpensive and permits batch production. The capabilities of SCOM as well as SNOM are demonstrated. It turned out that SCOM is much better suited for routine single-molecule studies. Therefore, all

studies presented in the forthcoming chapters are performed by utilizing the SCOM part of the instrument.

In chapter 4 single terrylene molecules embedded in a p-terphenyl crystal are investigated. The most prominent result presented in this chapter is the fact that this system provides an extraordinarily high photostability of the fluorophores. This was exploited for measurements which demonstrated for the first time non-classical photon statistics at room temperature [32].

Chapter 5 presents a new method for rapid and reliable identification of single molecules by spectral and simultaneously time-resolved photon counting. This method relies on analyzing each successively detected photon by comparing the determined observables with experimentally obtained fingerprints of different species which describe the distributions of these observables.

In chapter 6 the main result of this thesis is shown. Simulations and measurements are presented which show that the focal field distribution of a high numerical aperture lens can be engineered such, that all electric field components acquire comparable magnitudes. Single molecules were utilized to map the field distribution. Relying on characteristic image patterns, a method is presented which allows for a reliable and easy determination of the three-dimensional orientation of arbitrarily oriented single molecules on the basis of a single SCOM image while simultaneously benefiting from the SCOM immanent advantages of high spatial and temporal resolution.

Seite Leer /
Blank leaf

2. Fundamentals

This chapter describes the basic concepts that are required to understand the single-molecule experiments which are presented in the following chapters. The first part of this chapter is concerned with the basics of fluorescence. In summary, a fluorophore is described by its spatial parameters (position, orientation of absorption and emission dipole), its spectral parameters (absorption and emission spectrum), its dynamics (singlet lifetime, triplet lifetime, intersystem crossing rate) as well as its absorption cross section, fluorescence quantum yield, and photo-bleaching quantum yield. The requirements for single-molecule studies are discussed. The second part of this chapter provides the basics of optical imaging. A brief introduction into the angular spectrum description of optical fields is given, a mathematical technique used to describe the propagation of light e.g. in optical microscopes. It is applied to the discussion of basic properties of near-field and far-field optical imaging.

2.1 Basics of optical single-molecule studies

2.1.1 Fluorescence

All experiments within this work are performed with fluorescent molecules at room-temperature. In such experiments the characteristic fluorescence properties of the fluorophores are the possible observables. The different observables and their dependence on environmental parameters are discussed in the following.

Simple three level system

The characteristic fluorescence properties of fluorophores are determined by the photo-physical processes which occur between the absorption and the emission of light. Different species of fluorophores can be distinguished on the basis of their specific fluorescence properties.

A Jablonski-diagram (see figure 2.1) can be used to describe the underlying photo-physical processes. The three lowest electronic states are depicted as thick
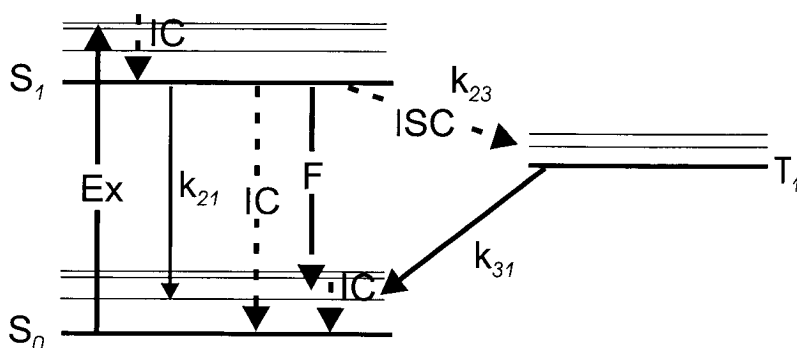
Figure 2.1: Jablonski diagram. The thick horizontal lines marked with S_0, S_1, and T_1 are the three lowest electronic states. The thin lines depict the corresponding vibrational states. Transitions between the states are illustrated as arrows: excitation (Ex), fluorescence (F), non-radiative relaxation by internal conversion (IC), inter-system crossing (ISC). The relevant decay rates k_{21}, k_{23}, and k_{31} are depicted.

horizontal lines. At each of these electronic energy levels the fluorophore can exist in

a number of vibrational energy levels (thin horizontal lines). The arrows illustrate transitions between the states which occur in about 10^{-15} s.

At room temperature, thermal energy ($kT \approx 200\,\mathrm{cm}^{-1}$) is not sufficient to significantly populate the excited vibrational states (energy spacing between vibrational states $\approx 10^2 - 10^3\,\mathrm{cm}^{-1}$). For this reason absorption typically takes place from the lowest energy level. The ground state of a typical fluorescent molecule is a singlet S_0 because usually its electrons are all paired. The probability for absorption a photon is determined by the absorption dipole moment of the molecule and the energy density of the excitation light.

By absorbing a photon the fluorophore is excited (Ex) to one of the vibrational levels of the first excited state, which is again a singlet. In condensed matter the molecule relaxes rapidly (10^{-12} s or less) to the lowest vibrational level of S_1; this process is called internal conversion (IC). Because the singlet lifetime is about three orders of magnitude longer, internal conversion is usually completed before further processes take place, which are therefore independent of the excitation.

From S_1 there are several relaxation paths:
(1) a fluorescence photon (F) is emitted, taking the molecule back to one of the vibrational levels of the ground state. Again internal conversion causes a rapid relaxation to the lowest vibrational level S_0. According to the Franck-Condon principle the emission spectrum has usually the shape of the mirrored absorption spectrum. Moreover the emission spectrum is red-shifted, because the energy of the emission is usually less than that of the absorption as can be seen in the Jablonski-diagram. This leads to the so called Stokes-shift.
(2) the excitation energy can dissipate non-radiatively by internal conversion. The total $S_1 \rightarrow S_0$ relaxation rate including all processes is k_{21}.

(3) A molecule in the S_1 state can also undergo a spin conversion, called intersystem crossing (ISC), to the first triplet state T_1. The rate of this ISC is k_{23} The triplet lifetime is usually several orders of magnitude longer than the singlet lifetime, because the radiative transition, called phosphorescence, from T_1 to S_1 is forbidden. The $T_1 \rightarrow S_0$ rate is k_{31}.

Back in the ground state S_0 the described cycles start again until the molecule photo-bleaches. About $10^5 - 10^6$ cycles before photo-bleaching is a typical number for widely used fluorophores at ambient conditions. The inter-system crossing yield is often in the range of 10^{-2} which implies that the molecule will pass through the triplet state many times during its life. Excursions to the triplet state are visible as off-times in the fluorescence of the molecule, provided that the triplet lifetime is longer than the average excitation-emission cycle time.

Transition dipole moment

Fluorescence result from the interaction of light with a fluorophore. Knowledge about this interaction and the fluorophore allows for investigation of optical fields. In chapter 6.4.1 it is demonstrated that single molecules can be utilized to map electric field components in confined optical fields.

A common procedure for describing the light-molecule interaction is to use the electric-dipole-approximation [55]. In the simplest case the absorption dipole and the emission dipole of a fluorophore have the same transition dipole moment $\vec{d}$. The interaction of an electric dipole with an oscillating electric field $\vec{E} = \vec{E_0} \cos \omega t$, like contained in a optical field, is restricted to the component, which is parallel to the dipole [55]. In view of fluorophore-light interaction this results in a fluorescence rate R which is directly proportional to the squared electric field component parallel to the molecular absorption dipole [90]:

$$R(\vec{r}) = c \left| \hat{d} \cdot \vec{E}(\vec{r}) \right|^2 = c \cdot \vec{E}_\parallel^2(\vec{r}) , \tag{2.1}$$

which is valid well below saturation. Here, $\hat{d}$ is the unit vector along the absorption dipole moment of the molecule, $\vec{E}(\vec{r})$ is the electric field vector at the position $\vec{r}$ of the molecule, $\vec{E}_\parallel^2(\vec{r})$ is the squared component of the electric field parallel to $\hat{d}$, and c is a constant, which is defined at the end of this section.

According to relation 2.1, a fluorophore with a fixed absorption dipole maps the distribution of the parallel squared electric field component $\vec{E}_\parallel^2$ of an optical field if the molecule is moved with high spatial accuracy through the field and the

fluorescence rate is recorded at each point. *Vice versa* the resulting fluorescence intensity map $R(\vec{r})$ allows for concluding about the orientation of the imaged molecule provided the field-distribution $\vec{E}(\vec{r})$ is known (see chapter 6.4.1). The emitted fluorescence light is polarized along the emission dipole orientation, which allows for determining the orientation of emission dipole by analyzing the polarization of the emitted light [45].

A rigorous derivation of equation 2.1 is beyond the scope of this thesis, but the underlying theory shall be briefly mentioned. One usually starts with the optical Bloch equations in rotating wave approximation [90], which describe the time-evolution of the populations in a three level system driven by excitation light like depicted in figure 2.1. The steady-state solution contains among others the mean population ρ_{22} of the S_1-state and its radiation lifetime T_{rad} in dependency on the rates k_{21}, k_{23}, and k_{31}. With this information the spontaneous emission rate $R = \frac{\rho_{22}}{T_{rad}}$ can be calculated [90]:

$$R = \frac{2\,(\vec{d}_{vac}\cdot\vec{E})^2\,T_1\,T_2\,/\hbar T_{rad}}{1 + [(\omega - \omega_0)\,T_2]^2 + 4\,(\vec{d}_{vac}\cdot\vec{E})^2\,T_1\,T_2\,K\,/\hbar}\;, \tag{2.2}$$

where $T_1 = (k_{21} + k_{23})^{-1}$ is the lifetime of S_1, T_2 is the dephasing time, $T_{rad} = T_1/\phi_f$ is the radiative lifetime where ϕ_f is the fluorescent quantum yield, $K = 1 + 0.5\frac{k_{23}}{k_{31}}$, ω is the frequency of the excitation light, and ω_0 is the resonance frequency of the molecule.

Recalling that the dephasing time T_2 at room temperature is in the range of 10^{-12} seconds and provided that the excitation frequency does not differ by orders of magnitude from the resonance frequency of the molecule, the emission rate at room temperature is given by:

$$R = \frac{2\,(\vec{d}_{vac}\cdot\vec{E})^2\,T_1\,T_2\,/\hbar T_{rad}}{1 + 4\,(\vec{d}_{vac}\cdot\vec{E})^2\,T_1\,T_2\,K\,/\hbar}\;. \tag{2.3}$$

The fully saturated emission rate R_∞ is achieved for high excitation intensities when the first term in the denominator in equation 2.3 can be neglected compared

to the second which reduces equation 2.3 to:

$$R_\infty = \frac{1}{2\,T_{rad}\,K} \ , \tag{2.4}$$

where $K = 1 + 0.5\frac{k_{23}}{k_{31}}$ describes the effect of the triplet bottleneck in the three level system. The effect of the triplet bottleneck on R_∞ is the larger the larger k_{23} and the smaller k_{31} is. Another limitation for the emission rate is the finite radiative lifetime T_{rad} which causes anti-bunching in the emission of two successively emitted photons.

Well bellow saturation the second term in the denominator in equation 2.3 is much smaller than the first term, which leads to

$$R = c \cdot (\vec{d}_{vac} \cdot \vec{E})^2 \ , \tag{2.5}$$

with

$$c = \frac{2\,T_1\,T_2}{\hbar\,T_{rad}} \ . \tag{2.6}$$

External influence on fluorescence

The fluorescence behavior of a fluorophore is influenced by its environment. For this reason a fluorophore can be utilized as local probe. Following the fluorescence behavior of a fluorophore it is possible to observe the interaction between the fluorophore and a second molecule. On the other hand it is also possible to design the environment in view of desired properties, for example working at low temperature allows for achieving narrow spectral linewidths. In chapter 4 it is demonstrated that an extraordinary high photo-stability of terrylene molecules at room temperature can be achieved by embedding them in a crystal. But even under the protected

conditions within a crystal the fluorescence shows on-off behavior, which can be explained by diffusing oxygen molecules occasionally coming close to the fluorophore.

One effect of the environment on the fluorophore is the decrease of the fluorescence rate, which is called quenching. Quenching can occur by different mechanisms depending on the fluorophore and environmental parameters.

In the case of collisional quenching the fluorophore during the encounter with the quencher goes to the triplet state or back to the ground state without emitting light. Quenching by heavy atoms is explained by enhanced spin-orbit coupling and a consequently increased rate of inter-system crossing to the triplet monitored. Another model is used in the case of oxygen, which is the most prominent quencher. If an oxygen molecule in its ground state $^3O_2$ encounters the fluorophore in its excited singlet or triplet state, the excitation energy is transferred to the oxygen molecule, generating the $^1S_0$ state of the fluorophore and $^1O_2^*$, the first excited state for the oxygen known [37]. This can subsequently result in photo-destruction of the fluorophore due to reaction with the highly reactive singlet oxygen.

Fluorescence quenching of a fluorophore can also occur due to energy transfer to a metallic structure in close proximity to the molecule [59, 86]. Quenching processes relying on energy transfer to other channels then relaxation by emission of a photon are always connected with a decreasing lifetime of the excited state [23, 87], because the lifetime is inversely proportional to the sum of all rates leading away from the excited state. For this reason changes in the fluorescence dynamics reflect changes in the environment.

Another prominent effect is the fluorescence resonance energy transfer (FRET) [41, 59]. FRET relies on energy transfer from a donor fluorophore to an acceptor fluorophore, which becomes observable as acceptor fluorescence. Energy is transfered by dipole-dipole coupling if the distance between acceptor and donor is in the order of a few namometers, whereby the amount of energy transfer depends strongly on the distance and the mutual orientation of the two fluorophores. For this reason single-pair FRET allows for precise distance measurements on a nanometer scale, provided that information about the mutual orientation of both fluorophores is available.

Observables in optical single-molecule studies

In conclusion, the possible observables in optical measurements on single-molecules are the spectral properties of the fluorophore (absorption and emission spectrum), its dynamic (singlet lifetime, triplet lifetime, intersystem crossing rate), spatial parameters (position, orientation of absorption and emission dipole) as well as absorption cross section, fluorescence quantum yield (the probability for the emission of a fluorescence photon per excitation circle), and photo bleaching quantum yield (the probability for photo-bleaching per excitation circle). Interaction between two molecules or one molecule with its environment can be studied by observing and interpreting changes in these observables.

2.1.2   Requirements for single-molecule studies

Choose appropriate fluorophores and environmental conditions

For performing optical measurements on a single molecule, it should be bright and stable. This requirements can be expressed in terms of photo-physics and photo-chemistry, respectively.
For achieving the highest fluorescence rate at a given excitation intensity

- the absorption dipole moment of the fluorophore should be as large as possible,

- the fluorescence quantum yield should be almost one: $\Phi_f \sim 1$,

- the radiation lifetime T_{rad} of the S_1 state should be as short as possible,

- the inter-system crossing rate should be small: $k_{23} \sim 0$,

- the triplet lifetime should be as short as possible,

- and non-radiative energy transfer should be avoided.

The photo-stability of a fluorophore is mainly determined by environmental parameters. A crystalline host can provide protecting conditions (see chapter 4). For many

single-molecule application in biology or chemistry ambient conditions are required. In these cases dispositions for oxygen protection should be made.

Experimental requirements

The only fundamental requirement for a single-molecule experiment is a sufficient signal-to-noise ratio (SNR). To distinguish between signal and background, mainly the above discussed Stoke shift in the wavelength of the fluorescence against excitation is exploited. Also time-gated detection can be utilized for this purpose e.g. if pulsed excitation is used.

A high signal can be achieved by meeting the above mentioned criteria for a high fluorescence rate of the single fluorophore, providing a high collection and detection efficiency, and working with an appropriate integration time.

The noise should be as small as possible by a given single-molecule signal. Three sources of noise can be distinguished: shot noise form the background luminescence, shot noise from the single molecule fluorescence itself, and dark counts. All three sources of noise are discussed in the following with respect to possibilities to improve the SNR.

Shot noise form the background luminescent can arise from other luminescing molecules in the excitation volume, luminescing optical components, and stray light from the laser. These background contributions increase proportionally with the laser power. In contrast to that, the single-molecule signal saturates at a certain excitation power, because of excursions to the dark triplet state, which become dominating at high excitation power, and due to the anti-bunching property (it is very unlikely, that a single molecule emits two photons simultaneously or with time lags orders of magnitude smaller then its singlet lifetime). For this reason single-molecule experiments are performed well below saturation. To strive for a low background, notch and bandpass filters should be used for efficiently blocking of the excitation laser light. High quality optical components with small auto-luminescence are required. Because auto-luminescence increases strongly when the excitation wavelength is lowered, fluorophores should be chosen which can be excited

in the green or red. The background contribution from other luminescing molecules can be decreased by working with small illumination volumes, thin samples, and again long wavelength excitation.

The shot noise of the single molecule is given by the square root of the single-molecule signal and consequently it can not be decreased by a fixed signal. However, well below saturation the signal of the single-molecule increases proportional with the laser power and with that faster then its shot noise, which results in a improved SNR with increased laser power.

For achieving a low dark count contribution a detector with small dark count rate should be chosen, whereby a high SNR simultaneously requires a high quantum efficiency. Beside electronic noise, dark counts caused by residual room and stray light should be avoided.

2.2 Basics of optics

2.2.1 Goal of optical microscopy

In order to optically image an object it is illuminated by light. This causes different interactions between light and matter like absorbance, diffraction, scattering, refraction, fluorescence etc. to take place. The result of these interactions is a complex optical field distribution emerging from the object. Let $z = 0$ be the plane of the object, where z is the optical axis of an imaging system. In the following sections it will be discussed how an optical field distribution $\vec{E}$ in the object plane evolves along the optical axis. This optical field is denoted as $\vec{E}$, because in most optical experiments only the electrical part of an electro-magnetic field can be measured.

The ultimate goal of optical imaging is to get a field distribution $\vec{E}_i$ in the image plane which is a perfect, magnified and eventually amplified replica of the field distribution $\vec{E}$ in the object plane:

$$\vec{E}_i(x_i, y_i) = a \cdot \vec{E}\left(\frac{x_i}{M}, \frac{y_i}{M}, 0\right) , \tag{2.7}$$

where M is the magnification of the imaging system, x_i, y_i are Cartesian transverse coordinates to describe the spatial positions in the image plane, and a is the amplification factor.

2.2.2 Angular spectrum representation of optical fields

The angular spectrum representation is a very powerful mathematical technique to describe propagation of light in optical microscopes [39]. The following brief introduction to the angular spectrum serves as basis for a discussion about potentials and limits of optical far- and near-field microscopy (see the following sections) as well as for the description of characteristic parameters of the implemented microscope (see chapter 3). Moreover, the angular spectrum representation is the mathematical instrument for the calculation of field-distributions in the focal region of a high numerical aperture objective (see chapter 6).

The angular spectrum representation of an optical field $\vec{E}$ across a plane, here $z = 0$, comprises its decomposition into an infinite series expansion in terms of Fourier components. The amplitude-distribution of the Fourier components is called angular spectrum $\vec{A}$ and forms a Fourier transform pair with the field-distribution $\vec{E}$.

$$\vec{E}(x, y; 0) = \mathcal{F}^{-1}\left\{\vec{A}_0(k_x, k_y)\right\} = \frac{1}{2\pi} \int\int \vec{A}_0(k_x, k_y)e^{i(k_x x + k_y y)} \, dk_x dk_y \quad , \quad (2.8)$$

$$\vec{A}_0(k_x, k_y) = \mathcal{F}\left\{\vec{E}(x, y; 0)\right\} = \frac{1}{2\pi} \int\int \vec{E}(x, y; 0)e^{-i(k_x x + k_y y)} \, dx dy \quad , \quad (2.9)$$

where k_x, k_y are reciprocal coordinates also called spatial frequencies.

Recalling the equation for a unit-amplitude plane wave in the three-dimensional space

$$W(x, y, z) = e^{i(k_x x + k_y y + k_z z)} \tag{2.10}$$

propagating in direction $\vec{k} = (k_x, k_y, k_z)$ with

$$k_z := \sqrt{k^2 - k_x^2 - k_y^2} \, , \tag{2.11}$$

where $k^2 = \left(\frac{2\pi n}{\lambda}\right)^2$ with the refraction index n of the medium and the wavelength λ in vacuum, the field $\vec{E}$ can be considered as a superposition of an infinite set of plane waves observed in the plane $z = 0$. The plane wave with direction determined by $\vec{k} = (k_x, k_y, \sqrt{(2\pi n/\lambda)^2 - k_x^2 - k_y^2})$ contributes according to the complex amplitude $\vec{A}_0(k_x, k_y)$. This is the reason why $\vec{A}_0(k_x, k_y)$ is also called angular spectrum of plane waves. Figure 2.2 illustrates a plane wave in the object-plane by depicting its wave-fronts as phase-zero lines. The figure visualizes the spatial frequencies k_x, k_y, and shows $\vec{k}_\parallel$, which is the in-plane projection of the wave vector $\vec{k}$.

The field in the plane $z = 0$ gives rise to a field distribution across a parallel plane at a distance z which is, in analogy to equation 2.8, represented by

$$\vec{E}(x, y; z) = \mathcal{F}^{-1}\left\{\vec{A}_z(k_x, k_y)\right\} = \frac{1}{2\pi} \int\int \vec{A}_z(k_x, k_y)e^{i(k_x x + k_y y)} \, dk_x dk_y \, . \tag{2.12}$$
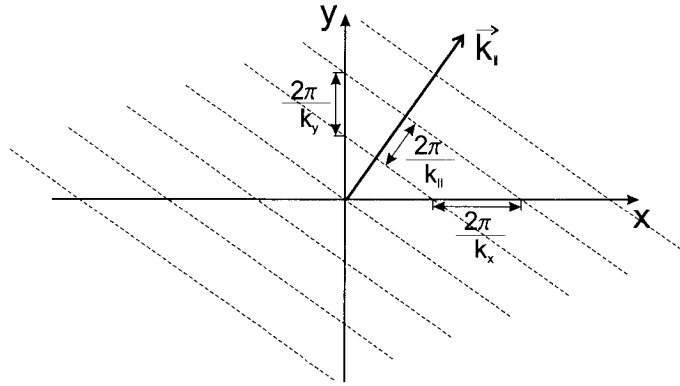
Figure 2.2: Zero-phase lines of a plane wave in the object plane.

The relation between $\vec{A}_z(k_x, k_y)$ and $\vec{A}_0(k_x, k_y)$ is determined by Maxwell's equations. For propagation within a linear, isotropic, homogeneous, non-dispersive and non-magnetic dielectric medium the Helmholtz wave equation $\nabla^2 \vec{E} + k^2 \vec{E} = 0$ has to be satisfied [55]. Direct application of this requirement to equation 2.12 shows that $\vec{A}$ must satisfy the differential equation

$$\left(\frac{d^2}{dz^2} + k_z^2 \right) \vec{A}_z(k_x, k_y) = 0, \tag{2.13}$$

which describes the evolution of the angular spectrum $\vec{A}$ in z-direction. A general solution of this equation is given by

$$\vec{A}_z(k_x, k_y) = \vec{A}_0(k_x, k_y) \cdot \begin{cases} e^{-ik_z z} & , \quad z < 0 \\ \underbrace{e^{+ik_z z}}_{propagator} & , \quad z > 0 \end{cases} \tag{2.14}$$

The angular spectra of the object plane and an arbitrary parallel image plane are connected by a factor which is called propagator. The '±' signs in the exponents specify two solutions which correspond to a wave propagation into the half-spaces $z > 0$ and $z < 0$, respectively. The positive sign has to be chosen in case of propagation in the homogeneous half-space $z > 0$ in order to ensure that the integral in equation 2.12 converges even in the case of imaginary k_z, an analogous argumentation holds for the negative sign for $z < 0$. This corresponds to the boundary condition that $\vec{A} \to 0$ for $z \to \pm\infty$. Choosing the image plane in the positive half

space reduces equation 2.14 to $\vec{A}_z(k_x, k_y) = \vec{A}_0(k_x, k_y)e^{ik_z z}$ which can be introduced into equation 2.12 yielding the field distribution in the image plane:

$$\vec{E}(x, y; z) = \frac{1}{2\pi} \int \int \vec{A}_0(k_x, k_y)e^{ik_z z}e^{i(k_x x + k_y y)} \, dk_x dk_y \,. \qquad (2.15)$$

2.2.3 Near-field and far-field region

Two regions in the frequency space should be distinguished because of the completely different propagation-behavior of the corresponding angular spectrum components of an optical field.

Region 1: $\sqrt{k_x^2 + k_y^2} > \frac{2\pi n}{\lambda}$ or analogous k_z is imaginary.

For high spatial frequencies k_x, k_y complying with this condition the propagator turns into an exponentially decaying function. Components of the angular spectrum within this region are called evanescent waves. The contribution of evanescent wave components to the angular spectrum is strongly attenuated during the propagation in z-direction and is negligible if the distance between object plane and image plane is sufficiently large (rule of thumb: $z > \lambda$). In other words, high spatial frequencies of the original field are filtered out during the propagation process which can therefore be regarded as a low-pass filtering. The region in space where these high frequency components are lost is called *far-field*. In direct vicinity to the object plane, where they still contribute to the angular spectrum, the term *near-field* is used.

Region 2: $\sqrt{k_x^2 + k_y^2} \leq \frac{2\pi n}{\lambda}$ or analogous k_z is real.

For these small spatial frequencies k_x, k_y of the original field the corresponding components of the angular spectrum are plane waves. The effect of the propagation over a distance z is simply a phase shift which depends on k_x and k_y. Since each plane wave component travels at a different angle, each has another optical path length between two parallel planes and relative phase delays are thus introduced.

As a consequence, near-field microscopy can theoretically provide with informations about the full range of spatial frequency components comprised in the optical

field in the object plane. In contrast to that far-field microscopy is in pinciple restricted to information about small spatial frequency components.

2.2.4 Evolution of propagating components

In many application like confocal microscopy only propagating components of the angular spectrum are concerned. Considering only the propagating part of the angular spectrum the corresponding field in the image plane is according to equation 2.15, p. 24 given by

$$\vec{E}(x, y; z) = \frac{1}{2\pi} \int\int\limits_{k_x^2 + k_y^2 \leq 2\pi n/\lambda} \vec{A}_0(k_x, k_y) e^{ik_z z} e^{i(k_x x + k_y y)} \, dk_x dk_y \,. \qquad (2.16)$$

To calculate an asymptotic far-zone approximation $\vec{E}_\infty$ for $r = \sqrt{x^2 + y^2 + z^2} \to \infty$ the method of stationary phase can be used which is described in [72]. Only the result shall be presented here saying that the optical field far away from the object plane is linked to the angular spectrum in the object plane by

$$\vec{A}_0(k_x, k_y) = \frac{ire^{-ikr}}{k_z} \vec{E}_\infty(k_x, k_y, k_z) \,, \qquad (2.17)$$

which implies that only one plane wave with the wave-vector $\vec{k} = (k_x, k_y, k_z)$ determines the far-field at a point located in this direction. Introducing this expression for $\vec{A}_0$ in equation 2.16 leads to the connection

$$\vec{E}(x, y; z) = \frac{ire^{-ikr}}{2\pi} \int\int\limits_{k_x^2 + k_y^2 \leq 2\pi n/\lambda} \frac{\vec{E}_\infty(k_x, k_y, k_z) \, e^{ik_z z} e^{i(k_x x + k_y y)}}{k_z} \, dk_x dk_y \qquad (2.18)$$

between the far-field $\vec{E}_\infty$ and the field $\vec{E}$ in the image plane. This relation shows that, as long evanescent fields are not part of the system, the field $\vec{E}$ and its far-field $\vec{E}_\infty$ form almost a Fourier transform pair. In the paraxial approximation $k_z \approx k$, $\vec{E}$ and $\vec{E}_\infty$ form a perfect Fourier transform pair.

The field-distribution in the focal region of a high numerical aperture lens, like used in high resolution confocal microscopy, can be calculated with help of equation

2.18, even if the paraxial approximation is not valid in this case (see chapter 6.4.1 for a detailed discussion).

2.2.5   Point spread function of an optical imaging system

The image properties of a microscope can be quantified by its point spread function (PSF) $\vec{h}$, which is the image-field $\vec{E}_i^\delta$ resulting by imaging a single point positioned at x_0, y_0 in the object plane. The following arguments and formulas are valid for each component of $\vec{h}$, $\vec{E}$ and $\vec{A}$.

$$h_z(x_i, y_i; x_0, y_0) = E_i^\delta(x_i, y_i) \ , \tag{2.19}$$

where z denotes the position of the image plane, and x_i, y_i are the spatial coordinates in the image plane. Knowing the PSF and relying on the linearity of wave propagation, the image field-distribution E_i, resulting from an arbitrary field distribution E_0 in the object plane, can be calculated by a superposition integral of E_0 and the PSF h [39]:

$$E_i(x_i, y_i) = \int \int h_z(x_i, y_i; x_0, y_0) \, E_0(x_0, y_0) \, dx_0 dy_0 \ . \tag{2.20}$$

For optimal imaging, as described in section 2.2.1, the PSF h should be a Dirac delta function $h \propto \delta(x_i + Mx_0, y_i + My_0)$, where M is the magnification factor. This means that the image of a point is a point and only the distance between two points in the image is by the factor M larger than in the object.

A point in the object plane is mathematically represented by a field with $E_0 = \delta(x, y)$. The angular spectrum of a delta function is uniform: [39]

$$A_0^\delta(k_x, k_y) = \mathcal{F}\left(\delta(x, y)\right) = \frac{1}{2\pi} \int \int \delta(x, y) e^{-i(k_x x + k_y y)} \, dx dy = \text{const} \ \forall k_x, k_y \ . \tag{2.21}$$

The PSF is given by the inverse Fourier transform of the corresponding angular spectrum A_z^δ in the image plane, which is calculated by introducing A_0^δ into equation

2.14, p. 23 resulting in:

$$A_z^\delta(k_x, k_y) \propto e^{i\,k_z\,z} \,.$$
(2.22)

PSF in the near-field:

The idea of near-field techniques like scanning tunneling optical microscopy (STOM) is to pick up the optical field directly at the object-plane. In the ideal case all components of the angular spectrum can be collected, which results in a near-field PSF h_n, which is a Dirac delta function obtained by inverse Fourier transformation of the detected uniform angular spectrum. To achieve an arbitrary magnification M, it is sufficient to stretch the scale of the image. Accordingly, beside technical difficulties there is no fundamental obstacle to get a perfect optical image by near-field microscopy. With increasing distance z, more and more high frequency components get lost, which causes a narrowing of the angular spectrum connected with a broadening of the obtainable PSF h_n.

PSF in the far-field:

Due to the discussed frequency filtering, from the original infinite angular spectrum only the inner circular part with $\sqrt{k_x^2 + k_y^2} \leq \frac{2\pi n}{\lambda}$ arrives at the far-field. For this reason the angular spectrum A^δ in the far-field is given by a circle function (see figure 2.4 (a))

$$A_{z>\lambda}^\delta(k_x, k_y) \propto \mathrm{circ}\left(\frac{\lambda}{2\pi n}\sqrt{k_x^2 + k_y^2}\right) = \begin{cases} 1 & , \quad \frac{\lambda}{2\pi n}\sqrt{k_x^2 + k_y^2} \leq 1 \\ 0 & , \quad \text{otherwise} \end{cases} \,.$$

The PSF h_f in the far-field is given by the inverse Fourier transform of this constricted spectrum $A_{z>\lambda}^\delta$. The result is therefore not a point but a pattern of finite size as determined by inverse Fourier transformation. In practice, when working with a lens with a specified numerical aperture NA, not all components of the propagating angular spectrum can be collected which further reduces the bandwidth to $\sqrt{k_x^2 + k_y^2} \leq \frac{2\pi NA}{\lambda}$. This can be illustrated if considering a lens (L) specified with a numerical aperture NA being used with an immersion medium having a refraction index n. According to the definition of the numerical aperture ($NA = n\sin\theta$), only
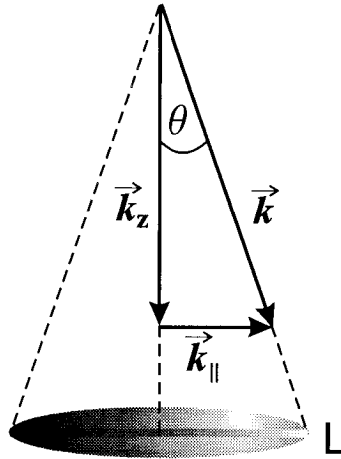
Figure 2.3: Lens with collection angle θ: only a restrained part of the angular spectrum is collected.

plane waves at an angle of incidence smaller then θ with respect to the optical axis z are collected by the lens (see figure 2.3). For this reason the border plane wave for collection by the lens has a wave vector $\vec{k}$ with a component $k_{\parallel} = \sqrt{k_x^2 + k_y^2}$ for which

$$k_{\parallel} = |\vec{k}| \cdot \sin\theta = \frac{2\pi n}{\lambda} \cdot \frac{NA}{n} = \frac{2\pi NA}{\lambda} \quad .$$

In figure 2.4 (a) the distribution of the angular spectrum is depicted. The PSF h_f for such a far-field imaging system is given by the inverse Fourier transform of the *collected* circular angular spectrum [39]:

$$h_f(x,y) = E^\delta(x,y; z > \lambda) \propto \mathcal{F}^{-1}\left\{ \text{circ}\left(\frac{\lambda}{2\pi NA} \sqrt{k_x^2 + k_y^2} \right) \right\} = \frac{J_1\left(\frac{2\pi NA}{\lambda} \sqrt{x^2 + y^2} \right)}{\frac{2\pi NA}{\lambda} \sqrt{x^2 + y^2}} ,$$

where J_1 is the bessel function of first kind and first order. An optical image shows the intensity, which is the square of the field,

$$I^\delta(x,y) = [h_f(x,y)]^2 \propto \left[\frac{J_1\left(\frac{2\pi NA}{n\lambda} \sqrt{x^2 + y^2} \right)}{\frac{2\pi NA}{n\lambda} \sqrt{x^2 + y^2}} \right]^2 \quad . \qquad (2.23)$$

This intensity distribution is refered to as *Airy-pattern* and is shown in figure 2.4 (b). The diffraction limited width of an Airy-pattern can be characterized by the distance $(\Delta = 0.61\frac{\lambda}{NA})$ between the central peak and the first minimum. As a definition for the confinement of the field or the resolution of an imaging system it is more appropriate to take the full width at half maximum (FWHM) of the central intensity peak

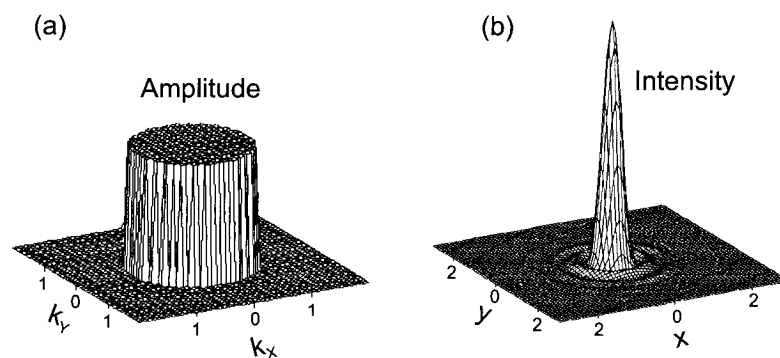$$\text{FWHM} = 0.51\frac{\lambda}{NA} \, . \tag{2.24}$$

Figure 2.4: (a) Two-dimensional distribution of the angular spectrum of an imaged point-object in the far-field. The variables k_x and k_y are normalized and must be multiplied by the factor $\frac{2\pi NA}{\lambda}$ to get the collected angular spectrum if working with lens with numerical aperture NA. (b) Corresponding two-dimensional diffraction-limited intensity distribution of an imaged point-object in the far-field (Airy-pattern). The distances x and y to the center are normalized and must be multiplied with the factor $\frac{\lambda}{NA}$ to get absolute values. The spatial intensity distribution in (b) is proportional to the squared Fourier transform of the angular spectrum depicted in (a).

The FWHM of the PSF is a criterion for the resolution of the microscope, because it implies, that the images of two equally bright points are separated by a dip to half of the maximal intensity, if the points in the object plane have a distance given by the FWHM. In conclusion the optical resolution of a far-field microscope is limited to about half of the wavelength used. Of course, choosing a dip of 50% is arbitrarily. The Rayleigh limit is based on a dip of 26% and results in a better

resolution. In a more realistic view including noise, the dip has to be deep enough to be clearly visible. Thus the resolution is finally limited by the SNR in an image.

3. Instrumentation

The theoretical background and the actual realization of microscopy techniques implemented within this work are discussed. For this purpose an introduction into scanning confocal optical microscopy (SCOM) and scanning near-field optical microscopy (SNOM) is presented. A home-made instrument which combines SCOM and SNOM is discussed. High resolution imaging and the suitability for single-molecule studies is demonstrated. Moreover, the fabrication process of the near-field optical probes by tube-etching is described in detail.

The part about the tube-etching technique is based on [113].

3.1 Scanning confocal optical microscopy

3.1.1 Introduction

In scanning confocal optical microscopy (SCOM) [125] the sample is moved pointwise through a confined illumination volume while recording the optical information point by point. In figure 3.1 the principle of SCOM is illustrated. A diffraction limited excitation volume is created by imaging a point-like light source (P_1) via an objective lens (O) into the object plane. The light interacts with the matter within the excitation volume (e.g. with an object marked with A in figure 3.1(b)) and the resulting optical field is collected by the same objective lens and imaged onto a detector (D) with a point-like active area (P_2). Objects outside of the focus (like B and C in figure 3.1 (b)) are hardly excited and moreover they are not imaged onto the point-detector resulting in an inefficient detection and a very good suppression of background. For these reasons SCOM allows for non-invasively imaging different object planes within a thick sample (3-dimensional sectioning). A dichroic mirror
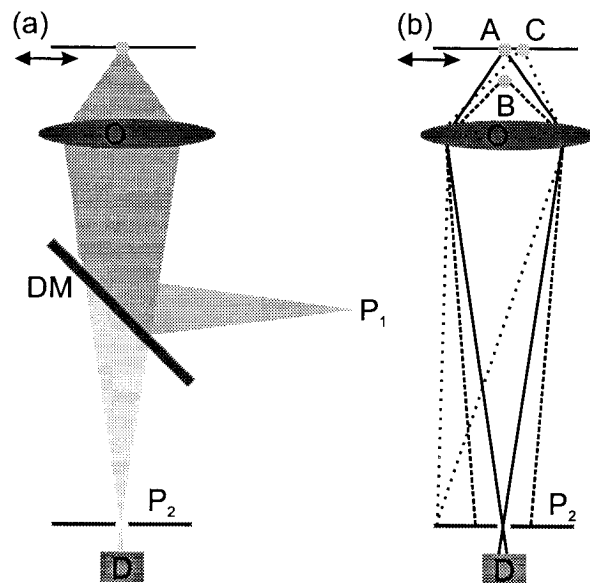

Figure 3.1: Principle of SCOM: (a) The focus is created by imaging a point-like light source P_1 via an objective lens O into the object plane. Light from the focal region is collected by the same objective lens filtered by a dichroic mirror DM and detected by a detector D with a point-like active area P_2. (b) Light emerging from out of focus objects like B and C is hardly detected.

(DM) which reflects the excitation light and transmits red-shifted light allows for recording fluorescence images. SCOM belongs to the family of far-field microscopy techniques because the size of the excitation volume is diffraction limited and the optical information is collected by an objective lens positioned in the far-field of the object.

3.1.2 Theory

According to equation 2.20, p. 26 it is sufficient to determine the point spread function of the microscope for a quantitative characterization of the imaging process. The intensity pattern of the PSF in a confocal microscope is produced by scanning a point-object through the focus and detecting the resulting intensity at each point by a point-like detector. Because the focus is created by imaging a point-like light source into the object plane the spatial distribution of the excitation intensity is given by an Airy-pattern (see equation 2.23, p. 28) centered around the optical axis. The image of a point-object in the object plane at the detector plane is again an Airy-pattern with a peak-intensity directly proportional to the excitation intensity. The position of the image depends on the position of the point-object within the focal region. Only if the point-object is on the optical axis, the projected Airy-pattern is centered above the point-detector. Otherwise only intensities in the flank of the Airy-pattern are measured by the detector. In conclusion the intensity of the PSF h_c of a confocal microscope is proportional to a squared Airy-pattern[1] because both the excitation and the detection efficiency have a position dependency within the focus which is determined by an Airy-pattern shape centered around the optical axis.

$$I^\delta(x,y) \sim [h_c(x,y)]^2 = \left[\frac{J_1\left(\frac{2\pi NA}{\lambda} \sqrt{x^2 + y^2} \right)}{\frac{2\pi NA}{\lambda} \sqrt{x^2 + y^2}} \right]^4 \tag{3.1}$$

---

[1]To be rigorous, in fluorescence microscopy there are actually two different λ, the excitation wavelength in the case of the excitation PSF and the fluorescence wavelength in the case of the detection PSF.

Generally speaking, the total point spread function of an imaging system can be regarded as the product of the excitation point spread function and the detection point spread function,

$$\text{total–PSF} = \text{excitation–PSF} \cdot \text{detection–PSF} . \tag{3.2}$$

This means that the PSF of a confocal microscope is proportional to the squared PSF of a wide-field microscope. The distance between the central peak and the first minimum in the case of a squared Airy-Pattern is again $\Delta = 0.61\frac{\lambda}{NA}$. Nevertheless the resolution is slightly enhanced considering the full width at half maximum of the central peak in the intensity pattern (see figure 3.2). Compared to the wide-field $\text{FWHM}_w = 0.51\frac{\lambda}{NA}$, the confocal $\text{FWHM}_c = 0.37\frac{\lambda}{NA}$ is reduced by a factor of 1.3. However, the main difference between wide-field and confocal microscopy
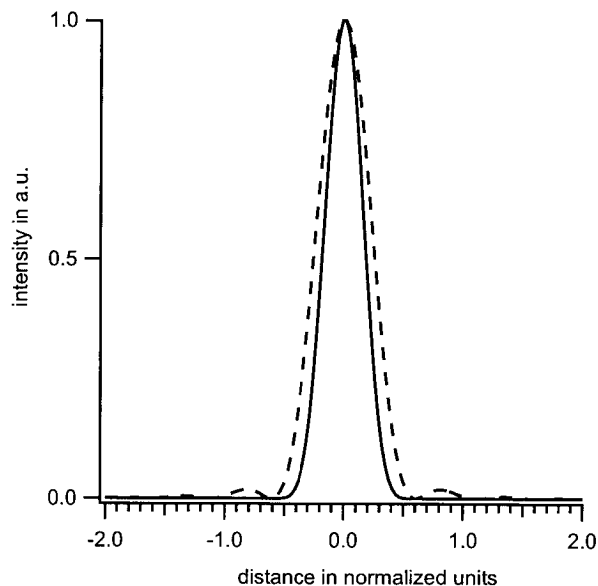

Figure 3.2: Profiles through the center of calculated PSF-intensity distributions in the image plane in case of confocal microscopy (solid line) or wide-field microscopy (dashed line). The distance from the center is normalized and must be multiplied with the factor $\frac{\lambda}{NA}$ to get real distances.

is the fact that confocal imaging allows for optical sectioning [128]. Confocal microscopy provides with a resolution in z-direction, which can be characterized by the $\text{FWHM}_z = 1.26\frac{n\lambda}{NA^2}$ [125].

3.2 Scanning near-field optical microscopy

3.2.1 Introduction

Limitations of the optical resolution due to diffraction is a far-field effect (see section 2.2.5, p. 26). Scanning near-field optical microscopy (SNOM) allows for optical imaging with resolution beyond the diffraction limit. The key idea was proposed 1928 by Synge [114] when he suggested to perform optical measurements in the near-field of a sub-wavelength hole in an opaque screen which is illuminated from the back side. In the middle eighties this idea was reinvented and experimentally realized by Pohl [91], and independently by Lewis [65]. In figure 3.3 the principle of SNOM is illustrated. By illuminating a sub-wavelength aperture in an opaque screen the
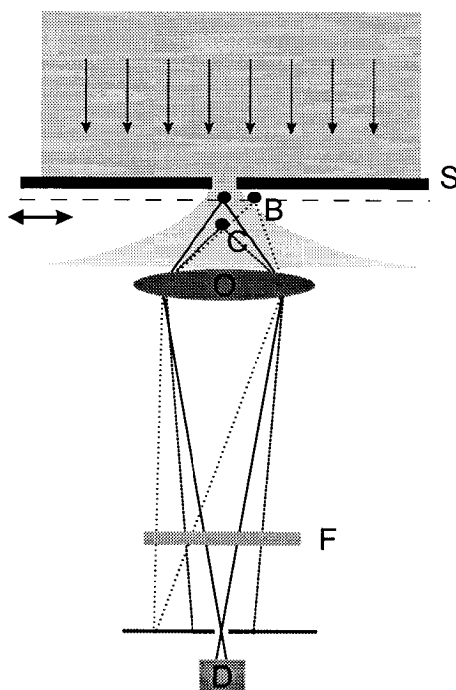

Figure 3.3: Principle of SNOM: An opaque screen (S) with a sub-wavelength aperture is illuminated from above. The sample is scanned in close proximity beneath the aperture (distance $\ll \lambda$), whereby the dimensions of excitation volume is given by the aperture size. An objective lens (O) collects the light from the focal region which is centered beneath the aperture. The light passes a filter (F) and is imaged onto a point-like detector (D). Objects like B and C which are not in the near-field of the aperture are hardly excited and moreover they are inefficiently detected if they are out of focus.

light will, in close proximity to the screen, be constrained to the dimensions of the opening. This strongly confined excitation volume can be exploited by scanning the sample directly beneath the aperture. The light interacts with the matter within the excitation volume and the resulting optical field is collected by an objective lens (O), filtered by a filter (F) and imaged onto a detector (D). Objects outside the near-field of the aperture marked with B and C are hardly excited. The small excitation volume implies a high optical resolution. Because the excitation volume is bound to the aperture, SNOM requires controlling the distance between aperture and sample. This finally results in a combined topographical and optical image of the sample-surface.

3.2.2 Theory

Like confocal microscopy SNOM is based on selective spatial illumination. As pointed out in section 3.1 the point spread function in microscopy is equal to the product from the excitation PSF and detection PSF (see equation 3.2) whereby the FWHM of the squared PSF characterizes the resolution. Only with respect to the excitation scheme there is a difference between SCOM and aperture SNOM (compare figures 3.1, p. 32 and 3.3, p. 35). In aperture SNOM the confined excitation volume is defined by the near-field behind a sub-wavelength aperture e.g. in an opaque screen which is illuminated from the other side. The field distribution behind a circular aperture in an ideally conducting, infinity large and infinity thin screen was rigorously calculated by Bethe and Bouwkamp [13, 20] in the late forties. Since this time the Bethe/Bouwkamp closed analytic solutions of this model are mostly used to describe the field-distribution in aperture SNOM. However, the aperture of a realistic near-field probe is positioned at the apex of a tapered waveguide coated with $\sim 100\,nm$ metal, rather than in a flat, infinity large and thin screen. According to the Bethe/Bouwkamp model, the resulting field-distribution behind a sub-wavelength aperture is inhomogeneous even for illumination with a plane wave. Figure 3.4 illustrates the spatial distribution of different electric field components in the optical near-field of an aperture. The field distribution in a plane beneath
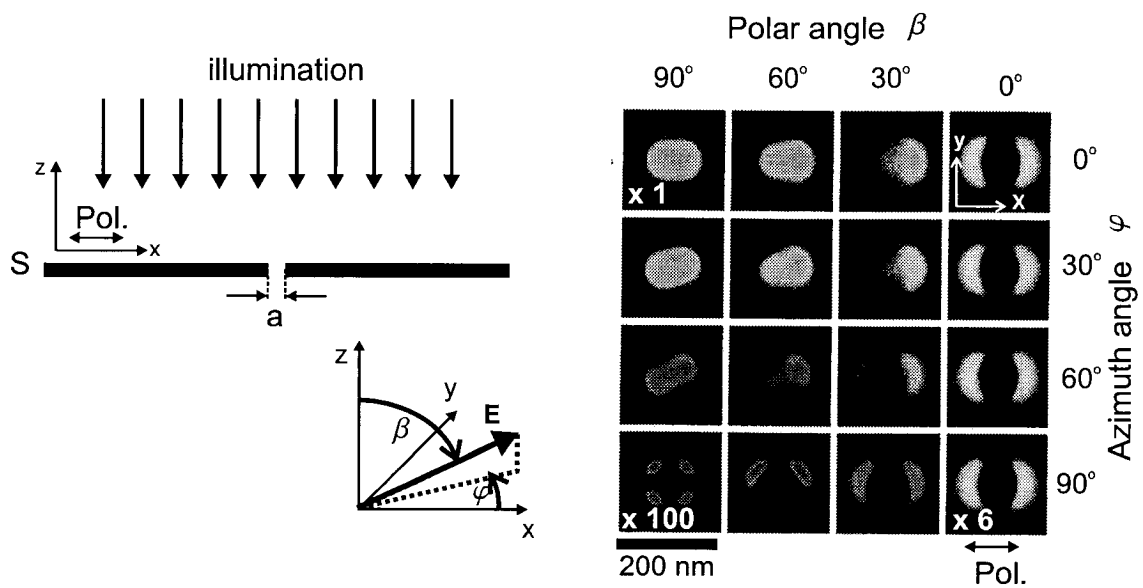
Figure 3.4: Inhomogeneous field-distribution in the optical near-field of a sub-wavelength aperture: According to the Bethe/Bouwkamp model an opaque screen (S) is illuminated by a planar wave, here assumed to be linearly polarized in x-direction. The matrix shows the solutions according to the Bethe/Bouwkamp model of the spatial intensity distributions of various electric field-components in 15nm distance to the aperture plane for an aperture diameter of $a = 100$nm and $\lambda = 515$nm (the image is taken from [124]). The intensities of the distributions shown are normalized, which is indicated by the scaling factors in some of the patterns. The orientation of the corresponding electric field-component E is described by the angles β and φ which are defined in the depicted coordinate system.

the aperture depends on the wavelength, the aperture size and the distance to the aperture.

In the case of a *sub-wavelength* aperture the field is strongly confined to the direct surrounding of the aperture. This can be explained in terms of Fourier optics. In a small aperture the field is strongly spatially confined in the xy-plane of the screen and has therefore a broad angular spectrum $A(k_x, k_y)$ (see section 2.2). Only those components of the angular spectrum corresponding to small spatial frequencies k_x, k_y complying with $\sqrt{k_x^2 + k_y^2} \leq \frac{2\pi n}{\lambda}$ propagate into the far-field (see section 24, p. 24). The smaller the aperture and correspondingly broader the angular spectrum is, the more components have high spatial frequencies complying with $\sqrt{k_x^2 + k_y^2} > \frac{2\pi n}{\lambda}$ and therefore have an amplitude with exponentially decay with respect to the distance z to the aperture plane ($\propto e^{-\sqrt{|(\frac{2\pi n}{\lambda})^2 - k_x^2 - k_y^2|} \cdot z}$, see section 2.2.3 f.) which becomes all the steeper the larger k_x, k_y are. For this reason the intensity in the near-field of sub-wavelength apertures decays rapidly leading to a very confined excitation volume, not only laterally but also along the optical axis. Another parameter depending on the aperture size is the transmission coefficient, which is defined as ratio of the light intensity before passing the aperture and the intensity in the far-field. According to the Bethe/Bouwkamp model this dependency is described by a power-law of fourth order in the aperture size [13, 20, 62]. For this reason it is expected that small apertures have strongly confined near-fields but also low transmission to the far field.

3.3   Setup

An instrument was implemented which combines SCOM and SNOM. A scheme of
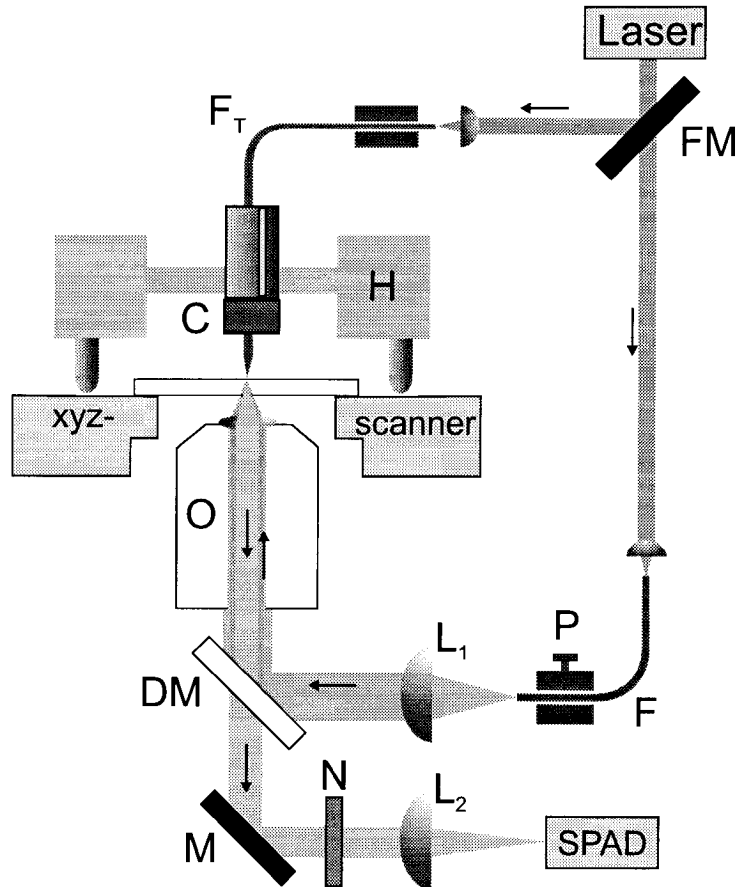the setup is shown in figure 3.5.

Figure 3.5: Setup for the SCOM/SNOM combination: The components used for
SNOM as well as for SCOM are a laser, a xyz-scanner, an objective lens (O), a
dichroic mirror (DM), a notch filter (N) and a lens (L_2) for focusing the fluorescence
light onto a single photon avalanche diode (SPAD). With a flip-able mirror (FM)
it can be chosen between SCOM or SNOM illumination. In the case of SCOM the
illumination path contains a fiber (F) which goes through a polarization controller
(P). A collimated beam produced by a lens (L_1) is focused by the objective lens. In
the case of SNOM the laser light is coupled into a fiber (F_T) which has a near-field
tip at the far end which is mounted in a SNOM-head (H). The sample-tip distance
is controlled by a controlling unit (C) relying on shear-force detection.

A laser (either a continuous wave Ar^+ laser (Coherent Innova 90) or a pulsed
Nd:YAG laser (Coherent Antares, Palo Alto, CA)) is used as light source. With a

flip-able mirror (FM) it can be chosen between SNOM or SCOM mode. In the case of doing SCOM the laser light is coupled into an optical fiber (F) (91-9116.136 Alcatel), which goes through a polarization controller (P) (PLC-003, LOT Oriel) allowing for adjusting an arbitrary wanted polarization state at the end. The $3\mu m$ diameter inner core of the fiber at the far end serves as point-like light source which is imaged into the object plane. In compliance with equation 2.24, p. 29 the infinity corrected immersion oil objective lens (O) (Leica, $NA = 1.3$, $\times 100$, $f_O = 2mm$) determines the full width at half maximum of the smallest achievable image pattern,

$$\text{FWHM} = 0.51 \frac{\lambda}{NA} = 202\text{nm} , \qquad (3.3)$$

where $\lambda =$514 nm is used. To ensure a diffraction limited focus a lens (L_1) with focal length $f_1 = 50$mm is chosen, which yields together with the objective lens a magnification $M_1 = f_O/f_1 = 1/25$. In conclusion, the nominal diameter of the fiber-core image is 120 nm, and with that clearly beyond the diffraction limit.

In the case of doing SNOM the light is coupled into a fiber F_T (FS-SN-3224, 3M) with a near-field optical probe at its far end. The resolution is determined by the aperture size of the optical probe. The optical probe consists of a tapered end of the optical fiber, coated with aluminum, with a sub-wavelength aperture at the apex. The fabrication process and the properties of these probes are discussed in section 3.4. For doing optical near-field measurements the sample has to be positioned within the near-field of the sub-wavelength aperture and the sample-aperture distance has to be kept constant while scanning the sample beneath the aperture. For this purpose a SNOM-head is utilized, which contains a tip mounting assembly and a tip-sample distance control relying on shear-force detection. This SNOM head was designed, realized, and discussed previously [48].

The detection part is the same for both, SCOM and SNOM. The fluorescence light emerging from the excitation volume is collected by the objective lens and subsequently filtered. The dichroic mirror (DM) reflects excitation light and transmits fluorescent light which is further filtered by a holographic notch-filter (N) (Kaiser Optical Systems, INC., HNPF-12969) strongly suppressing a sharp spectral region around the laser wave-length. A single-photon counting avalanche photo

diode (SPAD) (SPQ 141, Perkin Elmer) with less than 100 dark-counts per second is chosen as detector on account of its high quantum efficiency of $\sim$70% at 630 nm. The fluorescence light is focused by the lens L_2, which has a focal length of f_2=300mm, onto the 200μm large active area of the SPAD serving as confocal aperture. The size of the back-projected image of the active area into the object plane is about 1μm in diameter, which contains the area of the focal region. Because of the reversibility of light paths this imply, that the image pattern of a point-object at an arbitrary position within the focal region hits the active area. In other words the detection efficiency or the detection PSF is constant for all positions within the illumination volume. In this case the total PSF is equal to the excitation PSF, and therefore a recorded scanning image of a point-object is actually an image of the distribution of the excitation field within the focal region, which can be exploited for experimentally determining distributions of field-components (see chapter 6.4.1). With this choice of the lens L_2 the total PSF of the SCOM is given by an Airy-pattern, as opposed to a squared Airy-pattern, which can be achieved in this configuration of SCOM with the large active area of the SPAD, if working with a lens with about three-times longer focal length. In spite of the slightly reduced resolution (factor 1.3), this design was chosen, because $\sim$ 30% more photons are detected from an imaged point-source, which is a clear advantage if working with single molecules.

The home-built xyz–scanner for sample scanning is based on stack piezos (Physik Instrumente) allowing for a scan range of 60$\times$60μm in x-y-direction and 12μm in z-direction. The use of inductive position-sensors for the x- and y-direction in combination with a closed-loop feedback system (Physik Instrumente) provides linear scan movements, high positional accuracy and eliminates long-term drifts. The design of the scanner was developed by R. Brunner at the university of Ulm.

3.4   Preparing SNOM tips by tube etching

3.4.1   Introduction

In many of today's near-field optical microscopes the optical probe with a sub-wavelength aperture at the apex is the most delicate component [15, 92]. Great efforts have been devoted to the micro-fabrication of near-field optical (NFO) probes [76, 81]. However, few of the present designs are commercially available or have actually been used in experiments. The most widely used optical probes in SNOM are tapered optical fibers, coated with aluminum, which have a sub-wavelength aperture at the apex. Desirable properties of such aperture probes are high brightness, obtained by large cone angles [52, 82, 84, 135], a well defined circular aperture, no light leaking through pinholes in the metal coating [122], and a high optical damage threshold. Several methods have been proposed to prepare the tapered glass core necessary for NFO probes. Most popular up to now is the adiabatic pulling of optical fibers during heating with a CO_2 laser [14, 119].

A different method is based on etching bare glass fibers at the meniscus between hydrofluoric acid (HF) and an organic overlayer (Turner method) [52, 117] (see figure 3.6). A taper is formed due to a decreasing meniscus height as the fiber diameter is reduced by the etchant. Variation of the organic solvent influences the resulting tip geometry. Fiber probes produced by etching usually provide higher optical throughput due to larger cone angles [52, 82, 84, 135]. A well known problem of etched Turner tips is the sensitivity of the tip shape to environmental influences such as vibrations, temperature drifts etc. during the etching, resulting in a glass surface with a considerable roughness. This roughness and the asymmetry of the tip apex are generally held responsible for pinholes in the subsequently applied aluminum coating and ill–defined optical apertures, respectively.

A new process for tip formation, called tube–etching, was developed that overcomes these problems [64, 113] and is described in the following. Essentially it relies on etching the optical fiber within its polymer coating. Consequently, the whole etching process takes place inside a tube formed by the fiber's protective polymer coating that withstands degradation by the etching solution.
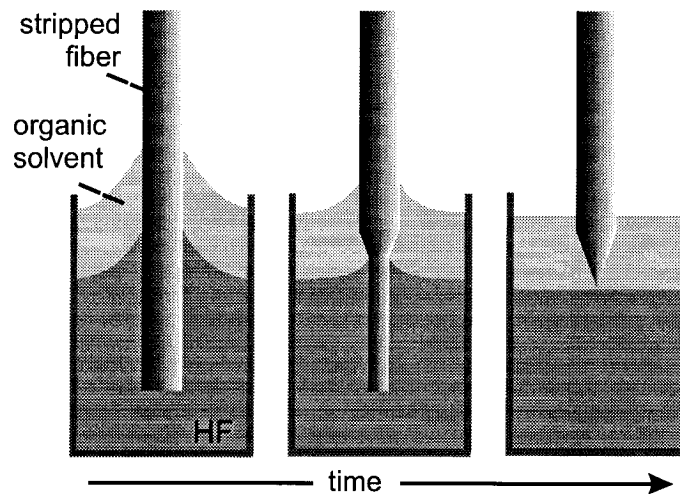
Figure 3.6: Tip formation by the Turner method.

3.4.2 Methods and materials

Five different types of optical fibers were investigated with respect to their suitability for tube etching: Three single mode fibers (FS-SN-3224, inner core diameter 3.36 μm from 3M; 40-692.11, inner core diameter 3 μm from Cabloptic; 91-9116.136, inner core diameter 3 μm from Alcatel) and two multi mode fibers (HCG-M0100T-14, inner core diameter 100 μm from Laser Components; HCG-M0200T-14, inner core diameter 200 μm from Laser Components).

As a stock solution for a series of differently concentrated etching solutions, 40% hydrofluoric acid (HF) (purissimum, Fluka) is used. ISO-octane or p-xylene serves as overlayer to protect the fiber mounts from the corrosive HF vapor. Sulfide acid (98% H_2SO_4, purissimum, Fluka) is used for chemically removing the polymer coating of optical fibers after tip formation.

Without removing the protecting polymer coating the optical fiber is wound up in a home-made fiber-holder (see figure 3.7 (a)), where one end sticks out by $\sim$ 2.5 cm. Eight fiber holders can be mounted in a revolver (see figure 3.7 (b)). The revolver is fixed to the lid of a Teflon vessel containing the etching solution covered with a protecting overlayer (thickness $\sim$ 0.1 $-$ 0.2 cm), in which about 0.6 cm of the protruding fiber is dipped. A batch of eight tips is etched at each time

using $\sim 30\,\text{ml}$ etching solution. The tip formation process is observed through two sapphire windows on opposite sides in the Teflon vessel by a slow scan CCD camera (SensiCam, PCO). Pictures are taken at an acquisition rate of 0.03 Hz. The resulting time-lapse movie of the etching process facilitated the detailed investigation of the tip formation pathways. The etching temperature is controlled by a thermostat to $\pm 0.1°\text{C}$ between 10 and 50°C.
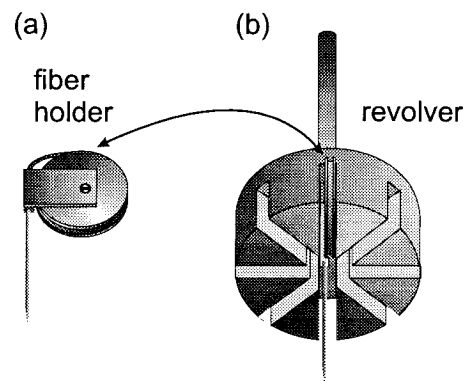

Figure 3.7: Fiber mounting: (a) shows a loaded tip holder, (b) a revolver, in which eight tip holder can be mounted.

After the etching the polymer coating is removed by either dissolving it in hot sulfide acid or by mechanically stripping. The bare tips are investigated by wide-field optical microscopy.

For achieving an aperture at the very end of the tip mostly the shadowing-effect method is used. This method relies on rotating the tapered fibers at an angle relative to a directed metal vapor beam (see figure 3.8). The shadowing-effect results in an aperture which is determined by the shape of the very end of the tip and the quality of the coating process. To perform the coating process the revolver containing the freshly etched tips is mounted at an angle of $\sim 15°$ in a vacuum chamber of an evaporation machine (MCS, BAL-TEC). The evaporation source is a tungsten coil filled with small aluminum rods (see figure 3.9). The revolver rotates with typically 2 Hz during metal deposition takes place with a deposition rate of $\sim 30\,\text{nm/s}$ in case of aluminum. The deposition rate and the thickness of the resulting metal layer is controlled by a quartz gauge. Selected metalized tips are investigated using a
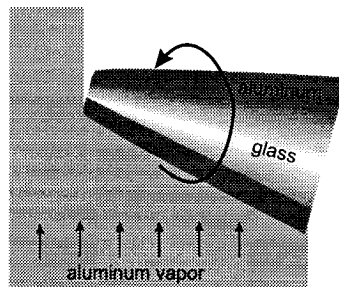
Figure 3.8: Evaporation geometry of the aluminum coating process. Evaporation takes place under a small angle while the tip is rotating. Due to the shadowing-effect an aperture is created at the very end of the tip.

Figure 3.9: Setup for the metalization process inside a vacuum chamber (V). An tungsten coil filled with aluminum rods serves as source (S). The rotation of the revolver (R) is driven by a motor (M). The thickness of the deposited metal is monitored by a quartz (Q).

high-resolution scanning electron microscope (SEM) (Hitachi S41100 at the CSEM Zurich, Hitachi S-700 at the institute of micro-biology ETHZ).

3.4.3 Results and discussion

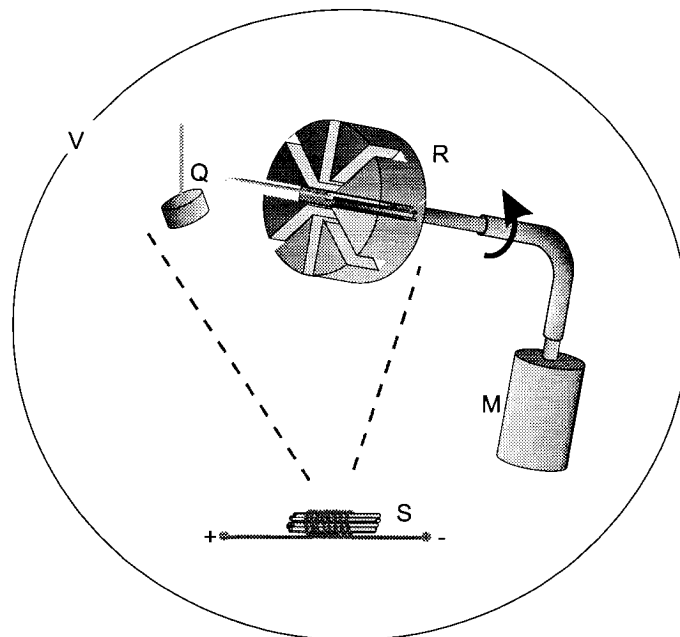To check the permeability of the polymer coating for HF, for each type of fiber a closed fiber loop is dipped into a vessel containing HF. For the two multi mode fibers no etching inside the plastic jacket takes place, whereas the other fibers show severe thinning of the fiber core after 60 minutes in HF, which allows for the conclusion that HF diffuses through their polymer coating.

Tip formation was found to follow two different pathways depending on whether the fiber's polymer coating is permeable for HF or not. Nevertheless, similar tips are obtained independent of the taper formation pathway involved. Figure 3.10 (a) shows the etching process of a fiber with HF impermeable polymer coating; Figure 3.10 (b) the etching process for a fiber with HF permeable polymer coating. For each case the etching behavior is sketched schematically and supported by video frames acquired during the etching process (insets).

If no HF can penetrate through the coating (figure 3.10 (a)) the tip formation starts at the lower end of the fiber. No thinning of the glass in the upper region of the fiber is observed. Once a tip is formed, the tip shape is maintained while the tip shortens inside the tube. The tip quality in terms of sharpness and smoothness does not deteriorate upon further etching; the tube etching process is found to be self-limiting. The scanning electron microscopy (SEM) images in figure 3.11 show aluminum coated optical probes etched for 90 (a) and 130 minutes (b), respectively. It is evident that the taper angle and the surface quality are insensitive to the etching time. This result compares very well with the video frames in figure 3.10 (a). This observation is in contrast to our experience with the Turner method [52, 117] where the tip quality decreases after the tip has been formed, although the process should be self-terminating.

For the HF permeable protective polymer coating the glass fiber is thinned regularly inside the plastic jacket due to diffusion of HF through the jacket as demon-
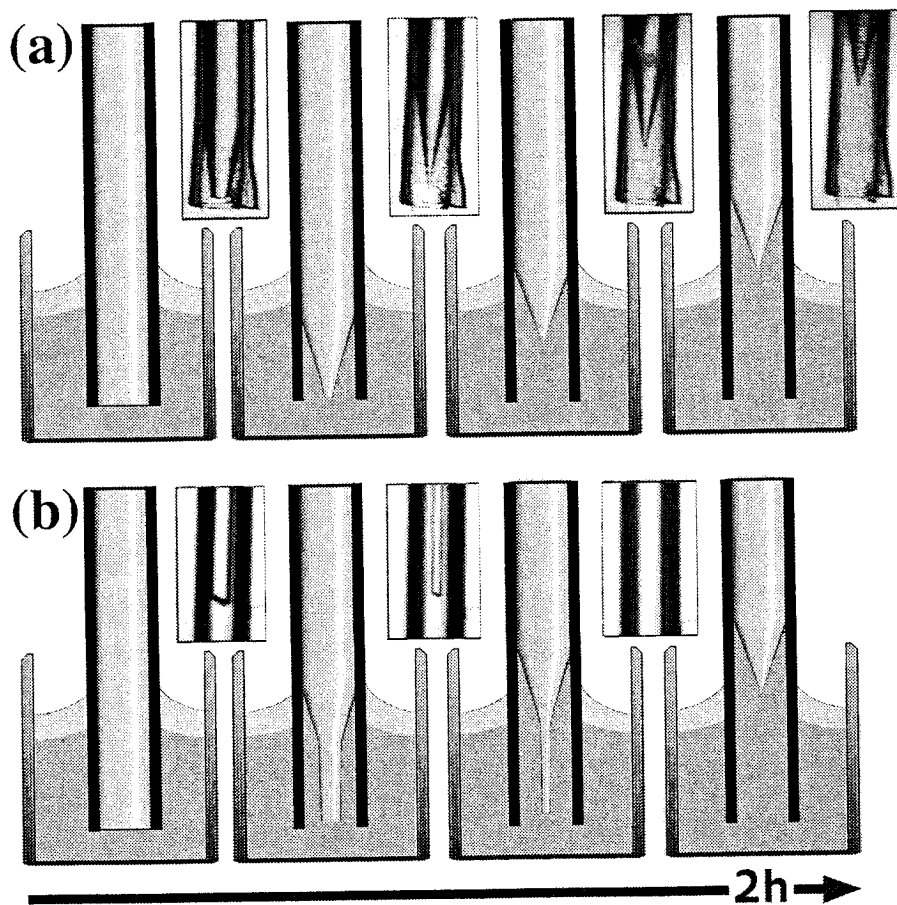
Figure 3.10: Tip formation by tube-etching for different fiber polymer coatings: (a) HF impermeable coating, (b) HF permeable coating. The insets show video frames taken at the fiber part below the meniscus during the etching process.
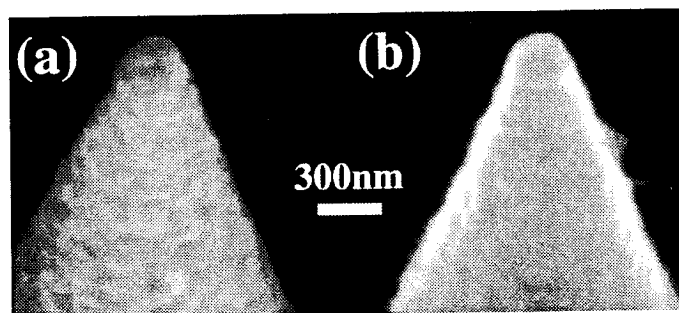

Figure 3.11: Scanning electron micro-graphs of tube-etched tips coated with 100 nm aluminum. They were etched for (a) 90 min. and (b) 130 min., respectively. The surface quality is insensitive to the etching time.

Table 3.1:
Taper angles obtained with different HF concentrations at room temperature

Fiber	40%	34%	28%	21%
3M	22±1	25±1	22±1	20±1
Cabloptic	18±2	23.6±1	20.8±1.5	19.4±1.1
LaserComp. 100μm	22.9±1.2	26±1	-	35.1±1

strated in figure 3.10 (b). A preliminary tip formation at the position of the interface between the HF solution and the organic overlayer can be seen in the same figure. This is possibly due to a gradient in the lateral diffusion along the tip in the meniscus region. The final tip formation takes place *above* the interface after complete removal of the thinned part. It should be noted that above the interface lateral diffusion of HF through the jacket is no longer possible. This suggests that the tip in this region is formed by the same mechanism as in the case of the impermeable polymer coating.

The most prominent result is the finding that the fiber type itself has the strongest influence on the resulting probe quality. Not only the cone angle, but also the resulting surface roughness is strongly dependent on the fiber type used. However, except for the Alcatel and Cabloptic single mode fibers all tested fibers yield extremely smooth glass surfaces after etching.

The influence of the HF concentration and etching temperature on the tip quality and geometry is investigated by etching with differently diluted HF solutions at different temperatures. For each set of parameters 6–8 tips were prepared. Measured values for different concentrations are listed in table 3.1. While the variation of HF concentration and temperature has no influence on the tip surface quality, the cone angle shows a slight dependence on these parameters. For both, temperature and concentration series are found optimum tip shapes for intermediate values (40°C and 34 % HF). Note that the taper angle deviation within a set is generally smaller than 2°. At room temperature the required etching time is between 90 minutes (40% HF) and 15 hours (21% HF). Temperature fluctuations of a few degrees during etching do not show any influence on the resulting tips. Most probably, as the tip formation no

longer occurs at a liquid surface but rather in a self-contained volume, the etching solution acts as a heat buffer allowing only slow, gradual temperature changes.

For explanation a model is proposed, which is based on micro–convection inside the tube, probably in combination with transient capillary effects (see figure 3.12). A similar mechanism was also postulated by Unger et al. [118] for other fiber materials. Initially, due to geometrical constraints, it is expected that the outer regions of the fiber are etched slightly faster than the center. This is attributed to the fact that at the rim of the glass cylinder, HF supply occurs out of a larger volume as compared to the central region (see Fig. 3 (a)). This effect starts the formation of a conical shape
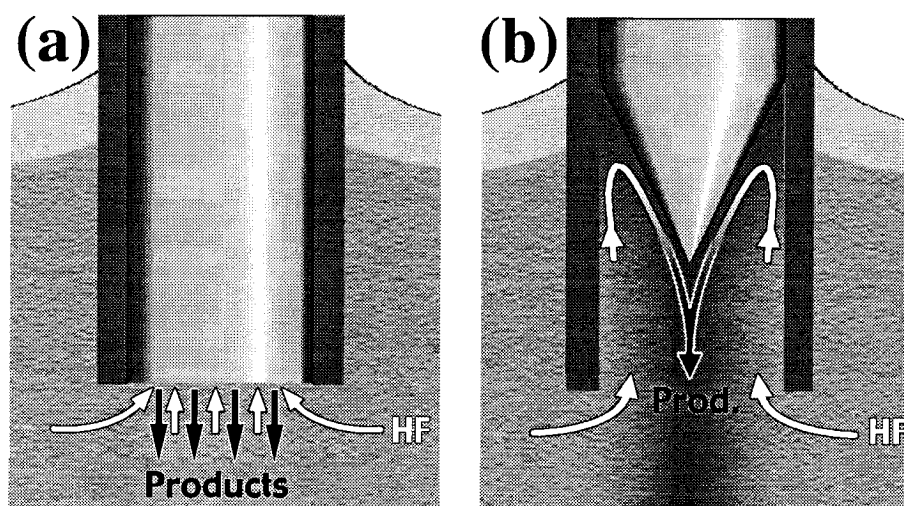
Figure 3.12: Schematic of the proposed convection mechanism involved in tube-etching: (a) Initial diffusion controlled etching, (b) convection-controlled tip formation inside the tube.

(see first inset figure 3.10 (a)). As soon as a preliminary tip is formed, convection starts to deliver HF to the upper region of the cone as shown in figure 3.12 (b). This convection is driven by concentration gradients caused by the etching process itself and the gravitational removal of the reaction products [77]:

$$SiO_2 + 4\,HF \rightarrow SiF_4 + 2\,H_2O$$

$$3\,SiF_4 + 2\,H_2O \rightarrow SiO_2 + 2\,H_2SiF_6$$
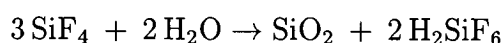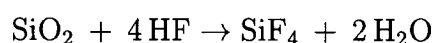
The influence of gravity on the tip formation process is checked by etching the fibers at various angles. Under such conditions asymmetric tip shapes are obtained.

Within the convection model the tip geometry is expected to be determined mainly by the relative magnitude of lateral diffusion and convection as well as the temperature dependence of the etching rate. In the etching region HF is consumed and the reaction products are transported away by gravity. The diffusion of products and educts increases linearly with temperature. The etching rate increases strongly with temperature. An increased diffusion is expected to lead to less sharp tips because of a more isotropic etching of the tip. An increased etching rate is likely to decrease the cone angle because the fresh HF delivered by convection may already be used up at the upper part of the cone *before* it reaches the apex region. As a consequence a maximum cone angle is expected to be obtained for an intermediate temperature. A similar explanation may also hold for the concentration dependence: concentration changes will influence the reaction rate and therefore result in an optimum concentration for a given temperature.

Tube-etching is directly compared to the Turner method by etching unstripped and stripped fibers of the same type (3M-fiber) in the same batch. The resulting tips are also coated in one batch. The tips were investigated optically before metalization and by a high-resolution scanning electron-microscope thereafter. In figure 3.13 the results are presented. The optical images (see top panel) show that the taper angle is quite similar for both techniques, but the tube etched tips are much smoother, evidentially due to the fact that the tip formation is no longer a perturbation-sensitive surface phenomenon but rather takes place in a protected container. This is even more evident in the SEM images of the glass surface recorded in close proximity to the tip apex (middle panels in figure 3.13). In particular, the dramatically increased smoothness of the tips is nicely reflected in the quality of the subsequently deposited $\approx$100 nm aluminum layer (bottom panel). In the case of the tube etched tips, the applied metal coating is virtually free of side holes. Their far-field transmission ranged from $2 \cdot 10^{-4} - 5 \cdot 10^{-3}$ for aperture diameters between 80 and 120 nm. Furthermore, the yield of usable tips after etching is around 80% for tube etching compared to below 40% for the Turner method.
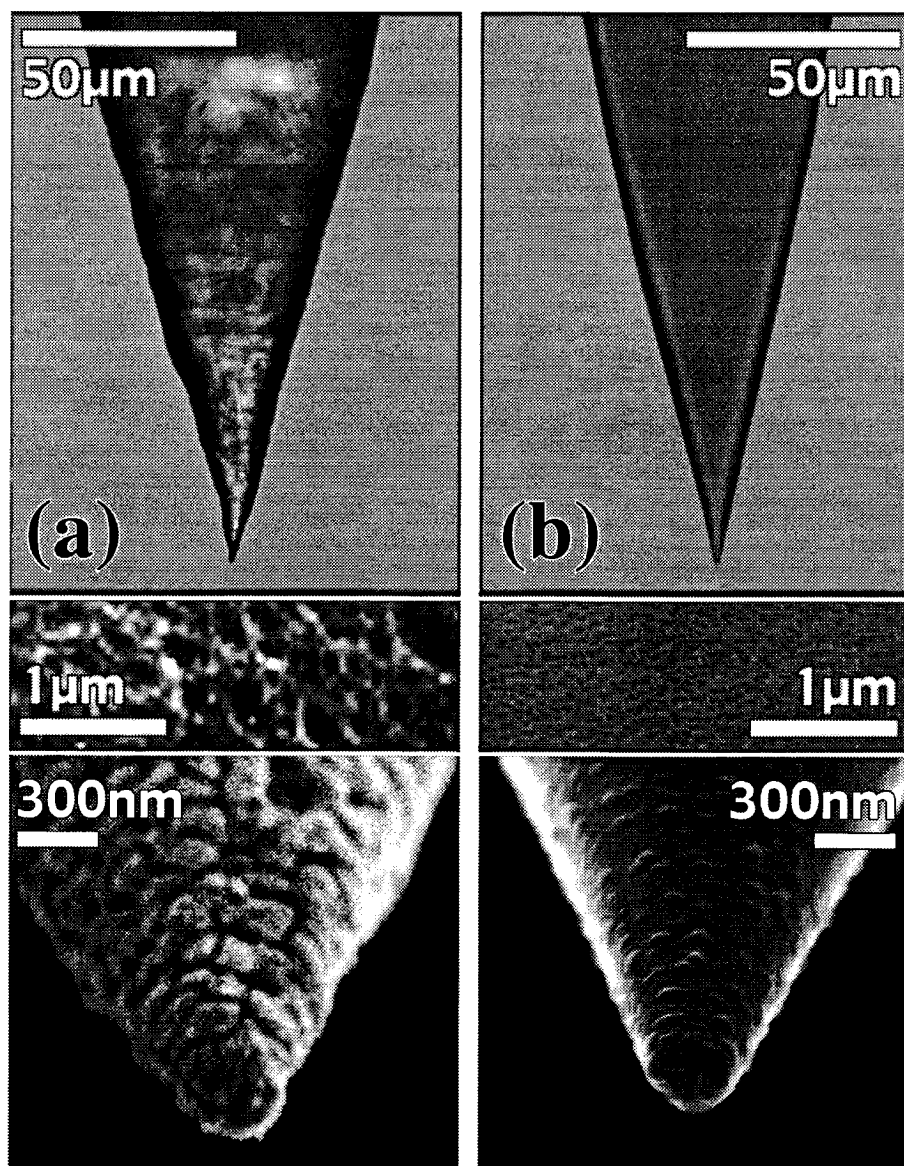
Figure 3.13: Scanning electron and optical micro-graphs of (a) conventionally etched (Turner method) and (b) tube etched fiber probes. Top panel: optical images of uncoated tips. Middle panel: SEM images of the glass surface (3 nm platinum sputtered at 77 K) close to the tip apex. Bottom panel: SEM images of Al coated fiber tips.

The presented results allow for the conclusion that tube etching is a highly reproducible and efficient method to produce near-field optical probes with large cone angles and smooth, side-hole-free aluminum coatings. The method is tolerant against environmental perturbations such as temperature changes and vibrations. The fact that etching time does not influence the tip quality makes the handling of the process straightforward and easy. For a given fiber type the cone angle can to some extent be controlled by varying the etching conditions. However, the main influence on the cone angle seems to result from the actual fiber type; for the same etching parameters the cone angles varied significantly. The smoothness of the glass surface allows to reduce the aluminum thickness and to refine the coating technique. This leads to improved damage thresholds [111] and NFO properties

3.5 Capabilities of the instrument

As discussed in chapter 1 the optical observation of single fluorophores can provide unique information, which would be hidden in ensemble measurements. The technical prerequisite for optimal single-molecule measurements is the capability to simultaneously determine all parameters, which describe a fluorophore: position, orientation of absorption and emission dipole, absorption and emission spectrum, singlet lifetime, triplet lifetime, intersystem crossing rate, fluorescence quantum yield, and photo-bleaching quantum yield.

According to section 3.1, SCOM provides with a far-field technique with diffraction limited x-,y-resolution and corresponding resolution along the optical axis. For this reason it is well suitable for non-invasively investigating fluorophores under ambient conditions at arbitrary positions within a transparent matrix. Within the scope of this thesis the confocal part of the implemented instrument is used for various single-molecule applications. Single molecule sensitivity in SCOM is achieved and demonstrated for different dye species e.g. in figure 4.1, p. 62, figure 5.2, p. 76, or figure 6.6, p.100. The theoretically predicted spatial resolution is experimentally achieved, which is demonstrated in figure 6.7, p. 103 and discussed in section 6.5, p. 107. Capability for determining lifetime and spectral properties with high time resolution is demonstrated for SCOM in chapter 5, p. 69 ff, where a method for rapid identification of single molecules is presented. A reliable method for orientational imaging of single molecules using SCOM is presented in section 6.4.2, p. 104 ff. Moreover it is demonstrated that by utilizing single molecules the instrument allows for mapping confined optical fields on a nanometer scale (see section 6.4.1, p. 99).

As opposed to SCOM, SNOM is a surface sensitive scanning probe technique yielding a combined optical and topographical image of the sample surface, which can provide with resolution beyond the diffraction limit (see section 3.2). However, this implies that SNOM is restricted to investigations of molecules at the surface and that the influence of the optical probe on the fluorophore has to be taken into account (see section 2.1.1). Also for SNOM single-molecule sensitivity is demonstrated (see figure 3.14 (a) and (c)). For imaging with SNOM molecules of the dye *1,1'-dioctadecyl-3,3,3',3'- tetramethylindocarbocyanine* (DiI) were embed-

ded at a concentration of 10^{-7} M in a 20 nm thick film of polymethylmetacrylate (PMMA). The quality and resolution of a SNOM image depends strongly on the used tip. In figure 3.14 (a) the single molecules appear as a distribution of small bright spots. The resolution is estimated to be less than 100 nm by analyzing the FWHM of the intensity profile of the marked molecule in figure 3.14 (a). The image were obtained by using a tube-etched and aluminum coated tip (see section 3.4). The single-molecule image in figure 3.14 (c) was measured with the tip depicted in (e). This tip was treated by focused ion-beam (FIB) milling[2] with the objective to get a smooth end-face for achieving a small sample-aperture distance. The same tube-etched and aluminum coated tip before the FIB-treatment is shown in figure 3.14 (d). Due to the rather poor resolution of the used FIB-instrument ($\sim$ 100 nm) one effect of the treatment is an increased aperture diameter (from $a \approx 80$ nm to $a \approx 250$ nm) and a correspondingly decreased resolution. But the positive effect is the appearance of orientation-dependent image patterns, which are achievable only in close proximity to the aperture [124]. This orientation-dependent image pattern arises because during scanning the fluorophore through the inhomogeneous field distribution beneath a sub-wavelength aperture (see figure 3.4 p. 37) the fluorescence intensity is proportional to the squared electric field component along the molecular absorption dipole at the respective position (see equation 2.1, p. 14). For example the marked double-lobe in figure 3.14 (c) can be assigned to a molecule oriented with its absorption dipole almost along the optical axes, because it maps the electric field component in this direction (see figure 3.4 p. 37). SNOM is therefore suitable for orientational imaging [16, 123], but there is a strong influence of the tip-sample distance and the geometry of the tip itself, which has therefore to be known very precisely.

The capability of SNOM for imaging delicate biological samples is demonstrated by the investigation of micro-contact printed mono-layers of biologically active molecules [12, 25]. This is of interest in biology and biochemistry, because it opens the possibility for nanometer-scale patterning and to carry out chemical assays with minute quantities of reagents [105]. Figure 3.15 shows a simultaneously

---

[2]FIB milling allows for flattening the end-face of a near-field tip by scanning a focused ion-beam perpendicular to the tip axis across the apex of the tip and removing aluminum grains [123].

recorded optical and topographical SNOM-image of micro-contact printed mono-layer-patches of protein molecules, specifically chicken immunoglobulin (IgG) labeled with *tetramethyl-rhodamine-isothiocyanate* (TRITC). To estimate the optical resolution intensity profiles were taken in the optical image (figure 3.15 (a)) along two lines marked by the arrows 1 and 2. The profiles are shown in figure 3.15 (c) and (d) as black lines. The full width at half maximum of the peak in (d) suggests an optical resolution of 50 nm, which was achieved with a standard tube-etched tip. To exclude the possibility of a topographical artefact [49] line-cuts were taken at the same position in the topographical image. The results are shown as gray lines together with the corresponding intensity profiles. Comparing the intensity and height profiles reveals a shift of $\sim$ 100 nm between optical and topographical image. This is an effect, that often occurs in SNOM images. It can be explained by assuming that a small aluminum grain located at the rim of the metal coating acts as the topographical tip shifted by $\sim$ 100 nm against the optical tip which is centered in the aperture. The noise of the height profiles of less than 0.5 nm suggests a z-resolution in this regime. The measured height of $\sim$ 2 nm for a mono-layer of chicken IgG molecules are comparable with results obtained by other groups using atomic force microscopy [12].

3.5.1   Evaluation of the assets and drawbacks of SNOM and SCOM

We demonstrated that both, SCOM and SNOM are suitable for single-molecule measurements. The choice of one of these techniques depends on the problem.

SNOM is better suited if one is interested in the correlation between the topographical and optical properties of a sample surface. The strongly confined near-field provides the opportunity to excite only molecules within the upper 100 nm of the sample surface, and it offers a resolution beyond the diffraction limit. Moreover, it is possible to study the interaction between tip and molecule. The drawbacks of SNOM are tip-induced effects on the sample, e.g. the lifetime of a fluorophore can be influenced by the tip. For interpretation of the acquired scanning images knowledge about the used tip is required. The limited optical damage threshold of a tip limits

the achievable excitation power and therefore the speed of a measurement. Another problem is the optical background caused by the tip itself.

Because SCOM is a far-field technique, it enables to investigate molecules deep inside a transparent bulk sample. No external influences beside optical induced effects are introduced by the instrument. The opportunity to work at high signal to background ratio allows for a fast and precise determination of the molecular fluorescence properties. It is possible to utilize SCOM for reliable determination of the three-dimensional orientation of arbitrarily oriented molecules without loosing any performance of SCOM.

In conclusion SCOM is better suited for efficient optical measurements on single molecules if external influences should be avoided and if the concentration of the fluorophores can easily be tuned. For this reason all single-molecule experiments presented in the forthcoming chapters are performed by utilizing the SCOM part of the instrument.
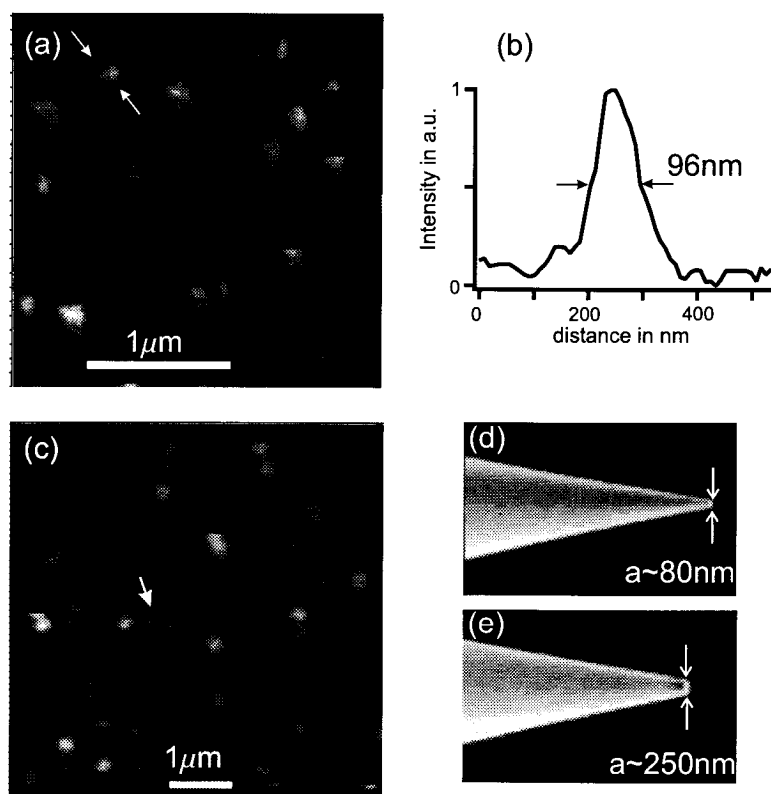
Figure 3.14: Imaging of single fluorescent molecules by SNOM. Single DiI molecules embedded in a 20nm thick polymer film were imaged (a) using a tube-etched, aluminum coated near-field tip with no further treatment like the tip shown in the SEM micro-graph (d). In (b) the intensity profile of the marked molecule in (a) is displayed. The single-molecule image in (c) was obtained with the tube-etched and FIB-treated tip, which is shown in (e). The marked double-lobe pattern in (c) can be assigned to a molecule almost oriented along the optical axis (see matrix in figure 3.4).

Figure 3.15: A combined optical (a) and topographical (b) SNOM image of a micro-contact printed pattern of TRITC labeled chicken IgG molecules is shown. In (c) and (d) line-profiles taken at the marked positions 1 and 2, respectively, are shown, where the black lines are intensity profiles and the gray lines are height profiles.
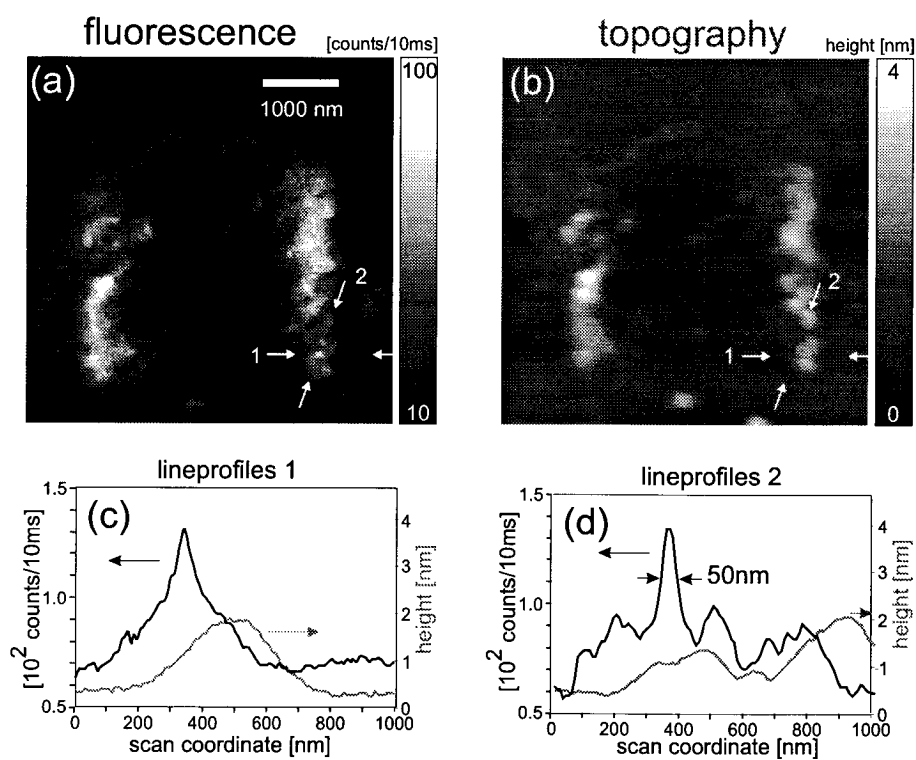
4. Photostability of terrylene in a para-terphenyl crystal

Using scanning confocal optical microscopy the properties of individual terrylene molecules embedded in a p-terphenyl crystal were investigated. The most prominent result is the great photo-stability of this system with a corresponding ensemble-averaged photo-destruction quantum efficiency lower than $1.2 \cdot 10^{-8}$. On average, with a detection efficiency of 6.5 %, a stable fluorescence signal of 10^5 photons/s could be detected from single molecules during one minute of continuous photo-excitation. Both irreversible and reversible abrupt fluorescence intensity jumps to the background have been observed. The experimental data indicate that diffusing quenchers at low concentration in the crystal contribute to fluorescence bleaching of single molecules. The large photo-stability allows for long illumination times and high emission rates of single molecules trapped in a crystal at room temperature.

This chapter is based on [31].

4.1   Introduction

Optical studies of individual fluorophores can be utilized to probe various environmental conditions at a microscopic scale (see chapters 1 and 2). A molecule emits light for a time which is limited by photo-bleaching provided that its residence time in the excitation focus is long enough. Photo-bleaching therefore imposes an upper limit for the detectable number of photons from a single molecule at room temperature. The photo-destruction quantum efficiency has been reported to range approximately from 10^{-7} to 10^{-5} in various systems [4, 26, 103, 130]. For experiments and applications at room temperature, it is of great importance to optimize the photo-stability by choosing appropriate experimental conditions. A large photo-stability allows to maximize the signal to noise ratio for a given experiment since a single molecule can be studied at a high emission rate for a long period. In such a case, fascinating experiments, e.g. time-resolved spectroscopy and quantum optics experiments of single molecules in cavities, are greatly facilitated. In addition, near-field optical devices using single organic molecules as nanometric light sources can be envisaged [74]. In this chapter the photo-stability of single terrylene molecules in a p-terphenyl crystal is studied. On average $5.7 \cdot 10^6$ fluorescence photons were detected from individual molecules before photo-bleaching took place. This number of photons exceeds all previously reported values for all known systems by more than one order of magnitude. Exploiting the high photostability enables e.g. to observe non-classical photon statistic at room temperature, which was demonstrated for the first time in our group by utilizing this system [32], based on the study presented here.

4.2   Methods and materials

Crystal flakes of p-terphenyl doped with terrylene are prepared by co-sublimation of p-terphenyl and terrylene [101]. An approximately 10 μm thick crystal flake is chosen as sample. From fluorescence confocal images a terrylene concentration of $1.5 \cdot 10^{-10}$ mol/l is estimated. Previous low temperature studies indicate that terrylene in the p-terphenyl crystal absorbs around 579 nm, having a fluorescence quantum yield

close to unity [60]. The flake is attached to a cover glass with a tiny amount of index matching oil. Images of single molecules are recorded with the confocal part of the setup, shown in figure 3.5, p. 39. The light source is an argon ion laser operated at 514 nm. The fluorescence is detected by an avalanche photodiode after passing the dichroic mirror. The residual scattering light is blocked by a 514 nm super notch filter and long pass color filters.

4.3 Results and discussion

Figure 4.1 shows a confocal fluorescence image of single terrylene molecules embedded in a p-terphenyl crystal. The peak count rates at an excitation intensity of 900 kW/cm^2 range from $1.6 \cdot 10^5$ to $6.9 \cdot 10^5$ counts/s with a mean value of $4.2 \cdot 10^5$ counts/s. With a pixel integration time of one millisecond, the signal to noise ratio is about 400 and the total time needed to record an image (256 pixels x 256 pixels) is $\sim$ 65 seconds. The signal to background ratio ranges from 3 to 12 for the most intensive peaks. At an integration time of 1 ms/pixel, several consecutive images of the same area are fully reproducible with all molecules showing up at the same positions in the images. Even if the integration time is increased to 20 ms/pixel, only a few percent of the molecules are missing in the second of two consecutive images. Structures, characteristic for fast photo-bleaching such as stripes of a few pixels in length or half-moon shaped dots (see e.g. figure 5.2, p. 76, or figure 6.6, p.100) are hardly ever found.

These observations already reveal the high photo-stability of individual terrylene molecules in a p-terphenyl crystal at room temperature. This feature has been studied in detail by investigating the photo-stability of 41 single molecules at an excitation flux of 225 kW/cm^2 and a pixel integration time of 22 ms. In figure 4.2, traces of repetitive line scans are shown for three molecules. In this kind of measurement, the same line is scanned successively over and over again. Molecule A shows a stable fluorescence signal with a count rate of approximately $5 \cdot 10^4$ counts/s during 256 line scans (trace a). For molecule B (trace b) the fluorescence intensity jumps irreversibly to the background count rate at t $\cong$ 9 min. In contrast, molecule C (trace

c) shows a reversible behavior. After an intensity drop at t $\cong$ 18 min, the fluorescence recovers and fluctuates before it again drops irreversibly to the background. Similar fluctuations were observed for 15 out of 41 molecules in this experiment. Since the absorption spectra are relatively broad at room temperature, these fluctuations cannot be explained by spectral jumps out of the resonance with the exciting laser frequency as previously observed for single molecules at liquid helium temperature [1]. Indeed, the largest spectral shifts, expected to be limited by the width of the inhomogeneous band of a few cm^{-1} typical for doped organic crystals, would be unobservable in this experiment because of the low spectral resolution (> 30 cm^{-1}). Furthermore, rotational jumps of the molecules (see e.g. [42]), such that the dipole moment becomes accidentally oriented perpendicular to the light polarization, can be ruled out. From the crystal structure of the closest shell surrounding the substitutional terrylene molecule, the molecular orientation can be thought of being tightly fixed. However, strong changes either in the absorption cross section σ and/or in the fluorescence quantum yield ϕ_f may lead to the observed fluctuations [66]. A mechanism that could explain the variations of the parameters σ and ϕ_f, namely fluorescence quenching by diffusing species, is discussed below.

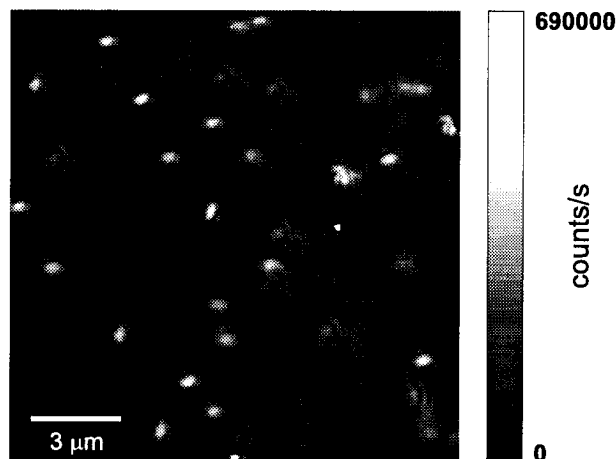Figure 4.1: Fluorescence image (256 x 256 pixels) of a $15.2\,\mu m \times 15.2\,\mu m$ sample depth section. Count rates are represented by a gray scale. Each molecule corresponds to a bright spot. The pixel integration time is 1 ms and the excitation flux is $900\,kW/cm^2$. The average number of photons recorded per molecule is $15 \cdot 10^3$ for a total illumination time of approximately 35 ms.
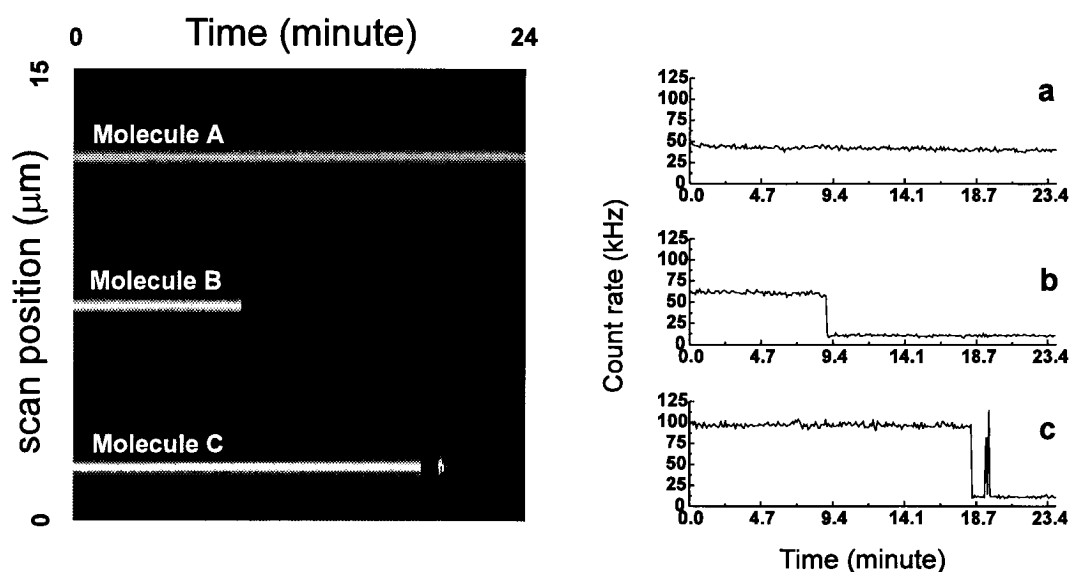
Figure 4.2: Left: line scan of $15\,\mu m$ length along the x-direction at a constant y-position as a function of time. The three detected molecules illustrate three characteristic behaviors. Right: fluorescence time traces obtained from a one pixel wide cut along the maximum of the fluorescence traces on the left.

The photo-stability is quantitavively deduced from the line scans by determining the number N of detected photons emitted by each molecule which photobleached within the 256 line scans. The quantum efficiency for photo-destruction ϕ_b is calculated from N according to $\phi_b = (\eta\phi_f)/N$ where η is the detection efficiency and ϕ_f denotes the fluorescence quantum yield. The unknown quantity ϕ_f is set to 1. Therefore, the estimated values of ϕ_b represent upper limits, which implies that the deduced photostabilities might be underestimated. The histogram shown in figure 4.3 (a) is obtained from 32 out of 41 molecules that photobleached during the 24 minutes total duration of the experiment. The histogram is truncated on the left side at $\phi_{bt} \cong 2.6 \cdot 10^{-6}$ corresponding to the smallest measured value of ϕ_b or the most photostable observed terrylene molecules, respectively. Fast photobleaching events occurring on a time scale shorter than $\cong 20$ ms of photo-excitation are rarely observed and are not included in the statistics. No decrease in photo-stability is observed when the excitation flux is increased by a factor of 2. Consequently, the chemical stability depends, if at all, only weakly on the local heating generated through non-radiative transitions of the excited molecule. The results of the line-scan experiment with doubled intensity are shown in figure 4.3 (b). At this intensity,

photobleaching was observed for all except one of the 18 investigated molecules. Now 37 % of the molecules showed a photo-destruction quantum efficiency even smaller than the cutoff ϕ_{bt} determined previously at half of the excitation intensity. Within the errors the two histograms in figure 4.3 are the same.
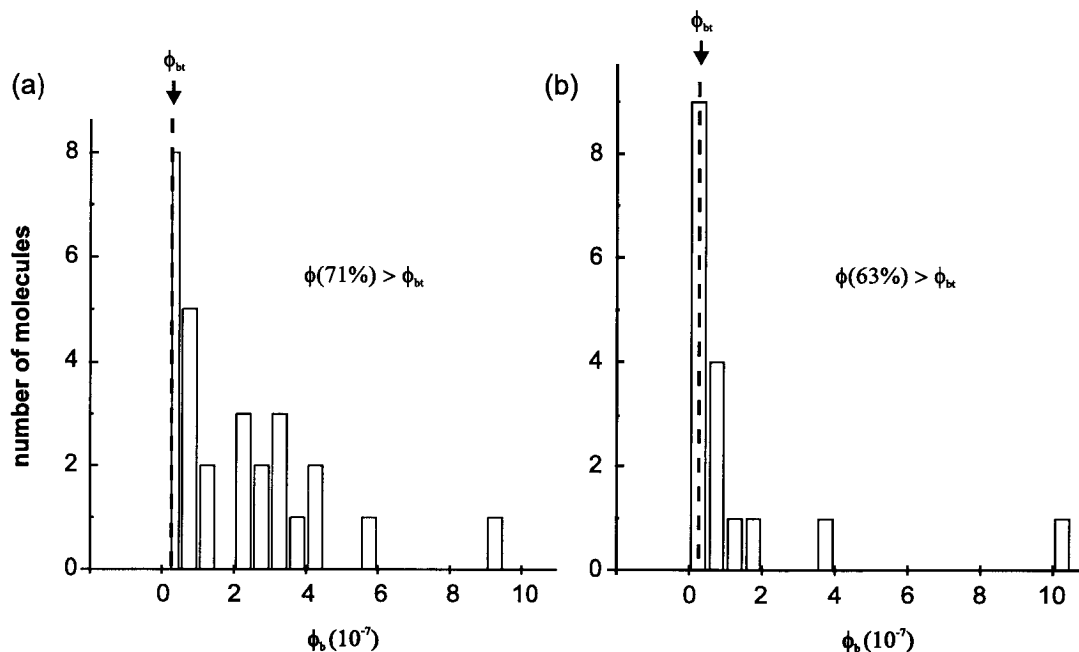

Figure 4.3: Histograms of the photo-destruction quantum efficiency ϕ_b measured for photobleached molecules in the line scan experiment (22 ms/pixel). a) $I = 225\,\mathrm{kW/cm^2}$, b) $I = 450\,\mathrm{kW/cm^2}$.

In order to elucidate a possible illumination-time dependence of the photobleaching, in the next experiment, molecules are placed in the excitation focus and continuously illuminated without scanning. The signal is sent to a multi-channel analyzer (Stanford Research 430) with a 10 ms bin width. Fluorescence intensity traces (d-f') are presented in figure 4.4 for three different molecules (D, E, F). Molecule D shows a stable count rate of $3.35 \cdot 10^5$ counts/s until photobleaching occurs after 18 seconds of photo-excitation (trace d). Trace e indicates an initially stable count rate for molecule E which suddenly startes to fluctuate at t_1 until bleaching occurs at t_2 (see inset in figure 4.4). Similar fluctuations are observed for 15 out of 41 molecules in the line scan experiment but only for 2 out of 30 molecules in the continuous excitation experiment. Typical examples of fluctuations are shown in the traces of

molecule C in figure 4.2 and in the traces of molecules E and F in figure 4.4. The fluctuations are characterized by a remarkable behavior. The drops in intensity end at the background and the returns do not lead to the initial values in most cases. Smaller and larger count rates are recorded during the fluctuations if compared with the fluorescence intensity of the stationary periods. This effect is observed for all the molecules that undergo fluctuations. The fluorescence of molecule F ceases at t_3, recovers at t_4 for a short period until bleaching occurs at t_5 (trace f) and finally recoveres again in a new acquisition (trace f') started a few seconds after the end of the measurement of trace f. Four consecutive traces are recorded for molecule F which shows an exceptionally high photo-stability $\phi_b < 5 \cdot 10^{-10}$. In these traces, the count rate decreases very slowly (probably due to mechanical drifts of the setup) from $3 \cdot 10^5$ to $2 \cdot 10^5$ counts/s during 11.5 minutes of photo-excitation.
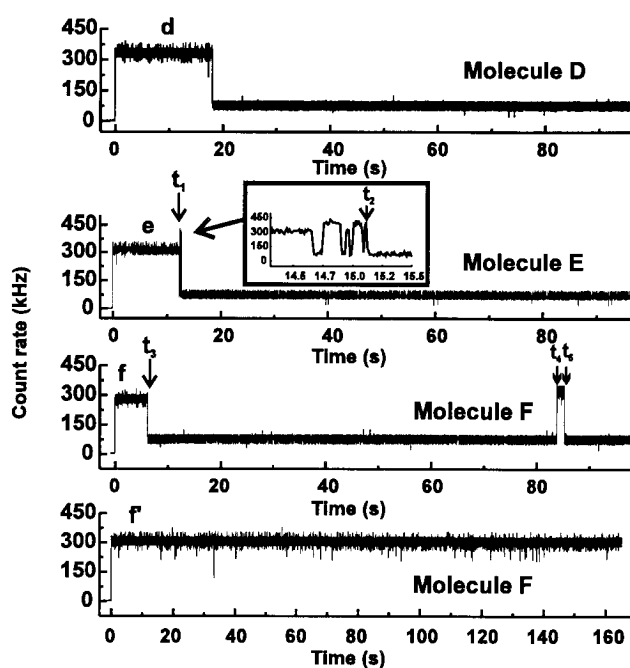
Figure 4.4: Fluorescence time traces for 3 different molecules excited continuously. A fluorescence on-off blinking is observed on a millisecond time scale for molecule E before photobleaching takes place at t_2.

Under continuous photo-excitation, 28 out of 30 molecules photobleach during the trace acquisition time of 128 s. The ϕ_b measured at an excitation intensity of 225 kW/cm^2 range from $4.3 \cdot 10^{-9}$ to $1.3 \cdot 10^{-7}$. The corresponding ensemble-averaged

photo-destruction quantum efficiency is estimated to be lower than $\eta\phi_f/\bar{N} = 1.2 \cdot 10^{-8}$ where $\bar{N} = 5.7 \cdot 10^6$ is the average of N over the 28 photobleached molecules. The data are presented as a histogram in figure 4.5.
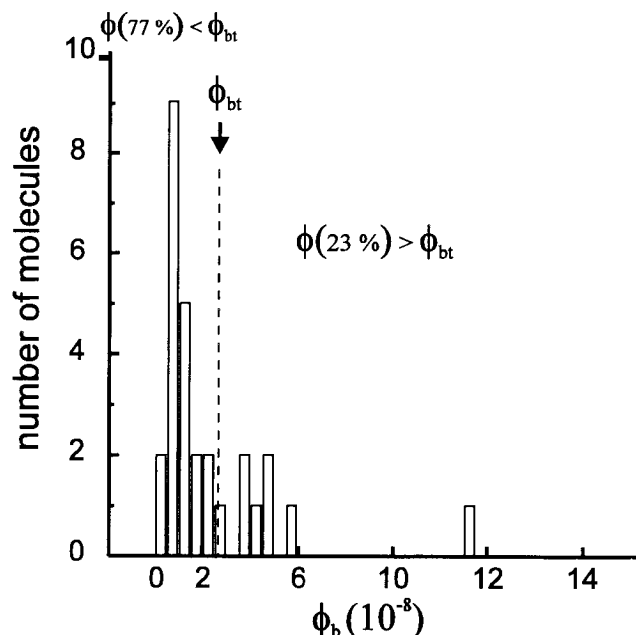
Figure 4.5: Histogram of the photo-destruction quantum efficiency ϕ_b measured for photobleached individual molecules under continuous excitation ($I = 225\,\mathrm{kW/cm^2}$).

Under continuous excitation, 77 % of the investigated molecules showed a photo-destruction quantum efficiency ϕ_b smaller than the cutoff $\phi_{bt} \cong 2.6 \cdot 10^{-8}$ defined above for the line scan experiment. Consequently, the photo-stability appears to be larger under continuous excitation.

The larger photo-stability under continous excitation with the same excitation power as used in the line-scan experiment allows for the conclusion that photo-bleaching can not be explained by a purely photo-induced process. A possible explanation for this observation which can also explain the fluorescence intensity fluctuations mentioned above, can be given by assuming slowly diffusing quencher species in the sample. Photo-destruction due to contact with a quencher is considered as a reaction between quencher and excited terrylene molecule resulting in a complex, which is non-fluorescent when excited at 514 nm. A reaction between an

excited terrylene and a diffusing oxygene can e.g. result in an exo-peroxide, which is stable and non-fluorescent at 514 nm excitation, or in an endo-peroxide, which is also non-fluorescent but non-stable [8]. Because the quenchers diffuse presumably by hopping interstially from one to another lattice site, they may take well defined positions relative to the terrylene molecules. The random hopping of the quencher among these positions may thus lead to the characteristic fluctuations shown in figure 4.4. The enhancements of the fluorescence can be caused by a shortening of the triplet life-time through quenching of the triplet excitation [37]. Another explantion can be given by assuming that the result of the reaction between quencher and previously formed terrylene-quencher complex resulting in a fluorescent product. The fluorescence rate of the formed fluorophore would depend on its absorption and emission spectrum as well as on the magnitude and direction of its transition dipole, which would also explain the oberservation that during the fluctuations the fluorescence intensity in on-times can be increased or decreased compared to the initial fluorescent rate. Diepoxide is a possible fluorophore, because it can result from a decay of the non-stable endo-peroxide [8]. According to the presented model, the encounter of the excited terrylene with a quencher can result (a) in a non-stable and non-fluorescent product, which results in dark periods, (b) in fluorescence fluctuations due to fluctuating singlet/triplet quenching efficiency, (c) in a non-stable and fluorescent product, which gives rise to on-times with various fluorescent rates, and (d) in a stable non-fluorescent product, which can be regarded as final photobleaching event.

The model of slow diffusing quencher molecules, which interact with the excited terrylene molecule, results in one of the four above mentioned outcomes. To a certain extent this explains also the higher photo-stability at continous excitation compared to the line-scan measurement: The probability that the quencher arrives at the position of the observed terrylene at a certain time after the start of the experiment is equal for both types of measurements. But in the line-scan experiment the experiment time is about forty times longer then the excitation time. Consequently, with respect to the excitation time the observed terrylene molecule in a line-scan experiment will be encountered more often by a quencher then a terrylene molecule under continous excitation leading to a decreased photostability in line-scan exper-

iments. However, while the molecules bleach on average after 4 min experiment time in the line-scan experiment, bleaching under continous excitation requires on average a time of only 1 min. This supports a model which encloses two different beaching processes: bleaching caused by diffusing quenchers, and photo-induced bleaching. The photo-induced bleaching is more important in the experiment with continous excitation, while the line-scan experiment favours the observation of the slow diffusion-controlled formation of quencher-molecule complexes. This explains also why a larger fraction of molecules exhibit fluorescence fluctuations during scanning ($\sim 37\%$) than upon continous excitation ($\sim 8\%$).

4.4   Conclusions

The detection of single organic molecules in a molecular crystal at room temperature has been demonstrated. Terrylene molecules rigidly immobilized in a p-terphenyl crystal show the largest photo-stability ever observed in a single molecule experiment at room temperature. The largest photo-stability was found for continuous excitation. The reduced photo-stability in the line-scan experiment has been attributed to diffusion-controlled formation of molecule-quencher complexes leading to no detectable fluorescence upon excitation. The fluorescence fluctuations observed after long stationary periods of stable emission have been assigned to the arrival of a quencher and subsequent quencher hopping in the vicinity of the terrylene molecule or to the formation of an astable fluorophore.

5. Rapid and efficient single-molecule identification

A method for rapid and reliable identification of single molecules is presented. This method relies on determining different properties of each successively detected photon. Knowledge about the behavior of the different species of molecules with respect to the observed properties are gained in bulk experiments under the same condition which are valid for the single-molecule experiment. This knowledge is represented by so called look-up tables, which are used to determine photon by photon the probability for having a molecule of a certain species as emission source. By combining the probabilities of successively detected photons the identification procedure is completed if the resulting probability reaches a certain accuracy. Using this method, single-molecule identification of four different dyes with spectrally and time-resolved photon-counting is demonstrated for the first time. Monte-Carlo simulations show that less than 500 photons are needed to assign an observed single molecule to one out of four species with a confidence level higher than 99.9%.

5.1 Introduction

The possibility to detect fluorescence from single molecules at ambient temperatures has initiated several attempts to identify and distinguish individual molecules in solution [22, 35, 58, 79, 108, 121, 133, 134]. One of the most prominent future applications of such a technique is DNA sequencing by labeling individual bases with different fluorescent dyes [28]. Different properties of fluorescence photons, namely their spectrum resolved in two channels [108], fluorescence lifetime [133], and fluorescence lifetime in conjunction with fluorescence intensity [121], have been analyzed to identify individual molecules. In conventional single-molecule identification techniques, the identification parameters, like fluorescence lifetime [133] and photon burst size [121], are computed from bunches of photons generated e.g. during the passage of the molecule through a focus before photo-bleaching occurs. In the case of fluorescence lifetime, these parameters are obtained by fits of a model function (exponential decay) to a photon arrival time histogram obtained from a single molecule. The criterion of the identification is based on the agreement of the single molecule fluorescence lifetime with the bulk lifetime within a given confidence interval.

Many applications require ambient conditions which lead to a reduced photo-stability of fluorophores compared to fluorophores in a protecting environment like a crystal (see chapter 4). A typical label as used in biology under ambient conditions emits about 10^5 photons before photo-bleaching. Taking into account that the mentioned number is only the mean-value of a corresponding exponential distribution, and that a typical detection efficiency of a sensitive microscope is in the range of 3–8%, this implies the need for an efficient identification method if the aim is to identify almost all labels with high accuracy. The number of required photons necessary to achieve a certain accuracy can be reduced if more observables are determined, in which the molecular species differ, and if a more precise knowledge about the properties of the species with respect to these observables are available. In the presented method the knowledge about the observables of the different species are not based on theoretical models, but on empirical fingerprints obtained by bulk-measurement, which were performed for each molecular species under the same experimental conditions as valid in the single-molecule experiment. The probability for having one

particular of the species as emission source can be determined for each detected photon by using these fingerprints. By combining the probabilities of successively detected photons the identification procedure is completed, if the resulting probability reaches the acquired accuracy. The outlined methology can be applied to each set of simultaneously determined observables.

The presented measurements rely on analyzing each successively detected photon with respect to the observables 'singlet lifetime' and 'emission spectrum'. This type of time-resolved photon-by-photon analysis became possible by recent developments in time-correlated counting electronics and multichannel detection [11]. An important benefit of the method is that the calculations involved are simple and can be performed online. Therefore the molecules can be sorted and collected simultaneously for further use or verification of the identification. Second, the analysis can be stopped when the required accuracy is reached, which allows for a further optimization of the identification procedure. Third, no model is required for the analysis.

5.2 Methods and materials

Theoretical part

The first step in the presented method is to provide the empirical fingerprints, which describe the different species with respect to the observables determined from each photon. This is done by measuring distributions of these observables in bulk-samples which contain only fluorophores of one species, respectively. The values of an observable are partitioned in K bins. Each bin b contains $c_i(b)$ counts, which is the number of detected photons showing a corresponding value of the observable within this bin. The normalized photon histogram from molecules of sort m_i ($1 \leq i \leq N$), where N is the number of different species, provides the relative occurrence of photons in the respective bin. This relative occurrence is equal to the probability of detecting a photon in bin b ($0 \leq b \leq K$) of this observable given that molecule

belongs to the sort m_i

$$P(b|m_i) = \frac{c_i(b)}{\sum\limits_{\tilde{b}=0}^{K} c_i(\tilde{b})} . \tag{5.1}$$

Assuming that the number of counts not originating from the molecule is negligible compared to the number of photons emitted by the molecule, the probability for having a molecule of sort m_i as emission source of a count in bin b is

$$P(m_i|b) = \frac{P(m_i)P(b|m_i)}{\sum\limits_{q=1}^{N} P(m_q)P(b|m_q)}, \tag{5.2}$$

provided that the molecule is one out of the N possible kinds of molecules. If the occurrences of the different molecules in the sample are almost equal, as would be the case in DNA sequencing, equation 5.2 simplifies to

$$P(m_i|b) = \frac{P(b|m_i)}{\sum\limits_{q=1}^{N} P(b|m_q)}. \tag{5.3}$$

A look-up table is generated with the aid of equation 5.3 which assigns to each bin b of each observable a certain probability $P(m_i|b)$ for each species i. This look-up table is multi-dimensional if more than one observable is measured.

After this preparatory work is done the procedure for the actual single-molecule identification can start. Provided that only one individual fluorophore is within the observation volume, photons from this single molecule are successively detected and analyzed with respect to each utilized observable. According to the determined values of an observable the probabilities $P(m_i|b)$ can be read from the look-up table. If several observables of a fluorescence photon are taken into account, their respective probabilities in equations 5.2 or 5.3 have to be multiplied. This holds of course only provided that the observables are statistically independent.

The current probability for having either of the species as the emission source has to be updated after each detected photon. If L photons are detected from one molecule in the respective bins b_j, where the index j denotes the photon number,

the probability that these photons are emitted by the molecule m_i can be calculated according to

$$P_L(m_i) = \frac{\prod_{j=1}^{L} P(m_i|b_j)}{\sum_{q=1}^{N} \prod_{j=1}^{L} P(m_q|b_j)}. \tag{5.4}$$

Identification of a molecule is achieved, if the determined probability for one of the species reaches the required accuracy which is in our case 99.9%. In this case the measurement can be stopped.

Experimental part

The confocal part of the setup shown in figure 3.5, p. 39 is utilized to perform the experiment. An active mode-locked Nd:YAG laser frequency-doubled to 532 nm is used to excite the molecules. The width of the pulses is approximately 150 ps with a repetition rate of 76 MHz. The arrival time after pulsed excitation and emission wavelength of the fluorescence photons are observed as described below.

The four dyes rhodamine 6G (R6G), sulforhodamine B (SRB), dibenzanthranthene (DBATT), and 1,1'-dioctadecyl-3,3,3',3'-tetramethylindocarbocyanine perchlorate (DiI) are chosen as species to be identified, because of their distinct emission properties and fluorescence lifetimes (see table 5.1).

Single-molecule samples are prepared by spin-casting (9600 rpm) of a 10 μl droplet from a solution of polymethylmetacrylate (PMMA) in toluene containing the dye in a concentration of 10^{-9} M onto standard glass cover slips, previously cleaned by baking at 510°C for six hours. The resulting polymer films are investigated by atomic force microscopy revealing a smooth surface and a thickness of about 30 nm. Bulk samples are prepared in the same way as the single-molecule samples but with micro-molar dye concentrations.

Raster scanning of a single-molecule sample leads to a fluorescence burst each time a molecule passes the confocal area, which has a volume of approximately 100 attoliters. The scattered laser-light and background are efficiently suppressed by a

dichroic mirror, and a holographic notch filter. The resulting fluorescence light is spectrally separated by a additional dichroic mirror (50% transmission at 575 nm) before being detected by two APDs. Both APD signals are fed through a routing device into a PC-card based single-photon counting device (SPC 402, Becker&Hickl, Germany). A trigger from the mode-locker driver serves as the synchronization signal. Having dead times of 100 ns and 150 ns, respectively, the APDs and the SPC card are capable of detecting photons with a rate of up to 8 Mhz. Considering an overall detection efficiency of the setup of $\eta \simeq 0.065$ this number perfectly matches the excitation repetition rate. For each photon, the arrival times τ with respect to the excitation pulse (256 channels, 25 ns width), the time t with respect to the start of the experiment (50 ns resolution), and the information which detector counted the photon is stored. The timing resolution is approximately 400 ps FWHM.

For determining the empirical fingerprints of the four species the respective bulk samples are investigated in the same manner.

5.3   Results and discussion

Single-molecule identification experiments

Graphical representations of the look-up tables constructed according to equation 5.3 from the bulk measurements are shown in figure 5.1 together with the measured photon arrival time histograms (a). The stacked probabilities (according to equation 5.3) to have a given molecule as the source of a photon is plotted versus the photon arrival time for both spectral channels (b). Due to the pulse repetition rate of 13 ns, almost two complete fluorescence decays occur within the range of 25 ns of the time-to-amplitude converter (TAC). Therefore, for each of them a separate time window is set. The borders of the time window are adjusted to exclude scattered laser light which still might pass the notch and band pass filters. Light which is scattered by the solvent or the matrix surrounding the molecule can obscure the identification. Nevertheless, in order to optimize the number of analyzed photons the time windows are kept as large as possible. The photons close to the boundaries

of the TAC range are neglected since the TAC has non-linearities at both limits of its range. The shape and the size of the areas representing the probabilities deter-
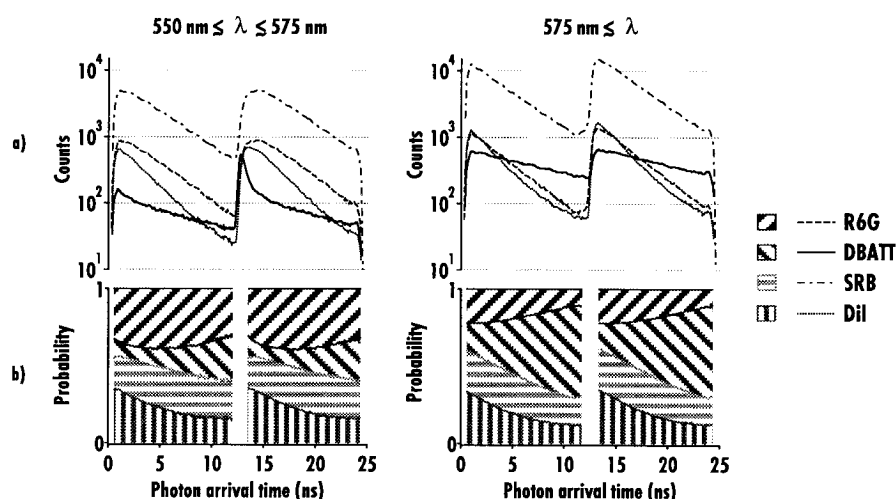

Figure 5.1: a) Photon arrival time histograms in the two spectrally distinguished channels obtained from bulk measurements of the four dyes R6G, SrB, DBATT, and DiI. b) Graphical representation of the look-up tables computed from the histograms a) according to equation 5.3 in two time windows within the TAC range.

mine the efficiency of the identification procedure. Two remarkable features can be observed in the photon arrival time histograms. A peak at time 13 ns, the time position of the laser pulse, in the histogram of the dye DBATT in the short wavelength channel shows that scattered laser light still is detected. The peak is visible only for DBATT since its fluorescence intensity in the short wavelength channel is much lower as compared to the other dyes. Second, there is a significant difference in the shape of the histograms at short times between the two channels. This difference is due to rotation of the molecules within the polymer matrix which leads to a polarization relaxation of the emission. The dichroic mirror has a polarization dependent reflectance which makes this relaxation visible in the arrival time histogram [95].

In the single-molecule identification experiment the respective look-up table is consulted for each count depending on which detector registered the photon. The obtained probabilities lead together with equation 5.4 to the joint probabilities of observing either one of the molecules.

A typical image of a sample of SRB in a PMMA film obtained by scanning confocal optical microscopy is shown in figure 5.2. The count rate as a function of time along the white line is plotted in the inset. The transit of the molecule through the confocal spot is seen as a burst of photons having a duration of about 15 milliseconds. Depending on the type of dye, during the transit time approximately 500 to 3000 photons are detected in a burst. The number of dark counts during the dwell time is at least two orders of magnitude lower and therefore neglected in the analysis.
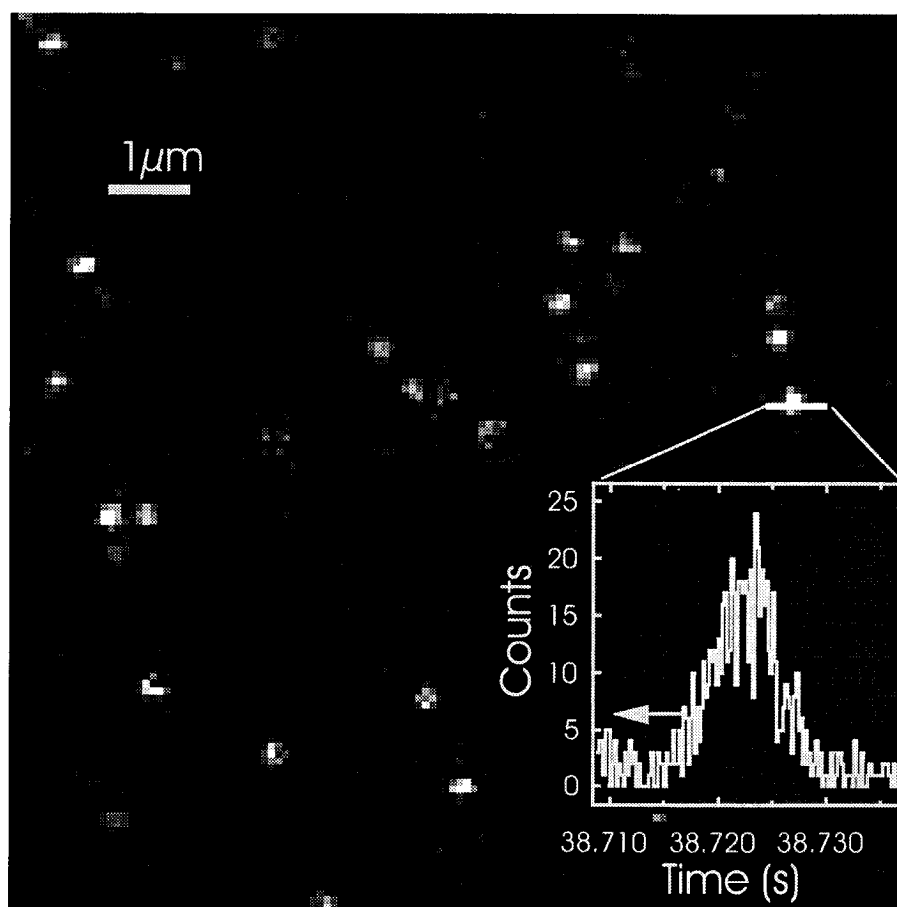
Figure 5.2: Scanning confocal optical microscopy image of individual SRB molecules in a PMMA film. Inset: Histogram (bin width 0.2 ms) of the photon burst emitted by the highlighted molecule during a single transit through the confocal volume.

Figure 5.3 visualizes the identification experiment for four different single molecules, one of each dye, embedded in a PMMA film. From top to bottom pure dilute samples of R6G, DBATT, SRB, and DiI, respectively, are investigated in this

Figure 5.3: Analysis of single-molecule identification experiments for four molecules of the respective dyes: stacked probabilities to have either dye versus photon number, a) without spectral resolution), b) spectrally resolved in two channels.

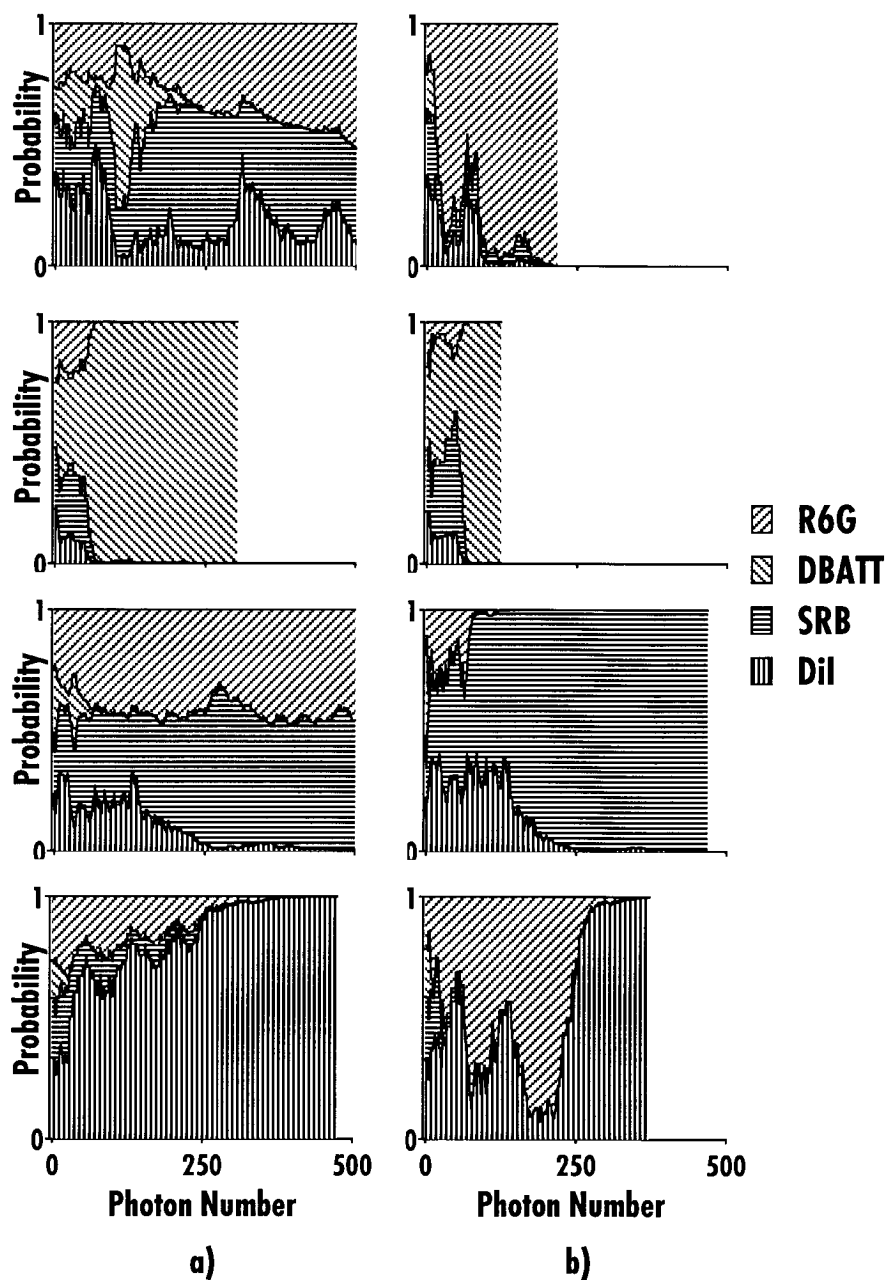experiment. The stacked probabilities according to equation 5.4 are plotted versus the photon number for four selected molecules. Each panel shows how the probability of any one of the molecules being observed develops with the photon number. As soon as the confidence level of 99.9% is reached the analysis is stopped. For the sake of comparability with the MC simulation (see below), the fluorescence photons of each burst are analyzed without (a) and with (b) taking spectral resolution into account. In the case of spectrally resolved time-correlated single-photon counting (b) the four molecules are identified with a small number of photons. In contrast, if spectral resolution is discarded (a), no decision can be made regarding the dyes R6G and SRB within the transit time of the molecule in this example. Figure 5.3 demonstrates the stochastic nature of the identification experiment. For small numbers of photons the probabilities show large fluctuations which decrease as the number of detected photons increases.

Due to the polarization dependence of the dichroic mirror reflectance the count ratio between both spectral channels depends on the orientation of the single molecule. Within the PMMA film, the molecules obey a fixed orientation. For this reason, linearly polarized light was used in order to excite mainly molecules with the proper orientation. Moreover, near the polymer/air interface the lifetime of a fluorophore depends on its orientation [71] (the lifetime differs up to a factor of three for the same molecule once oriented perpendicular and once parallel with respect to the interface). However, in the presented experiment perpendicular oriented molecules rarely are observed, because they are excited ten times weaker compared to in-plane molecules (see table 6.1, p. 95). A molecule in a liquid which rotates quickly compared to the transit time through the confocal volume takes an isotropic effective orientation removing the polarization dependence of the count ratio.

Monte Carlo simulations

Random photon arrival times are generated with the aid of a Monte Carlo (MC) method obeying exponential probability distributions according to one of the four molecules at a time. Gaussian time jitter is added to account for a finite instrument response function. To simulate the experiment with two spectrally resolved channels

these are randomized obeying the count ratio between both channels. The simulated data are then analyzed according to the procedure outlined above.

For the simulation, which were performed by colleagues [94], the look-up tables are generated assuming single-exponential fluorescence decay behavior. A single look-up table suffices for the simulation of the experiment without spectral resolution, whereas two look-up tables, one for each spectral channel, are computed for the simulation of the spectrally resolved experiment. The lookup tables are generated within a finite time window since in the experiment a time window has to be set to account for the laser repetition rate and to reject photons not emitted by the molecule. In order to compare the simulation with the experiment the bulk values obtained from the reference experiments were used for the fluorescence lifetimes as well as for the count ratio between the two spectral channels (see table 5.1).

Table 5.1: Results of the MC simulations of single-molecule identification with sequential statistics. Right column: Average number of photons required for identification with 99.9% accuracy. Left column: Bulk emission maximum and fluorescence lifetime .

Dye	Emission maximum (nm)	Fluorescence lifetime (ns)	No. of photons	
			1 channel	2 channels
DBATT	586	10.15	285	102
SRB	584	4.15	7562	647
R6G	555	3.75	8070	267
DiI	572	3.05	1638	724

Table 5.1 summarizes the results of the MC simulations. It compares the number of photons needed to achieve a confidence level of 99.9% for four different dyes for detection with and without spectral resolution. It clearly shows that the dyes SRB and R6G can be identified with a small number of photons only if spectral resolution is exploited. The dye DBATT, which has a significantly longer fluorescence

lifetime than the other dyes, is identified by a small number of photons without needing spectral resolution. The most dramatic decrease of the number of photons required for identification when spectral resolution is exploited is observed for R6G since its spectral mean is significantly lower than that of the other dyes, whereas its lifetime is close to that of SRB.

Recently, the number of photons required to identify one molecule out of two by fluorescence lifetime without spectral information with 99.9% accuracy was theoretically predicted to be well above 1000 if their lifetimes are 3 and 4 ns, respectively [97]. The prediction was based on the precision of the determination of fluorescence lifetime, *i.e.* based on a model function. Here, *e.g.* DiI and SRB having fluorescence lifetimes of 3.05 and 4.15, respectively, are both distinguished within a set of four dyes with about 700 photons. Compared to the theoretical prediction in Ref. 11 the here presented approach is more realistic since a finite instrument response function is taken into account. In addition, in order to match the experimental conditions only photons detected within a 12 ns time window are used for the analysis yet photons outside this window still contribute to the total number of photons needed.

5.4   Conclusions

It has been shown that spectrally resolved time-correlated single-photon counting is suitable to identify single molecules which are similar in fluorescence lifetime, but different in emission spectra, and vice versa. With the presented method of analysis the information associated with each photon can be transparently exploited for the identification of its emitter. Compared to other single-molecule identification methods, the approach presented here has three advantages. (1) The photo-destruction quantum yield and out of focus molecules which both may obscure the results obtained if the fluorescence burst size is evaluated [121] have no influence on fluorescence lifetime and spectrum. (2) No theoretical models are required since our analysis is based on probability distributions. (3) There is no need for a deconvolution since all instrument response functions are already included in the empirical look-up tables.

The method can be easily extended to more observables and higher spectral resolutions. Increasing the spectral resolution to 256 channels is well conceivable and MC simulations show that this will lead to a further decrease in the number of required photons by almost an order of magnitude. An improved set of dyes with more distinct properties can gain efficiency of identification to an even higher level. If the molecules are distinct with respect to another observable, resolution of this observable has to be provided and one more histogram needs to be recorded which is then used for the analysis in the same way. For example, to utilize rotational mobility a polarizing beam splitter has to be inserted in one of the two detection paths with an additional APD. Thus, if only a small number of photons emerging from one single molecule can be detected, the single-molecule misclassification probability can be decreased to the level which is necessary for reliable DNA sequencing. The method offers the chance to simplify and miniaturize the components to produce an inexpensive, easy to use, yet extremely sensitive screening device for clinical applications.

Seite Leer /
Blank leaf

6. Mapping confined fields with single-molecules and *vice versa*

Single dye molecules are used as local probes to map the spatial distribution of the squared electric field components in confined optical fields. Simulated field distributions are quantitatively verified by experimentally obtained field maps. Using these maps it is shown that the field distribution in the focus of a high numerical aperture lens can be engineered such that electric field components in all directions acquire comparable magnitudes. It is demonstrated that a single SCOM image of single molecules recorded with such an engineered focus allows for the determination of the 3D orientation of arbitrarily oriented molecular absorption dipoles.

This chapter is based on [109], and [110].

6.1   Introduction

Single fluorescent molecules are among the smallest possible sensing devices one can think of. Exploiting their sensitivity to changes in the local environment, single dye molecules have been used as sensitive probes for dynamics in solids at low temperature and as markers in biological systems [6,36]. A single dye molecule is also an ideal probe for mapping confined optical fields, because the fluorescence rate of a single molecule is directly proportional to the strength of the squared electric field component parallel to its absorption dipole moment. Scanning a single molecule with high spatial accuracy through a confined field distribution and recording the fluorescence count rate at each point therefore yields an image pattern which is a map of the spatial distribution of the respective squared field component. Single-molecule images showing such effects were first noticed in aperture scanning near-field optical microscopy (SNOM) [16,123]. In these first SNOM images of single molecules it was observed unexpectedly that single molecules do not appear as identical peaks, but rather as various pattern shapes. For an illustration see figure 3.14 (c), p. 57 which shows an image of single molecules taken with a tube-etched and FIB-treated tip. The different patterns are caused by various orientations of the imaged molecules, which were scanned through the inhomogeneous field distribution in the near-field of a sub-wavelength aperture (see figure 3.4, p. 37). A molecule with a certain orientation accordingly maps the distribution of the field-component, which is parallel to the molecular absorption dipole moment. However, the method is not restricted to SNOM: distributions of confined fields for various kinds of scanning optical microscopes can be measured and compared *quantitatively* to simulations. This is a capability that may be of importance for the future development of near-field optics, since it allows for an experimental determinations of field-distributions with nm-resolution.

Vice versa, if the electric field distributions are precisely known a wealth of information can be inferred from microscopy images. It is possible to determine precisely the orientation of molecular absorption dipole moments. This is an important capability, because reorientation of the dipole moment can be caused by subtle changes in the chromophores environment [42] or reveals degrees of freedom in the spatial or-

ganization of moieties within macromolecules by observation of hindered rotational diffusion [44]. Furthermore, various relevant observables in single-molecule experiments such as lifetime [71] and fluorescence quantum yield [89] are influenced by the dipole orientation. Knowledge of relative orientation is also a prerequisite for precise distance measurements using single-pair fluorescence resonant energy transfer [43].

A fundamental requirement for the determination of *arbitrary* molecular dipole orientations is that the three independent components of the optical excitation field are of comparable magnitude. By analyzing single-molecule image patterns it is proved that a field distribution satisfying this condition is created by focusing a doughnut-shaped laser beam onto a dielectric/air interface using a high numerical aperture (NA) lens [109, 110, 129]. These results are of relevance in confocal microscopy of single molecules at interfaces and in tip-enhanced nonlinear optical microscopy [99]. In the latter case, a strong longitudinal field component is necessary to create a strong field enhancement at a sharp metal tip [73, 99].

6.2 Theory for engineering focal fields

The theory for calculating the three-dimensional distribution of electro-magnetic fields in the focus of a high numerical aperture lens was developed by Richards & Wolf (1959) [96] and is still of current interest [5,93,132]. The scalar wave theory and the paraxial approximation is adequate for describing the focusing process with low numerical aperture lenses, but not valid for modeling the focusing process with high numerical aperture lenses. In the following the case of focusing linearly polarized light (x-direction) with a high numerical aperture lens is considered. As opposed to the scalar treatment the vectorial description yields an electric (and magnetic) field in the focal region which also contains components perpendicular to the polarization direction of the incident beam [5, 96].

6.2.1 Pictorial description of the focal field

Figure 6.1 (a) illustrates the geometry of the focusing problem in a ray optics picture. Although ray tracing is inadequate for mathematical modeling of the problem, it can give some insights and rationalizes the general shape and structure of the expected field distributions. The solid lines in figure 6.1 (a) depict representative rays in the outer rim of the incident parallel beam. The incident electric field vector $\vec{E}_i$ is oscillating along the x-direction. The arrows represent the field vector at a certain time at several positions along the beam. After refraction by the lens, all rays, apart from the one on the optical axis, are tilted. Consequently, the orientation of the refracted electric field vector $\vec{E}_r$ in general is tilted away from the pure x-orientation except for some classes of rays which will be discussed below. As a consequence, the field distribution in the focal region contains electric field components of all directions. On the right hand side of figure 6.1 (a) simulated distributions (see section 6.2.3) of the squared x-, y-, and z-component of the electric field in the focal plane are shown. The x-pattern is a bright spot (labeled by $E^2_{\text{foc}\,x}$). The z-pattern consists of two equally intense lobes separated by a dark line along the y-axis ($E^2_{\text{foc}\,z}$). The y-pattern includes four equally intense lobes separated by a dark cross-shaped area oriented along the x- and y-axes ($E^2_{\text{foc}\,y}$). A qualitative explanation for the occurrence of these characteristic patterns is given in the following.

The pattern of the x-component of the electric field is created by superposition of the x-components of the fields in the focused rays. It results in a centro-symmetric pattern with a maximum in the center of the focus because symmetric rays have there the same phase and consequently interfere constructively. Depending on the distance to the geometrical focus in the focal plane, rays have different optical pathways and therefore a non-zero phase difference. This results in less constructive interference and leads to destructive interference, finally resulting in a centrosymmetric fringe pattern.

Rays within the yz-plane ($x = 0$) [see figure 6.1 (b)] are s-polarized, because the electric field vector is perpendicular to the plane spanned by the incident and the refracted ray. The direction of $\vec{E}_i^{(s)}$ remains unchanged after refraction [55]. For this reason rays within the yz-plane only contribute to the x-component of the electric
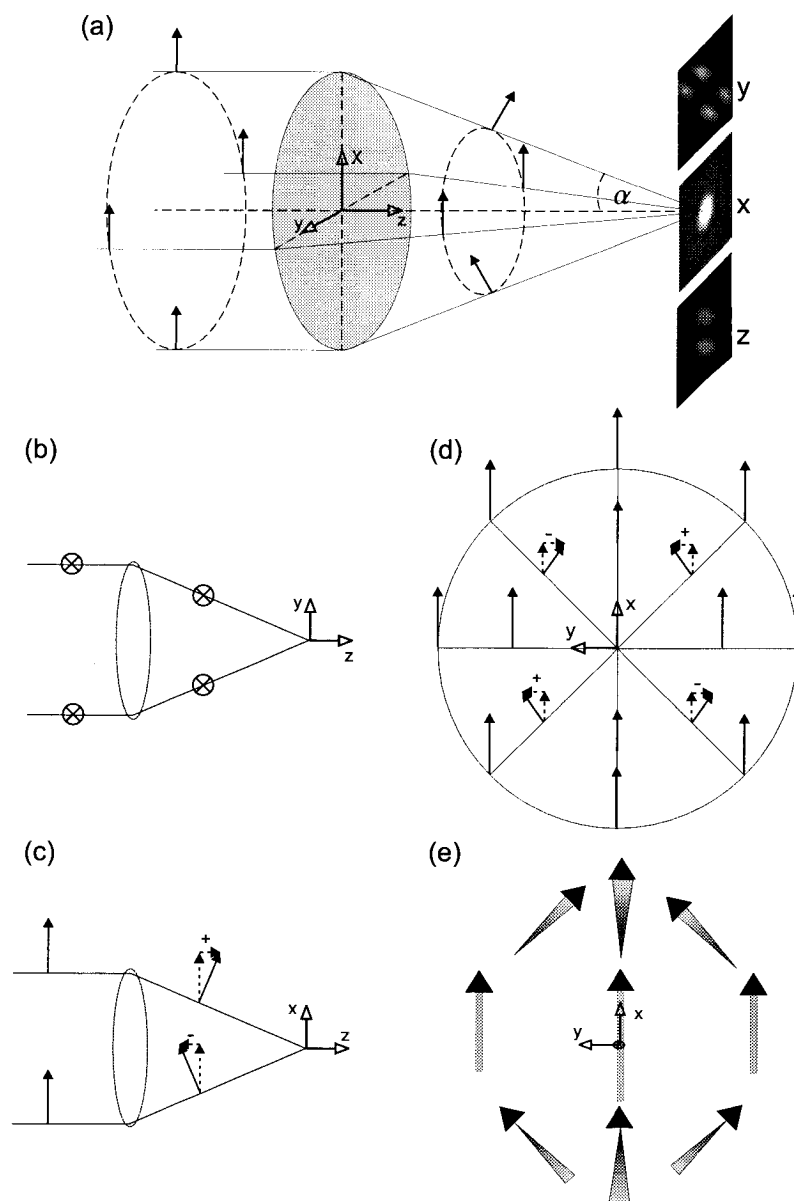
Figure 6.1: (a) Image of the three-dimensional focusing optics. The grey ellipse marks the position of the lens. For a given instant in time the electric field vectors are indicated as arrows. $(\vec{E_i})$ is the electric field before, and $(\vec{E_r})$ after refraction by the lens. (b) Section along the yz-plane (x=0). The orientation of the electric field vector points into the paper-plane ($\otimes$). (c) Section along the xz-plane (y=0). The electric field vector is within the paper plane ($\nearrow$). (d) Projection onto the xy-plane as seen from the focus. The in-plane components of the electric field are shown ($\nearrow$). (e) Summary of the field distribution in the focal plane. The arrows depict the direction of the electric field vector at indicated positions in the focal plane. The pointed shape of the arrows illustrates the z-component of the field vector (adopted from representations of chemical bonds).

field and have no y- or z-component, which causes the appearance of the dark line along the y-axis ($x = 0$) in the y-pattern as well as in the z-pattern.

Rays within the xz-plane ($y = 0$) [see figure 6.1 (c)] are p-polarized, because the electric field vector is parallel to the plane spaned by the incident and the refracted ray. Figure 6.1 (c) visualizes the fact that, after focusing, rays in the xz-plane do not contain a y-component [55] giving rise to the dark line along the x-axis ($y = 0$) in the y-pattern, which together with the dark line along the y-axis forms a dark cross in the y-pattern.

On the other hand the electric field vector of rays in the xz-plane in general undergoes a change in direction and gains in z-component due to the tilting of the rays. Figure 6.1 (c) shows that symmetric off-axis rays have electric z-components of equal values but opposite signs. Thus, superposition in the focal plane leads to a vanishing z-component on the y-axis. At positions away from the y-axis the resulting field contains a non vanishing z-component because in this case the two interfering rays have a finite pathway difference at the point of superposition. These considerations provide a qualitative explanation for the shape of the distribution of the z-component of the electric field which comprises two equally intense and symmetric lobes separated by a dark line on the y-axis.

While figure 6.1 (b) and (c) explain the existence of the dark cross in the y-pattern, figure 6.1 (d) illustrates why the focal field contains y-components at all. This is surprising because the incoming field before the lens is linearly polarized along x. The figure shows a projection of figure 6.1 (a) as seen from the focus. The eight straight lines symbolize rays at the rim of the beam which converge towards the focus. According to the discussion above, rays on the x- or y-axis have no y-component. All other off-axis beams contain a small y-component due to the superposition of refracted s- and p-polarized field components [96]. The larger the aperture angle of the ray, the larger is its electric field y-component. The relative sign of the y-components alternates from quadrant to quadrant as sketched in figure 6.1 (d). Accordingly, superposition actually leads to non-vanishing amplitudes only in the corner areas.

Figure 6.1 (e) summarizes the qualitative picture of the field distribution in the focal plane. The arrows depict the direction of the electric field vector at certain positions in the focal plane for a given instant in time. The pointed shape of the arrows illustrates the z-component of the field vector. Using this pictorial description of the field distribution provides an impression of the types of image patterns obtained for arbitrarily oriented dye molecules.

From the above considerations it is clear that rays with high semi-aperture angles α have particularly large y- and z-components of the focal electric field. Therefore, the relative magnitude of perpendicular field components with respect to the polarization can be enhanced as compared to the parallel component if the inner part of the beam is blocked (annular illumination) [100]. This property is of relevance in confocal microscopy of single molecules at interfaces especially orientational imaging of single molecules using SCOM [109, 110, 129], in tip-enhanced nonlinear optical microscopy [99], and in engineering a laser linac [100].

6.2.2 Mathematical description of the focal field

As illustrated in figure 6.1 (b) and (c) a s-polarized field remains unchanged by refraction opposed to a p-polarized field, which undergoes a change of direction. For this reason it is appropriate to decompose an incident field $\vec{E}_i$ into its s-polarized component $\vec{E}_i^{(s)}$ and its p-polarized component $\vec{E}_i^{(p)}$. Because the s-polarized component is perpendicular to the plane spanned by the unit-vectors $\hat{z}$ and $\hat{s}$ (see figure 6.2 (a)), it is given by

$$\vec{E}_i^{(s)} = \left(\vec{E}_i \cdot \frac{\hat{z} \times \hat{s}}{|\hat{z} \times \hat{s}|} \right) \cdot \frac{\hat{z} \times \hat{s}}{|\hat{z} \times \hat{s}|} \ ,$$

where the terms in the denominator are necessary for normalization. The p-polarized component lies in the plane spanned by $\hat{z}$ and $\hat{s}$ and is, as well as each component of a transverse wave, perpendicular to the direction of propagation $\hat{z}$, which leads to the expression

$$\vec{E}_i^{(p)} = \left(\vec{E}_i \cdot \frac{\hat{z} \times (\hat{z} \times \hat{s})}{|\hat{z} \times \hat{s}|} \right) \cdot \frac{\hat{z} \times (\hat{z} \times \hat{s})}{|\hat{z} \times \hat{s}|} \ .$$
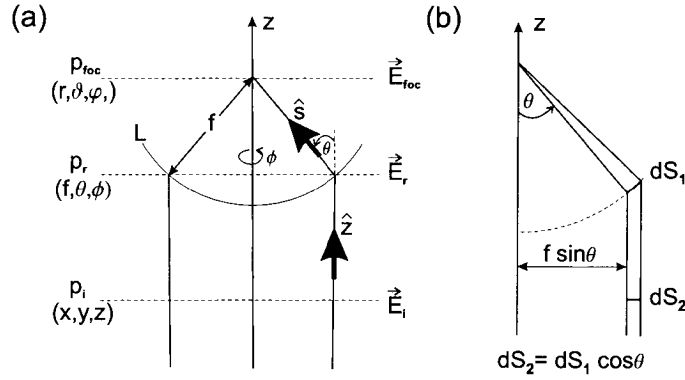
Figure 6.2: Refraction of a plane wave at an aplanatic lens (L) is determined by a spherical surface with radius f. (a) The field is considered in the planes p_i, p_r and p_{foc} with corresponding coordinate systems (x, y, z), (f, θ, ϕ) and (r, ϑ, φ), respectively. The direction of propagation is described by unit-vectors $\hat{z}$, $\hat{s}$. (b) Corresponding surfaces on the sphere and in the collimated beam are connected by a factor $\cos \theta$ which implies together with the law of energy conservation a factor $\sqrt{\cos \theta}$ between the corresponding field amplitudes.

After refraction by a lens the s-polarized component is unchanged whereas the vector $[\hat{z} \times (\hat{z} \times \hat{s})]$ describing the direction of the p-polarized component is refracted into the direction $[\hat{s} \times (\hat{z} \times \hat{s})]$, which is perpendicular to the new propagation-direction $\hat{s}$. Thus, the field direct after refraction by the lens can be expressed as

$$\vec{E}_r = \frac{\left(\vec{E}_i \cdot [\hat{z} \times \hat{s}]\right) \cdot [\hat{z} \times \hat{s}] + \left(\vec{E}_i \cdot [\hat{z} \times (\hat{z} \times \hat{s})]\right) \cdot [\hat{s} \times (\hat{z} \times \hat{s})]}{|\hat{z} \times \hat{s}|^2} \sqrt{\cos \theta} \ .$$

The factor $\sqrt{\cos \theta}$ is a consequence of energy conservation (see figure 6.2 (b)) assuming ideal refraction without losses. Restricting the calculations to the case of an incident wave $\vec{E}_i^T = (E_0, 0, 0)$, which is linear polarized in x-direction, and using spherical coordinates (f, θ, ϕ) leads, after some trigonometric manipulations, to [83]

$$\vec{E}_r(\theta, \phi) = E_0 \left[\sin \phi \begin{pmatrix} \sin \phi \\ -\cos \phi \\ 0 \end{pmatrix} + \cos \phi \begin{pmatrix} \cos \phi \cos \theta \\ \sin \phi \cos \theta \\ -\sin \theta \end{pmatrix} \right] \sqrt{\cos \theta} \ . \qquad (6.1)$$

Recalling the discussion in section 2.2.4, p. 25, the field in the focal region is completely determined by the field after the lens, because no evanescent waves

are involved. The focal field $\vec{E}_{\text{foc}}$ can be calculated according to equation 2.18, p. 25. Expressing equation 2.18 in spherical coordinates (r, ϑ, φ) instead of Cartesian coordinates (x, y, z), and introducing the field $\vec{E}_r$ as E_∞ leads to [83, 96]:

$$\vec{E}_{\text{foc}}(r, \vartheta, \varphi) = \frac{ikfe^{-ikf}}{2\pi} \int\limits_0^{\theta_{max}} \int\limits_0^{2\pi} \vec{E}_r(\theta, \phi)\, e^{ikr\cos\theta\cos\vartheta}\, e^{ikr\sin\theta\sin\vartheta\cos(\phi-\varphi)} \sin\theta\, d\phi\, d\theta \ .$$

With the mathematical relations

$$\int\limits_0^{2\pi} \cos n\phi\ e^{ix\cos(\phi-\varphi)}\, d\phi\ = 2\pi\,(i^n)\, J_n(x)\,\cos n\varphi$$

$$\int\limits_0^{2\pi} \sin n\phi\ e^{ix\cos(\phi-\varphi)}\, d\phi\ = 2\pi\,(i^n)\, J_n(x)\,\sin n\varphi$$

where J_n is the n-th order Bessel function, the integration over ϕ in equation 6.5 can be carried out analytically. The final expressions for the focal field now contain a single integration over the variable θ. It is convenient to use the following abbreviations for the occurring integrals:

$$I_0 \ = \ \int\limits_0^{\theta_{max}} \sqrt{\cos\theta}\ \sin\theta\,(1 + \cos\theta)\, J_0(kr\sin\vartheta\sin\theta)\, e^{ikr\cos\theta\cos\vartheta}\, d\theta \ , \qquad (6.2)$$

$$I_1 \ = \ \int\limits_0^{\theta_{max}} \sqrt{\cos\theta}\ \sin^2\theta\, J_1(kr\sin\vartheta\sin\theta)\, e^{ikr\cos\theta\cos\vartheta}\, d\theta \ , \qquad (6.3)$$

$$I_2 \ = \ \int\limits_0^{\theta_{max}} \sqrt{\cos\theta}\ \sin\theta\,(1 - \cos\theta)\, J_2(kr\sin\vartheta\sin\theta)\, e^{ikr\cos\theta\cos\vartheta}\, d\theta \ . \qquad (6.4)$$

Using these abbreviations the focal field can now be expressed as [83, 96]:

$$\vec{E}_{\text{foc}}(r, \vartheta, \varphi) = \frac{ikfe^{-ikf}}{2} \begin{pmatrix} I_0 + I_2\,\cos 2\varphi \\ I_2\,\sin 2\varphi \\ -2iI_1\,\cos\varphi \end{pmatrix} \ . \qquad (6.5)$$

The integration over θ in equations 6.2–6.4 is limited to the range $[0...\theta_{max}]$ because a lens has a maximum collection angle of θ_{max} determined by its numerical aperture $(NA = n\sin\theta_{max})$. Equation 6.5 represents an integral solution of the focal field in a homogeneous medium.
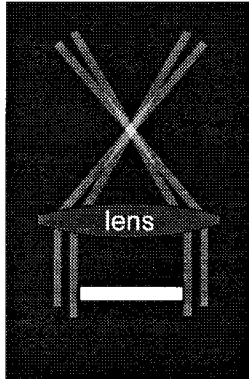
To create a focal field with comparable high z- and y-components, the inner part of the incident part is blocked (annular illumination). In this case only components within a range $[\theta_{min}...\theta_{max}]$ contribute to the focal field, which determines the integration range over θ in the integrals in equations 6.2–6.4.
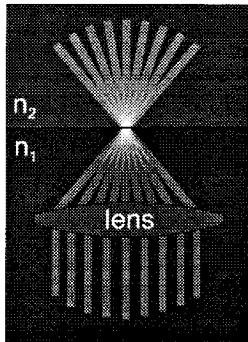
The focal field distribution is also changed if a disturber is positioned within the focal region. This is for example the case if focusing onto a planar interface between two dielectrics with refraction indices n_1 and n_2, which is realized in confocal microscopy at surfaces. The focal field distribution differs in this case from the one defined in equation 6.5, because reflection and transmission at the interface have to be taken into account. Reflection and transmission of plane waves at planar interfaces are described by Fresnel reflection and transmission coefficients (r, t), which depend on n_1 and n_2 and are different for s- and p-polarized plane waves [55]. Therefore, the focal field near an interface at $z = 0$ can be represented as

$$\vec{E}_{\text{foc/int}} = \begin{cases} \vec{E}_{\text{foc}} + \vec{E}_{\text{refl}}^{(s)}\left(r^{(s)}, \vec{E}_{\text{foc}}^{(s)}\right) + \vec{E}_{\text{refl}}^{(p)}\left(r^{(p)}, \vec{E}_{\text{foc}}^{(p)}\right) &: z < 0 \\ \vec{E}_{\text{foc}} + \vec{E}_{\text{trans}}^{(s)}\left(t^{(s)}, \vec{E}_{\text{foc}}^{(s)}\right) + \vec{E}_{\text{trans}}^{(p)}\left(t^{(p)}, \vec{E}_{\text{foc}}^{(p)}\right) &: z > 0 \end{cases}$$

$$(6.6)$$

The reflected and transmitted fields have been rigorously calculated by Lucas Novotny by using the angular spectrum formalism [83]. Together with equation 6.5

this leads again to a general integral solution of $\vec{E}_{\text{foc/int}}$, which was exploited for the following field simulations.

6.2.3 Field simulations

The electric field in the vicinity of the geometric focus has been numerically calculated for the following four geometries in order to assess the influence of different experimental parameters (see figure 6.3): (a) homogeneous medium with full illumination, (b) homogeneous medium with annular illumination, (c) focus at a dielectric interface with full illumination, and (d) focus at a dielectric interface with annular illumination.

Focal field calculations for a homogeneous medium with full and annular illumination have been performed, using the integral solution of the focal field (see equation 6.5). It contains diffraction integrals that were evaluated numerically using a series expansion [56]. The resulting focal field in a homogeneous medium is also used as a starting point to determine the focal field close to an interface (see equation 6.6). Figure 6.3 shows the squared total field ($|\vec{E}|^2$) in the xz-plane (logarithmic scale) for the geometries (a), (b), (c), and (d) as well as the respective squared x, y, and z electric field components in the focal plane. In the presence of the interface [figure 6.3 (c), (d)], rays with high aperture angles undergo total internal reflection which leads to a (weak) standing wave pattern in the higher index medium. The interface further increases the ellipticity of the spot shape. Along the direction of the initial polarization (x) the spot is almost twice as big as in the direction perpendicular to it (y). Moreover, the relative strengths of the components are changed compared with the situation where no interface is present. Annular illumination slightly reduces the spot size [128]. However, this reduction is at the expense of more pronounced side-lobes. In the case of annular illumination the focal spot splits up above the interface into two spots aligned along the direction of the incident polarization and separated by ≈ 200 nm. It is remarkable that the relative strength of the field components changes strongly for the different geometries (see table 6.1) whereas the shape of their distribution in the focal plane is nearly unaffected.
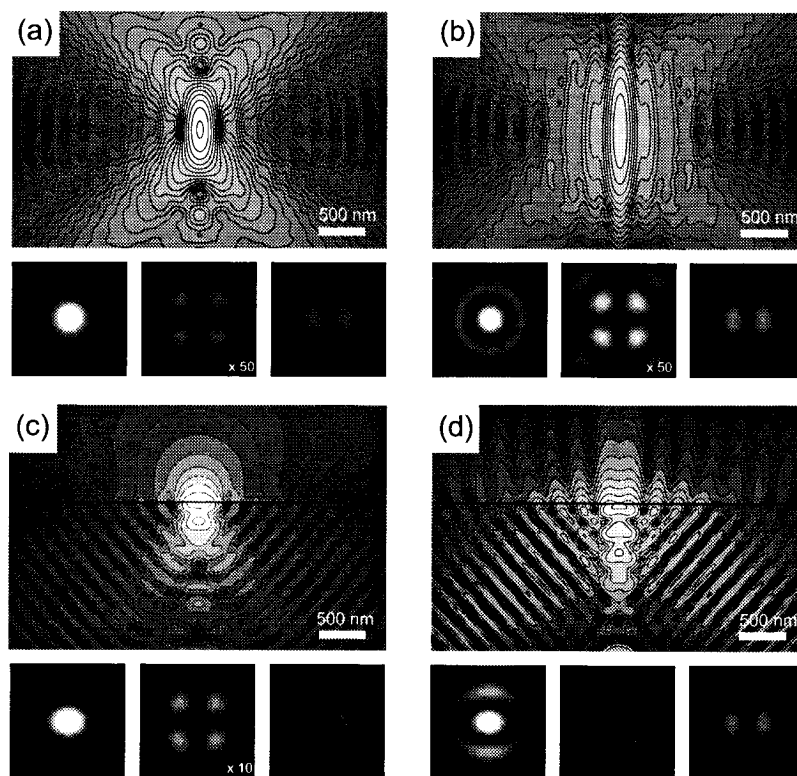
Figure 6.3: Calculated distributions of squared electric field components in the focal region for different geometries (a) homogeneous space, full illumination; (b) homogeneous space, annular illumination; (c) focus at the interface between glass (polymer) and air, full illumination; (d) focus at the interface between glass (polymer) and air, annular illumination. The large overview images show the squared total electric field in the xz-section through the geometrical focus (factor of two between adjacent lines). Each plot is accompanied by the respective plots of the squared x-, y-, and z-components of the electric field in the focal plane (1×1 μm).

Illumination	$annular$	$full$	$annular$	$full$
Interface	no	no	yes	yes
$Max[E_x^2]/Max[E_y^2]$	108	315	11	33
$Max[E_x^2]/Max[E_z^2]$	3.8 (2)	8.1 (2)	4.5 (0.93)	10.5 (0.93)

Table 6.1: Relative strength of the maximal E_x^2, E_y^2, and E_z^2 in a plane 5 nm below the polymer/air interface from calculations for different geometries. Angular range: $0°$ – $58°$ for full illumination and $38°$ – $58°$ for annular illumination. The values in brackets are the ratios of the collection efficiencies for a horizontal with respect to a vertical dipole [83].

The simulated field distribution (d), resulting for annular illumination and focusing onto a dielectric interface, is most interesting for single-molecule studies, because all components are of comparable magnitude allowing for excitation of arbitrarily oriented fluorophores. Moreover, the neighborhood of an interface is the more realistic situation in a single-molecule experiment than a bulk sample.

6.3   Methods and materials

Fluorescence

A single dye molecule is very well suited to map the distribution of field components with nanometer scale accuracy and resolution because it has an absorption cross-section in the Å- to nm-range and its fluorescence rate $R(\vec{r})$ is given by (see p. 14 in section 2.1.1)

$$R(\vec{r}) = c \left| \hat{\mathbf{d}} \cdot \vec{\mathbf{E}}(\vec{r}) \right|^2 . \tag{6.7}$$

Here, $\hat{\mathbf{d}}$ is the unit vector along the absorption dipole moment of the molecule, $\vec{\mathbf{E}}(\vec{r})$ is the electric field vector at the position $\vec{r}$ of the molecule, and c is a constant. The fluorescence rate is directly proportional to the squared field component parallel to the absorption dipole vector. The above relation is valid as long as the excitation intensity is far from saturation. Once the focal field distribution $\vec{E}$ is known it is possible to calculate scanning image patterns of single molecules according to equation 6.7 (see discussion on p.14 f.). Figure 6.4 shows the expected image patterns for molecular dipoles of varying orientations according to equation 6.7 using the numerical calculated field distribution for annular illumination and presence of an interface near the focal plane. All patterns obey the same contrast settings (scale bar on the right). The patterns change gradually as the dipole is rotated with respect to the direction of polarization. In the corners of the matrix the three pure image patterns (x, y, and z-orientation) are recovered. Patterns for other orientations, i.e. for negative angles, than ones displayed can be obtained by symmetry considerations.

Sample preparation

Samples were prepared by spin-casting (9600 rpm) of a 10 μl droplet from a solution of polymethylmetacrylate (PMMA) in toluene that also contains the dye *1,1'-dioctadecyl-3,3,3',3'- tetramethylindocarbocyanine* (DiI) in a concentration of 10^{-9} M onto standard glass cover slips. The cover slips were cleaned beforehand by baking at 510°C for six hours. The difference in the refractive indices of PMMA

($n_p = 1.49$) and glass ($n_g = 1.52$) is negligible. The only relevant step in the dielectric constant occurs at the PMMA/air boundary. Atomic force microscopy of the polymer films revealed a smooth surface and a thickness of about 30 nm.

Experimental

Figure 6.5 shows the setup used in the present study. The only difference to the confocal part of the instrument described in section 3.3 (see figure 3.5, p. 39) is a circular on-axis beam-stop (S) with a diameter of 3 mm built into the illumination path. The beam stop blocks the central part from the beam before it is reflected at the dichroic mirror and entering the microscope objective. The resulting doughnut-shaped beam is focused to a diffraction-limited spot onto the thin sample on top of a cover glass. Opening angles θ between 38° and 58° contribute to the field distribution in the focus. The full angular range of fluorescence is collected by the same objective and projected onto the active area of a single photon counting avalanche photo diode (SPAD). Single-molecule fluorescence images were recorded at excitation intensities far from saturation by raster scanning the sample through the focus using a linearized x-y-z piezo scan table and recording the number of counts for each pixel. The detected intensity is independent on the position of the imaged molecule within the focal region, because the size of the back-projected image of the active detector-area into the focal plane is about 1 μm^2 in diameter (see discussion in section 3.3). For this reason the resulting image patterns are maps of the squared field components parallel to the molecular dipoles of the imaged molecules.
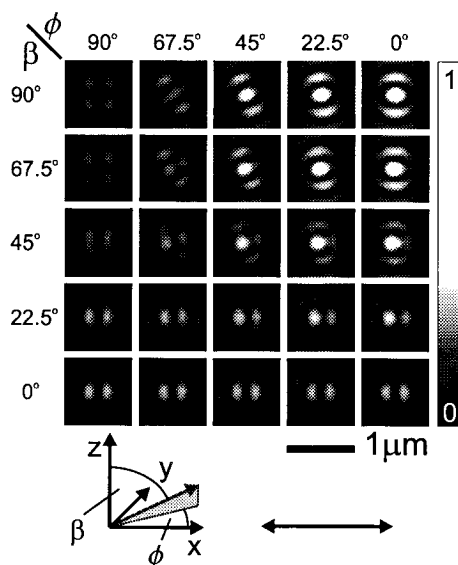
Figure 6.4: Single-molecule image patterns calculated according to equation 6.7 from the field distribution, which results by assuming annular illumination and focusing onto an interface. The image patterns were calculated for an array of differently oriented molecules placed 5 nm below the interface. The xyz coordinate system indicates the definition of the dipole orientation angles β and ϕ with respect to the incident polarization (double arrow).
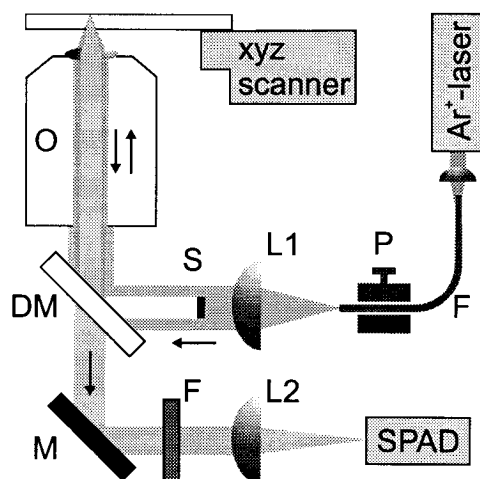

Figure 6.5: Setup for annular illumination scanning confocal optical microscopy. L1: collimation , O: microscope objective , DM: dichroic mirror, M: mirror, F: holographic notch filter, L2: focusing lens, SPAD: single photon counting avalanche photodiode, S: beam stopper, P: polarization controller, F single mode fiber.

6.4 Results and discussion

6.4.1 Field-mapping on a nano meter scale

A focal field distribution with comparable magnitude of all components is engineered according to the considerations in section 6.2.1 – 6.2.3 by using annular illumination and focusing onto a dielectric interface (see section 6.3). This configuration [case (d), see p. 93] is chosen for a detailed comparison of experimental results and theory, because it predicts comparable magnitudes for all components which is of great importance in view of single-molecule applications. Moreover, a verification of the modeled field distribution for the case (d) of focusing with annular illumination by a high numerical aperture objective onto a dielectric interface implies the validity of the more simple, underlying configurations [case (a)–(c), see p. 93].

Figure 6.6 shows fluorescence images of single molecules, which are embedded in a thin polymer film, obtained with the setup shown in figure 6.5, p. 98. The orientation of the electric field vector of the incident light before focusing is indicated by the arrows in the images. Various spot shapes can be observed. The patterns are generated by the fluorescence emission of single molecules because (i) some of the patterns are truncated because of digital photo-bleaching during line-by-line image acquisition (the images in the top row were recorded from left to right, the images in the bottom row from bottom to top), (ii) some patterns exhibit intermittent dark spots due to excursions to a dark state e.g. the triplet state and (iii) the patterns are in agreement with expected fluorescence images of a single point-like dipole. Especially patterns marked with x, y, and z, respectively, correspond to molecules with x-, y-, z-orientation (see figure 6.3, p. 94). The two images in the top row of figure 6.6, and in the bottom row, each show the same area with the excitation polarization turned by 90°. The patterns therefore appear at the same positions in the images of the left and right column and can be assigned to the same dye molecule being fixed in the PMMA matrix. The different appearance of the same molecule can be explained by the changed field distribution in the focal region due to the rotated polarization of the incidence light. This is nicely illustrated by the two molecules which are marked with y in the image figure 6.6 (a) and with x in the
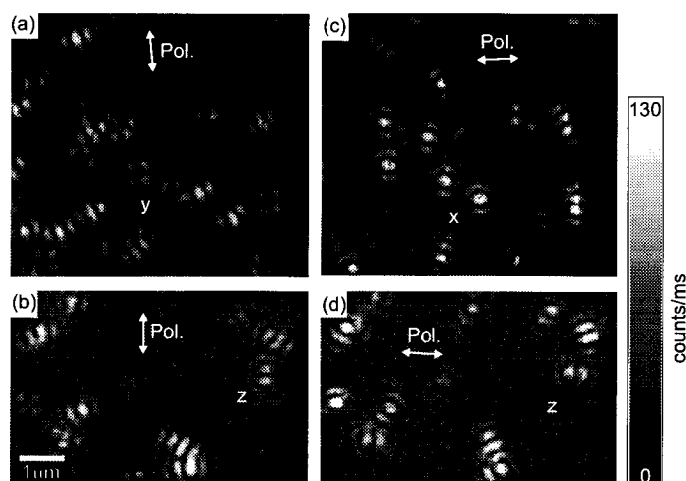
Figure 6.6: Confocal single molecule fluorescence image of DiI in a thin film of PMMA obtained with linearly polarized (arrow), annular illumination. Characteristic patterns are labeled by x, y, and z. They result from molecules that map the squared x-, y-, and z-components of the electric field in the focus, respectively.

image figure 6.6 (c) . Both show in figure 6.6 (a) a pattern which is consistent with a molecule mapping the squared y-component of the electric field distribution in the focus. This provides evidence that the molecular absorption dipole lies in the focal plane and perpendicular to the direction of polarization. In image figure 6.6 (c) the polarization is rotated by 90° and is thus parallel to the orientation of the absolute dipole of these two molecules. Accordingly, they now map the x-component of the focal field distribution. The pattern marked by z remains unchanged in figure 6.6 (b) and (d), however, its orientation follows the direction of the incident polarization, which allows for the assignment to a z-oriented molecule.

According to this consideration differently oriented molecules map the corresponding squared field components. Conversely, if the experimentally achieved field-distribution is reliably known, then it is possible to determine the orientation of the imaged molecules by comparing the recorded fluorescence patterns with the calculated maps of squared field components for different orientations as displayed in figure 6.4 (see also section 6.4.2).

Comparison of theory and measurements

In order to compare the simulated and the experimentally determined focal field, measured and calculated distributions of three, mutually perpendicular, squared field components are compared in the following. For this purpose it is most illustrative to compare the measured x-, y- , and z-patterns with the corresponding simulations. Figure 6.7 shows the comparison between measurement and simulation. The images in row A are measured image patterns, row B shows the respective calculated maps of the squared x- y- and z-field components in the focal plane (column x, y, and z). The measured as well as the calculated images have a size of $1 \times 1 \mu m$ with the origin in the center of the patterns. Either two (in the case of the x- and z-pattern) or three characteristic line cuts (in the case of the y-pattern) were taken at the same positions in the measured and calculated images. The cuts taken from the measured images and calculated patterns are indicated by solid and dashed lines, respectively. The resulting intensity profiles have been normalized. The top and the bottom row shows the horizontal sections and the vertical and diagonal sections, respectively.

Experiments and theory are compared without adjustable parameters apart from normalization!

A first glance at the profiles in figure 6.7 reveals a good agreement between measurements and calculations, regarding the general curve shape as well as the size, position, and relative intensities of main and side peaks. The vertical sections in the observed and calculated x-pattern match nearly perfectly. The horizontal sections in the x-patterns show that the measured width of the peaks is slightly broader (14%) than the calculated width. The intensity of the side peaks is 24% larger in the calculated pattern than in the measured pattern. The positions of the side peaks match perfectly. In case of the y-pattern, all profiles show a very good agreement with respect to relative intensities of main and side peaks. In the upper right corner the side lobe of another molecule overlaps with the side lobe of the investigated pattern which causes larger intensities in this area (by a factor of 2). The horizontal section in the z-patterns reveals a wider peak-width (14%) in the measurement than in the calculation and the measured side-lobes are

more pronounced. This is similar to the case of the x-pattern (x,A). The intensity profiles of the vertical section match very well even though the molecule shows blinking during the image acquisition. Other conspicuous features in the measured pattern are some black or rather dark pixels within the patterns. They result from excursions to a dark state of fluorescence (e.g. a triplet state). Black pixels turn up if the off-time exceeds the integration time of 1 ms per pixel and pixels with reduced intensity appear for shorter dark state lifetimes. Additionally, intermediate intensities are caused by interpolation between two adjacent pixels which was the only image processing performed. Furthermore, there is a certain influence of shot noise in the measured data. The shot noise is given by the square root of the absolut count-number with $n \sim 150$ counts per ms in the peaks.
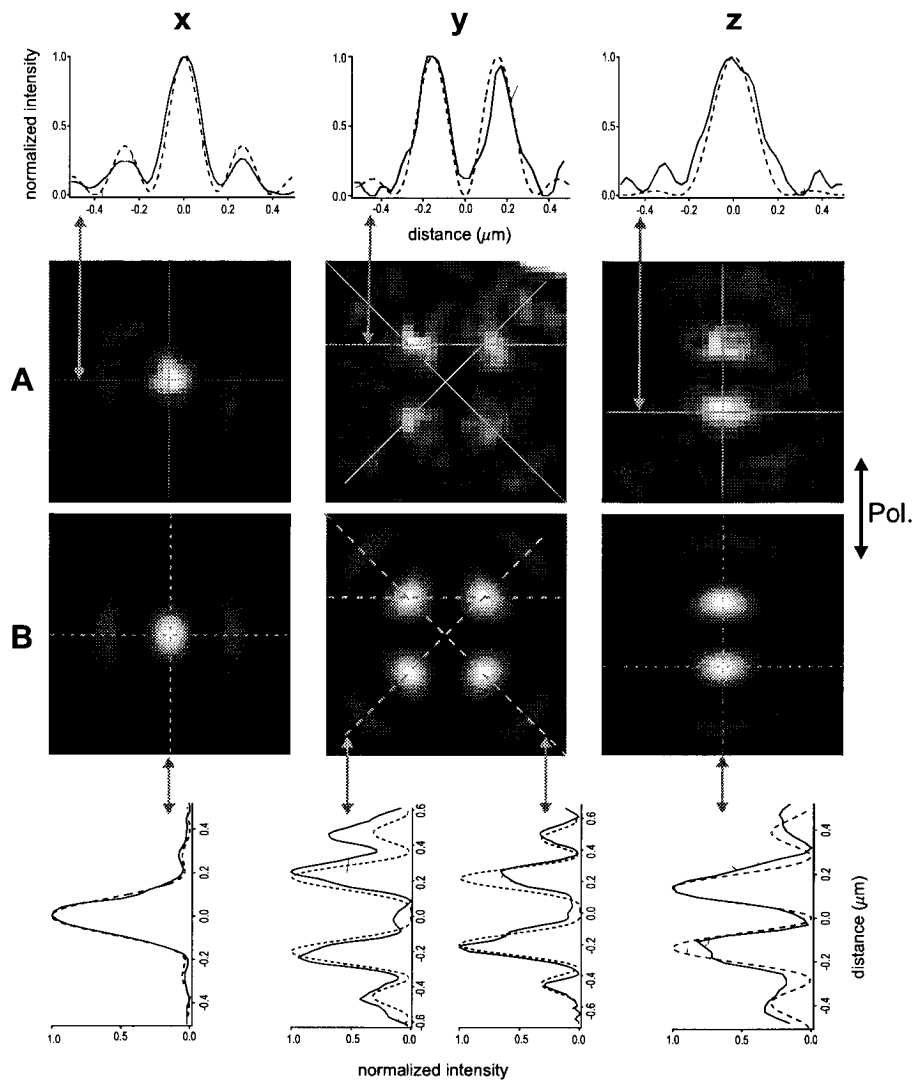
Figure 6.7: Comparison of measured and calculated field maps. In columns: field-maps in the focal plane of the squared x-, y-, z-component indicated with x, y, and z. The top row shows intensity profiles of the horizontal sections of the measurements (solid curves) and simulations (dashed curves). Row A: measured field maps, Row B: calculated field maps. Bottom row: intensity profiles of vertical and diagonal sections of the measured data (solid curves) and simulations (dashed curves).

6.4.2 Orientational imaging of single molecules

In section 6.4.1 it was shown that it is possible to engineer a focal field distribution which contains components of comparable magnitude in all directions. This allows for exciting molecules of arbitrary orientations. Moreover it was demonstrated that the experimentally achieved field distribution is reliable known by the corresponding simulations (see section 6.4.1). This opens the way for determining the three-dimensional orientation of an arbitrarily oriented molecule by comparing the recorded image pattern with simulated image patterns of differently oriented molecules. The simulated image patterns are calculated according to equation 6.7, p. 96, assuming that the molecules are placed 5 nm below the polymer/air interface. A matrix of simulated image patterns is calculated in steps of $22.5°$ covering all possible three-dimensional orientations (see figure 6.8). The upper image-matrix in Figure 6.8 shows image pattern in the case of x-polarized incident light; the image patterns at corresponding positions in the lower matrix show the appearance of the same molecule provided that the polarization of the incident light is rotated by $90°$. The dipole orientation is described by two angles, φ and β, which are defined in the coordinate system in figure 6.8. The contrast settings are the same for each pattern.

As an example, the orientation of the absorption dipoles of nine molecules which are marked in the upper two images in figure 6.9 shall be determined in the following. Both images were recorded with x-polarized incident light. For this reason the detected image patterns are compared with the calculated image patterns in the upper matrix in figure 6.8. Simulated patterns are picked out which best match with the observed patterns and are shown in the upper row of the table in figure 6.9. The orientation of the imaged molecules are determined by the angles φ and β which can be taken from the matrix 6.8 for the matching pattern. This in principle concludes the orientation determination. For a cross-check the two lower images in figure 6.9 were recorded at the same sample area in a second scan after rotating the polarization by $90°$. Two molecules have disappeared due to photo-bleaching but the nine marked molecules reemerge, as expected, at the same positions but with changed pattern. The orientations of all visible molecules are determined by the
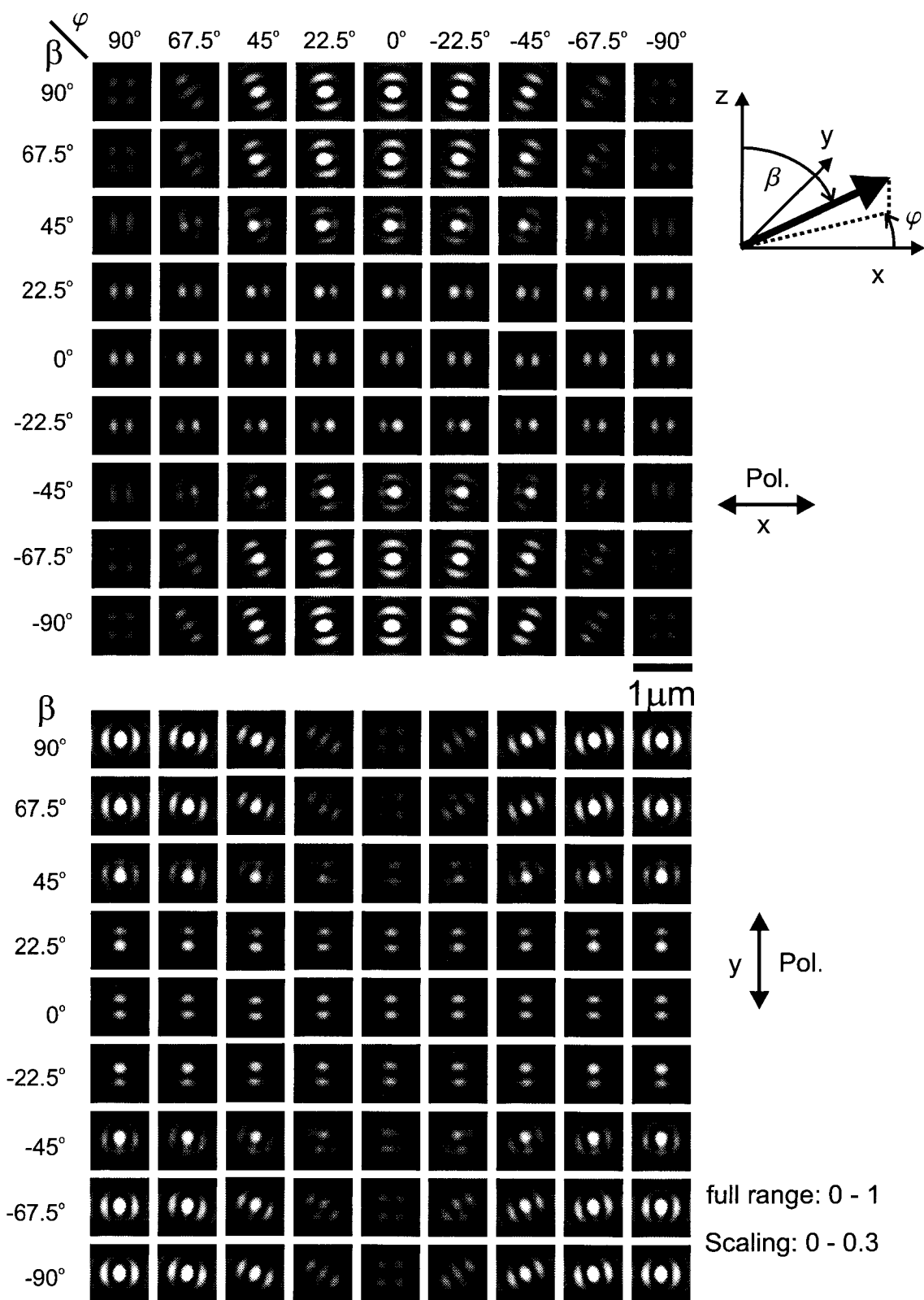
Figure 6.8: Calculated fluorescence patterns for differently oriented molecules in the case of x-polarized (upper matrix) and y-polarized (lower matrix) incident light.
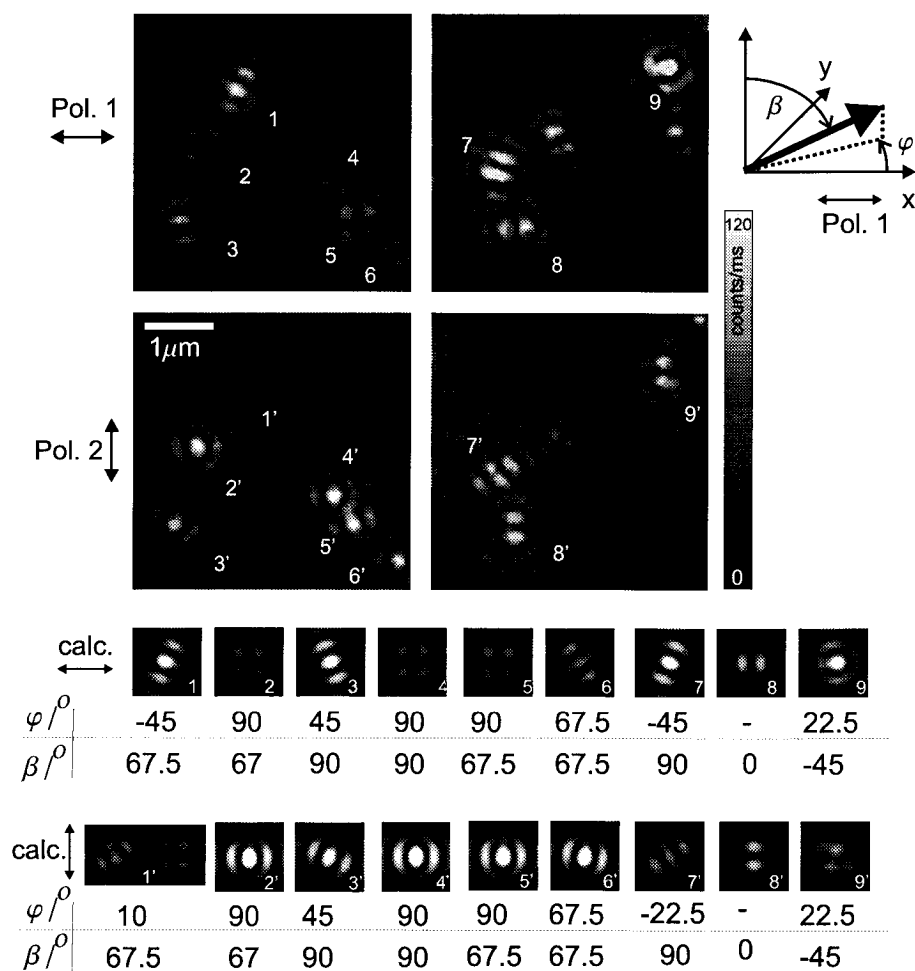
Figure 6.9: Single molecule orientation determination. Single molecules embedded in a thin PMMA film were imaged by annular illumination SCOM. The polarization of the incident light is depicted as double arrow on the left hand side. The orientations of the nine marked molecules are determined in two images series, which were recorded subsequently with x- and y-polarized incident light, respectively (see coordinate system on the right hand side). The resulting orientations are listed in the bottom tables, where the matching simulated image patterns together with the corresponding angles are shown.

same procedure using the lower matrix in figure 6.8. For the molecules number 2, 3, 4, 5, 6, 8 and 9 the determined orientation is the same in the first and the second scan. Molecule number 1 and 7 are assigned to different orientations in the first and second scan. The pattern 1' seems to lie between the two simulated patterns which are shown in the lower table in figure 6.9, which implies that the corresponding molecule has rotated in-plane by $\approx 35°$. For the molecule 7 an in-plane rotation by $\approx 22°$ is determined.

The precision in this method is yet restricted to about $10°$ because the comparison between measurement and simulation is based on the pattern-matrix in figure 6.8 with steps of $22.5°$ and was done by visual inspection. But the good agreement between simulation and data, which was revealed in the quantitative comparison in section 6.4.1, gives evidence for a great potential of this method in combination with suitable image processing for a reliable determination of the orientation of the molecular absorption dipole .

6.5 Conclusions

The striking agreement between measured and calculated field maps (see section 6.4.1) allows for the conclusion that the model of the focusing process with high numerical aperture lenses is experimentally verified. Moreover it is demonstrated that single molecules can be utilized to quantitatively map the spatial distribution of confined optical fields with great accuracy. The remaining deviations between simulation and data in the present study are partly caused by blinking and shot noise. Both sources of errors can be decreased by increasing the integration time. However, an increased integration time decreases the time resolution and increases the risk of photo-bleaching during image acquisition. For long integration times orientational diffusion can blur the observed patterns. Apart from these sources of errors inherent to the method there are actually small differences between the model and the actual experimental configuration. For example, the incident light may be not perfectly linearly polarized (typical depolarization between 10^{-2} and 10^{-3}). Also

the model assumption of an incident plane wave is not perfectly fulfilled by a laser-beam with Gaussian profile even if the entrance aperture is over-illuminated.

The calculated field-maps can be regarded as point spread functions for differently oriented dipole-point-sources, which characterize the capability of the confocal microscope (see section 2.2.5, p. 26). The consistence of calculated and measured field-maps therefore proves that the theoretically predicted resolution limit is achieved by the implemented instrument.

Relying on the convincing agreement between simulated and measured image patterns a method for determination of molecular dipole orientations was presented. It should be pointed out, that within the presented method the arbitrary orientation of a molecular dipole can be determined from a single image. However, by imaging the same molecules twice with orthogonal polarization, the method can be extended to determine the full orientation of single molecules far from an interface. Thus, the optical sectioning capabilities of confocal microscopy as well as any other facility of SCOM can simultaneously be exploited. The demonstrated method is well suited for monitoring rotational diffusion of single molecules in complex environments. In the case of DiI molecules embedded in a thin PMMA film the determined orientation of nine molecules imaged in two subsequent scans imply a quite fixed orientation of the molecules within the polymer matrix. The speed of the method is only limited by the photon emission rate. Assuming that 10×10 pixels are sufficient to determine the pattern of a single molecule, the time needed to determine the absorption dipole orientation is 100 ms.

Bibliography

[1] W.P. Ambrose, and W. E. Moerner, Nature **349**, 225 (1991)

[2] W.P. Ambrose, P.M. Goodwin, J.C. Martin, and R.A. Keller, Science **265**, 364 (1994)

[3] W.P. Ambrose, P.M. Goodwin, J.C. Martin, and R.A. Keller, Phys. Rev. Lett. **72** 160 (1994)

[4] W.P. Ambrose, P.M. Goodwin, J. Enderlein, D.J. Semin, J.C. Martin, and R.A. Keller, Chem. Phys. Lett. **269**, 365 (1997)

[5] K. Bahlmann, and S.W. Hell, Appl. Phys. Lett. **77**, 612 (2000)

[6] T. Basché, W.E. Moerner, M. Orrit, and U.P. Wild, eds., *Single–Molecule Optical Detection, Imaging and Spectroscopy*, VCH Weinheim, (1997)

[7] T. Basché, W.E. Moerner, M. Orrit, and H. Talon, Phys. Rev. Lett. **69**, 1516 (1992)

[8] T. Basché, Talk at the *Minisymposium on Nanophysical Chemistry*, ETH Zurich (2000)

[9] Baudour, Delugeard, Cailleau, Acta Cryst. B32 150 (1976)

[10] F. Kulzer, F. Koberling, Th. Christ, A. Mews, and T. Basché, Chem. Phys. **247**, 23 (1999)

[11] W. Becker, H. Hickl, C. Zander, K.H. Drexhage, M. Sauer, S. Siebert, J. Wolfrum, Rev. Sci. Instr. **70**, 1835 (1999)

[12] A. Bernard, E. Delamarche, H. Schmid, B. Michel H.R. Bosshard, and H. Biebuyck, Langmuir **14**, 2225 (1998)

[13] H. Bethe, Phys. Rev. **66**, 163 (1944)

109

[14] E. Betzig, J. K. Trautman, T. D. Harris, J. S. Weiner, and R. L. Kostelak, Science **251**, 1468 (1991)

[15] E. Betzig, P. L. Finn, and J. S. Weiner, Appl. Phys. Lett. **60**, 2484 (1992).

[16] E. Betzig and R.J. Chichester, Science **262**, 1422 (1993)

[17] D.A. Vanden Bout, W. Yip, D. Hu, D. Fu, T.M. Swager, and P.F. Barbara, Science **277**, 1074 (1997).

[18] M.A. Bopp, G. Tarrach, M.A. Lieb, and A.J. Meixner, J. Vac. Sci. Technol. A **15**, 1423 (1997)

[19] M.A. Bopp, Y. Jia, L. Li, R.J. Cogdell, and R.M. Hochstrasser, Proc. Natl. Acad. Sci. USA, **94**, 10630 (1997)

[20] C.J. Bouwkamp, Philips Res. Rep **5**, 321 (1950)

[21] E. Brooks Shera, N.K. Seitzinger, L.M. Davis, R.A. Keller ,and S.A. Soper, Chemical Physics Letters **174**, 553 (1990)

[22] L. Brand, C. Eggeling, C. Zander, K.H. Drexhage, and C. Seidel, J. Phys. Chem. A **101,** (1997)

[23] R.R. Chance, A. Prock, and R. Silbey, J. of Chem. Phys. **60**, 2744 (1974)

[24] J. Dejace, Bull. Soc. Fr. Minér. Crist. **92**, 141 (1969)

[25] E. Delamarche, A. Bernard, H. Schmid, B. Michel, and H. Biebuyick, Science **276**, 779 (1997)

[26] R.M. Dickson, D.J. Norris, Y. Tzeng, and W.E. Moerner, Science **274**, 966 (1996)

[27] R.M. Dickson, D.J. Norris, and W.E. Moerner, Phys. Rev. Lett. **81**, 5322 (1998), A.P. Bartko and R.M. Dickson, J. Phys. Chem. B **103** 3053 (1999), J. Phys. Chem. B **103** 11237 (1999)

[28] K. Dorre, et al. Bioimaging **5,** 139 (1997)

[29] M. Eigen, and R. Rigler, Proc. Natl. Acad. Sci., **91**, 5740 (1994)

[30] S.A. Empedocles, R. Neuhauser, and M.G. Bawendi, Nature **399**, 126 (1999)

[31] L. Fleury, B. Sick, G. Zumofen, B. Hecht, and U.P. Wild, Mol. Phys. **95**, 1333 (1998)

[32] L. Fleury, J. M. Segura, G. Zumofen, B. Hecht, and U. P. Wild, Phys. Rev. Lett. **84**, 1148 (2000).

[33] C.S. Foote, J.S. Valentine, A. Greenberg, J.F. Liebman, *Active Oxygen in Chemistry*, Eds ; Blackie Academic & Professionnal ; London (1995)

[34] T. Funatsu, Y. Harada, M. Tokunaga, K. Saito ,and T. Yanagida, Nature **374**, 555 (1995)

[35] J.R. Fries, L. Brand, C. Eggeling, M. Kollner, and C. Seidel, J. Phys. Chem. A **102**, 6601 1998

[36] Frontiers in Chemistry *Single Molecules*, Science **283** (1999)

[37] A. Garner, F. Wilkinson, Chem. Phys. Lett. **45**, 432 (1977)

[38] J.K. Gimzewski, and C. Joachim, Science **283**, 1683 (1999)

[39] J.W. Goodman, *Introduction to Fourier optics*, Mcgraw-Hill (1968)

[40] F. Güttler, M. Croci, A. Renn,and U.P. Wild, Chem. Phys. **211**, 421 (1996).

[41] T. Ha, T. Enderle, D.F. Ogletree, D.S. Chemla, P.R. Selvin ,and S. Weiss, Proceedings of the National Academy of Sciences of the United States of America **93**, 6264 (1996)

[42] T. Ha, Th. Enderle, and D.S. Chemla, Phys. Rev. Lett. **77**, 3979 (1996)

[43] T. Ha, T. Enderle, D.F. Ogletree, D.S. Chemla, P.R. Selvin, and S. Weiss, Proc. Natl. Acad. Sci. USA **93**, 6264 (1996)

[44] T. Ha, J. Glass, Th. Enderle, D. S. Chemla, and S. Weiss, Phys. Rev. Lett. **80**, 2093 (1998)

[45] T. Ha, T.A. Laurence, D.S. Chemla, and S. Weiss, J. Phys. Chem. B **103**, 6839 (1999)

[46] Ch. Hafner, *The Generalized Multiple Multipole Technique for Computational Electrodynamics*, Artech, Boston, Mass., (1990)

[47] E. Hecht, *Optics*, Addison-Wesley Publishing Company (1987)

[48] B. Hecht, PhD thesis (ISBN 3-89649-072-9), University of Basel (1996)

[49] B. Hecht, H. Bielefeldt, Y. Inouye, L. Novotny, and D.W. Pohl, J. Appl. Phys. **81**, 2492 (1997)

[50] B. Hecht, B. Sick, U.P. Wild, V. Deckert, R. Zenobi, O.J.F. Martin; and D. Pohl, J. Chem. Phys. **112**, 7761 (2000)

[51] C.W. Hollars, and R.C. Dunn , J. Chem. Phys. **112**, 7822 (2000)

[52] P. Hoffmann, B. Dutoit, and R.-P. Salathé, Ultramicroscopy **61**, 165 (1995)

[53] Y. Ishii, T. Yoshida, T. Funatsu, T. Wazawa, T. Yanagida, Chem. Phys. **247**, 163 (1999)

[54] M. Ishikawa, K. Hirano, T. Hayakawa, S. Hosoi ,and S. Brenner, Japanese Journal of Applied Physics, Part 1 (Regular Papers & Short Notes) **33**, 1571 (1994)

[55] J.D. Jackson *Klassische Elektrodynamik*, second edition, Walter de Gruyter Verlag (1983)

[56] R. Kant, J. Mod. Opt. **40**, 337 (1993)

[57] K. Kitamura, M. Tokunaga, A.H. Iwane, T. Yanangida, Nature **397**, 129 (1999)

[58] M. Kollner, A. Fischer, J. ArdenJacob, K.H. Drexhage, R. Muller, S. Seeger, J. Wolfrum, Chem. Phys. Lett. **250**, 355 (1996)

[59] H. Kuhn, J. of Opt. Phys. **53**, 101 (1969)

[60] S. Kummer, Th. Basché, and C. Bräuchle, Chem. Phys. Lett. **229**, 309 (1994)

[61] S. Kummer, F. Kulzer, R. Kettner, Th. Basché, C. Tietz, C. Glowatz, and C. Kryschi, J. Chem. Phys. **107**, 7673 (1997)

[62] D.V. Labeke, D. Barchiesi, and F. Baida, J. Opt. Soc. Am. A **12**, 695 (1995)

[63] J.R. Lakowicz *Fluorescence Spectroscopy*, second edition, Kluwer Academic/Plenum Publisher, New York (1999)

[64] P. Lambelet, A. Sayah, M. Pfeffer, C. Philipona, and F. Marquis-Weible, Appl. Opt. **37**, 7289 (1998)

[65] A. Harootunian, E. Betzig, M. Isaacson, and A. Lewis, Appl. Phys. Lett. **49**, 674 (1986)

[66] H.P. Lu and X.S. Xie, Nature **385**, 143 (1997)

[67] H.P. Lu, XS. Xie, J. Phys. Chem. B **101**, 2753 (1997)

[68] H.P. Lu, L. Xun, and X.S. Xie, Science **282**, 1877 (1998)

[69] W. Lukosz, J. Opt. Soc. Am. **69**, 1495 (1979)

[70] W. Lukosz, Phys. Rev. B **22**, 3030 (1980)

[71] J.J. Macklin, J.K. Trautman, T.D. Harris, and L.E. Brus, Science **272**, 255 (1996).

[72] L. Mandel & E. Wolf, *Optical coherence and quantum optics*, New York: Cambridge University Press (1995)

[73] O.J.F. Martin & C. Girard), Appl. Phys. Lett. **70**, 705 (1997

[74] J. Michaelis, C. Hettich, J. Mlynek, and V. Sandoghdar, Nature **405**, 325 (2000)

[75] W.E. Moerner ,and L. Kador, Physical Review Letters **62**, 2535 (1989)

[76] S. Münster, S. Werner, C. Mihalcea, W. Scholz, and E. Oesterschulze, J. Microsc. **186**, 17 (1997)

[77] D. Naumann, *Fluor und Fluorverbindungen* Steinkopff, Darmstadt (1980)

[78] S. Nie, D.T. Chiu, and R.N. Zare, Science **266** 1018 (1994)

[79] S. Nie, and R.N. Zare, Anal. Chem. **70,** 431 (1995)

[80] S. Nie ,and R.N. Zare, Annual Review of Biophysics and Biomolecular Structure **26**, 567 (1997)

[81] W. Noell, M. Abraham, K. Mayr, A. Ruf, J. Barenz, O. Hollricher, O. Marti, and P. Günther, Appl. Phys. Lett. **70**, 1236 (1997)

[82] L. Novotny, D. Pohl, and B. Hecht, Opt. Lett. **20**, 970 (1995)

[83] L. Novotny, R.D. Grober, K. Karrai, submitted to Opt. Lett. (2000)

[84] T. Yatsuia, M. Kourogi, and M. Ohtsu, Appl. Phys. Lett. **73**, 2090 (1998)

[85] M. Orrit ,and J. Bernard, Physical Review Letters **65**, 2716 (1990)

[86] T. Pagnot, D. Barchiesi, D. Van Labeke, and C. Pieralli, Opt. Lett. **22**, 120 (1997)

[87] T. Pagnot, D. Barchiesi, and G. Tribilon, Appl. Phys. Lett. **75**, 4207, (1999)

[88] O. Panzer, W. Göhde, U.C. Fischer, H. Fuchs, K. Müllen, submitted to Advanced Materials (1998)

[89] T.Plakhotnik, W.E. Moerner, V. Palm, U.P. Wild, Opt. Commun. **114**, 83 (1995)

[90] T. Plakhotnik, E. Donley, and U.P. Wild, Annu. Rev. Phys. Chem. **48**, 181 (1997)

[91] D.W. Pohl, W. Denk, and M. Lanz, Appl. Phys. Lett. **44**, 651 (1984)

[92] D. W. Pohl, Advances in Optical and Electron Microscopy **12**, 243 (1991).

[93] S. Qabis, R. Dorn, M. Eberler, O. Glöckl, and G. Leuchs, Opt. Commun. **179**, 1 (2000)

[94] M. Prummer, C. Hübner, B. Sick, B. Hecht, A. Renn, and U.P. Wild, Anal. Chem. A **72**, 443 (2000)

[95] S. Rice, and G. Kenney-Wallace, Chem. Phys. **47, 161** (1980)

[96] B. Richards, E. Wolf, Proc. R. Soc. London A **253**, 358 (1959)

[97] M. Sauer, J. ArdenJacob, K.H. Drexhage, F. Gobel, U. Lieberwirth, K. Muhlegger, R. Muller, J. Wolfrum, and C. Zander, Bioimaging **6**, 14 (1998)

[98] I. Sase, H. Miyata, S. Ishiwata, and K. Kinosita, Proc. Natl. Acad. Sci. USA **94**, 5646 (1997)

[99] E.J. Sanchez, L. Novotny, X.S. Xie, Phys. Rev. Lett. **82**, 4014 (1999)

[100] M.O. Scully, Appl. Phys. B **51**, 238(1990)

[101] J.M. Segura, Ph.D. thesis, ETH Zurich (2000)

[102] J. Sepiol, J. Jasny, J. Keller, and U.P. Wild, Chem. Phys. Lett. **273**, 444 (1997).

[103] Th. Schmidt, G.J. Schütz, W. Baumgartner, H.J. Gruber, and H. Schindler, Proc. Natl. Acad. Sci. USA **93**, 2926 (1996)

[104] M.J. Schnitzer, and S.M. Block, Nature **388**, 386 (1997)

[105] G.J. Schütz, W. Trabesinger, and T. Schmidt, Biophys. J. **74**, 2223 (1998)

[106] G.J. Schütz, G. Kada, V.P. Pastushenko, and H. Schindler, EMBO J. **19**, 892 (2000)

[107] E.B. Shera, N.K. Seitzinger, L.M. Davis, R.A. Keller, and S.A. Soper, Chem. Phys. Lett. **174**, 553 (1990)

[108] S.A. Soper,L.M. Davis, and E.B. Shera, J. Opt. Soc. Am. B **9**, 1761 (1992)

[109] B. Sick, B. Hecht; L. Novotny, Phys. Rev. Let. **85**, 4482 (2000)

[110] B. Sick, B. Hecht; L. Novotny, J. Microcopy, accepted

[111] R. Stöckle, N. Schaller, V. Deckert, C. Fokas, and R. Zenobi, J. Microsc., in press.

[112] R. Stöckle, V. Deckert, C. Fokas, D. Zeisel, and R. Zenobi, Vib. Spectrosc., submitted.

[113] R. Stoeckle, C. Fokas, V. Deckert, and R. Zenobi; B. Sick, B. Hecht, and U.P. Wild, Appl. Phys. Let. **75**, 160 (1999)

[114] E.H. Sygne, Phil. Mag. **6**, 356 (1928)

[115] Ph. Tamarat, B. Lounis, J. Bernard, M. Orrit, S. Kummer, R. Kettner, S. Mais, and Th. Basché, Phys. Rev. Lett. **75**, 1514 (1995)

[116] J.K. Trautman ,and J.J. Macklin, Chemical Physics **205**, 221 (1996)

[117] D. R. Turner, US Patent No 4,469,554, (1984)

[118] M. A. Unger, D. A. Kossakovski, R. Kongovi, J. L. Beauchamp, J. D. Baldeschwieler, and D. V. Palanker, Rev. Sci. Instr. **69**, 2988 (1998)

[119] G. A. Valaskovic, M. Holton, and G. H. Morrison, Appl. Opt. **34**, 1215 (1995)

[120] D.A. Vanden Bout, W.T. Yip, D. Hu, D.K. Fu, T.M. Swager and P. F. Barbara, Science **277**, 1074 (1997)

[121] A. VanOrden, N.P. Machara, P.M. Goodwin, and R.A. Keller, Anal. Chem. **70**, 1444 (1998)

[122] J. A. Veerman, A. M. Otter, L. Kuipers, and N. F. van Hulst, Appl. Phys. Lett. **72**, 3115 (1998)

[123] J.A. Veerman, M.F. Garcia-Parajo, L. Kuipers, and N.F. van Hulst, J. Microsc. **194**, 477 (1999).

[124] J.A. Veerman, PhD-thesis (ISBN 90-36513510) University Twente (1999)

[125] R.H. Webb, *Confocal optical microscopy*, Rep. Prog. 59 (1996)

[126] S. Weiss, Science **283** 1676 (1999)

[127] T. Wazawa, Y. Ishii, T. Funatsu, and T. Yanagida, Biophys. J. **78**, 1561 (2000)

[128] T. Wilson & C. Sheppard *Theory and practice of scanning optical microscopy*, Academic Press (1984)

[129] X.S. Xie ,and J.K. Trautman, Annual Review of Physical Chemistry **49**, 441 (1998)

[130] X.H. Xu, and E. S. Yeung, Science **275**, 1106 (1997)

[131] R. Yasuda, H. Noji, K.Jr Kinosita, M. Yoshida, Cell **93**, 1117, (1998)

[132] K.S. Youngworth & T.G. Brown, Optics Express **7**, 77 (2000)

[133] C. Zander, M. Sauer, K.H. Drexhage, D.S. Ko, A. Schulz, J. Wolfrum, L. Brand, C. Eggeling, C. Seidel, Appl. Phys. B **63**, 517 (1996)

[134] C. Zander, K.H. Drexhage, K.T. Han, J. Wolfrum, and M. Sauer, Chem. Phys. Lett. **286**, 457 (1998)

[135] D. Zeisel, S. Nettesheim, B. Dutoit, and R. Zenobi, Appl. Phys. Lett. **68**, 2941 (1996).

[136] X.Zhuang, L.E. Bartley, H. Babcock, R. Russell, T. Ha, D. Herschlag, S. Chu, Science **288**, 2048 (2000)

Danksagung

An erster Stelle danke ich Urs Wild für die Möglichkeit in seiner Gruppe zu arbeiten. Ohne die hervorarragenden Arbeitsbedingungen wären die durchgeführten Experimente nicht möglich gewesen.

Für die freundliche Übernahme des Koreferats möchte ich Prof. Merkt und Bert Hecht danken. Insbesondere Bert Hecht hat mit viel optischem Fachwissen und guten Ideen als mein Betreuer einen großen Beitrag zu dieser Arbeit geleistet.

Große Teile dieser Arbeit resultieren aus Zusammenarbeiten mit verschiedenen Kollegen: Ludovic Fleury, Gert Zumofen, Raoul Stöckle, Christian Fokas, Volker Deckert, Michael Prummer, Christian Hübner, Alois Renn und Lukas Novotny. Ich möchte ausdrücklich auch allen anderen Kollegen für die vielen hilfreichen, tiefschürfenden und unterhaltsamen Gespräche über die Physik und den Sinn des Lebens danken.

Jean-Manuel Segura, Werner Trabesinger und Michael Prummer haben mit mir die 'Mühle' auf dem Schreibtisch und das Labor geteilt, mir unzählige Male geholfen und nebenher auch den Spaß nicht zu kurz kommen lassen. Jean-Manuel hat mir sehr geholfen als es darum ging, erste mikriskopische Schritte auf dem leergefegten optischen Tisch zu wagen. Michael danke ich besonders für die vielen, fruchtbaren Diskussionen während des Schreibens dieser Arbeit und für das Korrigieren der gröbsten sprachlichen Fehler.

Markus Traber, Udo Wallenborn und Michael Matthias danke ich für stete, prompte und konkrete Unterstützung im Cyber-Space, wenn es in meiner Computer-Welt mal krieselte.

Meinen Eltern verdanke ich vieles, insbesondere ein unbeschwertes Studium!

Manuela, Steffen, Michael, Anja, Sonja, Andreas, Reto, Agnes, Franko, Fabio und Jorge danke ich für die vielen schönen 'außer-Labor-Stunden' während meiner Doktorandinnenzeit.

Seite Leer /
Blank leaf

Curriculum Vitae

Name: Beate Sick

Geburtsdatum: 25. August 1967

Geburtsort: Stuttgart, Deutschland

Nationalität: deutsch

Feb. '97 - Jan. '01   Dissertation in der Gruppe von Prof. U.P. Wild am Institut für physikalische Chemie, ETH Zürich, Schweiz.

Dez. '94 - Dez. '96   Referendariat für das Lehramt an Gymansien im Schulpraktischen Seminar Spandau, Berlin, Deutschland. Abschluß mit dem 2. Staatsexamen in Mathematik und Physik.

Okt. '87 - Jun. '94   Studium an der Ruprecht-Karls-Universität Heidelberg, Deutschland, mit den Fächern Physik, Mathematik und Erziehungswissenschaften. Abschluß mit dem Diplom in Physik, dem 1. Staatsexamen in Mathematik und Physik und dem Pädagogikum.

Aug. '74 - Mai '87   Schulausbildung in Stuttgart, Deutschland. Abschluß mit der allgemeinen Hochschulreife.